# PH.D. THESIS

Real-time in-situ chemical sensing, sensor-based film thickness metrology, and process control in W CVD process

*by Yiheng Xu*
*Advisor: Gary W. Rubloff*

**PhD 2001-2**


*ISR develops, applies and teaches advanced methodologies of design and analysis to solve complex, hierarchical, heterogeneous and dynamic problems of engineering technology and systems for industry and government.*

*ISR is a permanent institute of the University of Maryland, within the Glenn L. Martin Institute of Technology/A. James Clark School of Engineering. It is a National Science Foundation Engineering Research Center.*

***Web site http://www.isr.umd.edu***

# REAL-TIME I*N-SITU* CHEMICAL SENSING, SENSOR-BASED FILM THICKNESS METROLOGY, AND PROCESS CONTROL IN W-CVD PROCESS

by

Yiheng Xu

Dissertation submitted to the Faculty of the Graduate School of the
University of Maryland, College Park in partial fulfillment
of the requirements for the degree of
Doctor of Philosophy
2000

Advisory Committee:

Professor Gary W. Rubloff, Chairman/Advisor
Professor Raymond A. Adomaitis
Professor John N. Kidder Jr.
Professor Gottlieb S. Oehrlein
Professor Lourdes G. Salamanca-Riba

DEDICATION

To my father who always loves me and supports me.

ACKNOWLEDGEMENTS

Dr. Theodosia Gougousi, Dr. John N. Kidder Jr., Laurent Henn-Lecordier, Ramaswamy Sreenivasan, Brian Conaghan, Dr. Yijun Liu, Soon Cho for support in experimental works, data analysis,and result discussion.

Dr. Louis Frees and Dr. Robert Ellefson (Inficon) for equipment supply and beneficial discussion.

Dr. Charles Tilford (NIST) for technical advice and enlightening questions.

TABLE OF CONTENTS

**List of Tables:**

List of Figures

# 1. Introduction

## *1.1: Sensor-based Metrology and Advanced Process Control in Semiconductor Process- Motivation, Challenge, and Trend.*

"The U.S. economy has undergone a fundamental shift in the 1990's. New industries dependent on innovation are now the source of jobs, income, and growth. Without warning, the U.S. has been transformed into a high technology economy that thrives on information appliances, high tech tools that enable people to communicate, and the creativity of a highly trained and entrepreneurial workforce. One technology outshines all the others and in fact, enables the others to prosper-the semiconductor. The tiny microchip drives virtually all-electronic products. Even the internet is, in reality, a world wide web of semiconductors."

Semiconductor Industry Association (SIA) Report, March 1998

Considering their far-reaching influence on our society in general and on our daily lives, it is not an overstatement that semiconductors and their applications represent one of the greatest scientific and technological breakthroughs of the twentieth century. These breakthroughs are possible thanks to the miniaturization of device dimensions, which allows the construction of compact systems with tremendous computing power and memory. As early as in 1964, Gordon Moore, later a co-founder of Intel Corp., noted that the number of transistors on a chip had doubled every 1.5 to 2 years or a fourfold increase every three years [i]. He also observed that the Microprocessor Unit (MPU) performance, i.e. millions of instructions per second (MIPS), doubles every 1.5 to 2 years, and the line-width shrinks by a factor of 2 every 5-6 years. (Table 1.1 [ii] & Table 1.2 [i]) This trend,

known as the Moore's Law, has become a key indicator of successful leading-edge semiconductor products and companies.

Table 1.1: Evolution of IC processing features

| Year of Production | 1980 | 1984 | 1987 | 1990 | 1993 | 1996 |
|---|---|---|---|---|---|---|
| Wafer size (mm) | 75 | 100 | 125 | 150 | 200 | 200 |
| Technology (DRAM) | 64K | 256K | 1M | 4M | 16M | 64M |
| Chip size ($cm^2$) | 0.3 | 0.4 | 0.5 | 0.9 | 1.4 | 2.0 |
| Feature size (nm) | 2000 | 1500 | 1000 | 800 | 500 | 350 |

Table 1.2: Projected technology node

| Year of Production | 1999 | 2002 | 2005 | 2008 | 2011 | 2014 |
|---|---|---|---|---|---|---|
| Line width, (nm) | 180 | 130 | 110 | 70 | 50 | 35 |
| Gate length (nm) | 140 | 85-90 | 65 | 45 | 30-32 | 20-22 |
| Oxide thickness (nm) | 1.9-2.5 | 1.5-1.9 | 1.0-1.5 | 0.8-1.2 | 0.6-0.8 | 0.5-0.6 |
| Junction depth, (nm) | 47-70 | 25-43 | 20-33 | 16-26 | 11-19 | 8-13 |
| Interconnect dielectric k | 3.5-4.0 | 2.7-3.5 | 1.6-22 | 1.5 | <1.5 | <1.5 |

In addition to Moore's Law, there is a historically based "corollary" which suggests that, to be competitive, manufacturing productivity improvements must also enable the cost per bit/transistor to decrease by about 29% per year [iii]. In order to

remain competitive, two approaches have been taken in parallel by the industry: increasing the wafer size and enhancing Overall Equipment Effectiveness (OEE). As the industry moves to the larger wafer size and shrinking device dimension, it has learned that loss of processed wafers due to delayed detection of equipment/process problems can lead to severe financial consequences. Real-time *in-situ* process monitoring, sensor-based metrology, and advanced process control (APC) are thus needed for cost-effective device manufacturing. Real-time *in-situ* process monitoring and metrology offer timely diagnostics information regarding the process status and equipment status [iv]. Now various techniques are currently in use or under development for *in-situ* process monitoring and metrology, for instance compact particle detector [v], multichannel spectroscopic ellipsometry [vi], optical emission spectroscopy (OES), and quadrupole mass spectrometry (QMS) [vii]. Each technique has its limitation. For example, compact particle detector suffers from the inability to accurately measure or monitor the in-film particulate due to the surface roughness of the film [v] and it offers few clues to the reason for particle generation. Optical emission spectroscopy (OES) has been widely used to monitor process endpoint in plasma etching, but its nonlinearity associated with the plasma is an obstacle to quantification. QMS has been recognized as an excellent sensor for leak detection and contamination control over an extended period of time owing to its high chemical sensitivity, and it has been pursued for further semiconductor manufacturing applications. Today's QMS finds its applications ranging from endpoint detection in dielectrics etching [viii] to film thickness metrology in metallization [ix]. Table 1.3 summarizes the potential applications of mass spectrometry as an *in-situ* sensor in physical vapor deposition (PVD), chemical vapor deposition (CVD), and etch

processes. The next logical step for this instrument is to provide real-time process control based on *in-situ* measurements of gaseous species [x]. The issues preventing the application of QMS in production lines, such as the need for better sensor-to-sensor matching, calibration standards, data management and integration, are gradually being overcome.

To facilitate sensor-based process control, signals from the *in-situ* sensors are routed to the process control system. With the information from sensors, APC helps to reduce the manufacturing costs by reducing process variation, reducing send-ahead and tool monitor wafers, shortening learning cycles and response-time, enabling better tool matching in high-volume production, improving OEE, shortening development times, and easing process transfer from pilot line to factory [xi]. Take the real-time process control (RTPC) system implemented at IBM-Burlington for example. The RTPC, which monitors more than 275 process tools saved more than $10 million on a total investment of less than $3 million over the past four years [xii]. Another good example of successful application of *in-situ* sensors is the 25% throughput improvement that sensor-based advanced process control brings to small batch, fast ramp furnaces [xiii].

Table 1.3: Potential application of Mass Spectrometry in IC fabrication.

| Transpctor Gas Analysis System | PVD | | CVD | | ETCH | |
|---|---|---|---|---|---|---|
| | Tool State | Process State | Tool State | Process State | Tool State | Process State |
| RGA(Open Ion Source): C100F/M, H100F/M, H200F/M, H300F/M Detection limit 100ppm | Leak detection MFC leaks Gas line leaks Chamber outgassing | Argon flow Reactive gas flow($N_2$ $O_2$) Gas supply contamination MFC instability Photoresist contamination | Leak detection MFC leaks Gas line leaks Chamber outgassing | Carrier gas flow Precursor gas flow Delivery system stability Gas supply contamination Monitor chamber clean endpoint Photoresist contamination | Leak detection MFC leaks Gas line leaks Chamber outgassing | Carrier gas flow Reactive gas flow Gas supply contamination MFC instability Monitor selectivity Monitor endpoint |
| Process gas Analyzer (XPR) Detection limit 10ppm | Leak detection MFC leaks Gas line leaks Chamber outgassing | Argon flow Reactive gas flow($N_2$ $O_2$) Gas supply contamination MFC instability | N/A | N/A | N/A | N/A |
| RGA( CIS) H100CIS H200CIS H300CIS Detection limit <1ppm | Leak detection MFC leaks Gas line leaks Chamber outgassing | Argon flow Reactive gas flow($N_2$ $O_2$) Gas supply contamination MFC instability Photoresist contamination Target impurity | Leak detection MFC leaks Gas line leaks Chamber outgassing | Carrier gas flow Precursor gas flow Delivery system stability Gas supply contamination Monitor chamber clean endpoint Photoresist contamination | Leak detection MFC leaks Gas line leaks Chamber outgassing | Carrier gas flow Reactive gas flow Gas supply contamination MFC instability Monitor selectivity Monitor endpoint |

The semiconductor industry which moved a year or two years ahead of Moore's Law, with the pace particularly quickening in the last five years, is pushing the limits of measurement capability as it approaches the next technology generation of 100nm and beyond. Future challenges come from the high aspect ratio structures, ultra thin layers, ultra-shallow junctions combined with the use of new materials for transistor, capacitor and on-chip interconnect. Table 1.4 illustrates the major near-term interconnect metrology challenges before 2005 [xiv]. To meet the requirement of the desired device scaling and manufacturing costs, metrology must keep up with new processes. The metrology tools must be capable of measurement with sufficient resolution and solutions to the metrology difficult challenges need be explored. Research and development of new metrology tool used to be the concerns only to the metrology suppliers, which are usually small companies that find the cost of providing new metrology tools for leading-edge activities prohibitive. Recently a favorable transition is taking place. More and more semiconductor equipment manufacturers such as Applied Materials Inc. are joining with the metrology suppliers to address the metrology challenges. Electronic News on July 10,2000 featured an interview with Jim Morgan, Applied's CEO. At the end of the interview, he emphasized that "Applied plans to continue to conquer new markets. What we are currently working on this year is to expand our presence in metrology and inspection." The development of new sensors with wider capabilities, ensured by the involvement of equipment manufacturers, is bringing integrated and *in-situ* metrology capabilities closer to reality. Some off-line metrologies are being replaced with real-time *in-situ* metrologies that greatly shorten the time to determine process performance, a key

parameter for metrology solutions. At the same time, single measurement is no longer enough. Industrial sensors on the stand-alone equipment are being replaced by the

Table 1.4: Near-term interconnect metrology challenges.

| Year | 1999 | 2000 | 2001 | 2002 | 2003 | 2004 | 2005 |
|---|---|---|---|---|---|---|---|
| Technology node | 180nm | | | 130nm | | | 100nm |
| Dram 1/2 pitch | 180 | 165 | 150 | 130 | 120 | 110 | 100 |
| MPU gate length | 140 | 120 | 100 | 85 | 80 | 70 | 65 |
| Planarity requirements: Minimum interconnect CD (nm)<br>Measurement precision (nm) | 250<br>+- 25 | 250 | 250 | 200<br>+- 20 | 200 | 200 | 175<br>+- 17 |
| Measurement of deposited barrier layer at thickness (nm)<br>process range | 17<br>10% | 16<br>10% | 14<br>10% | 13<br>10% | 12<br>10% | 11<br>10% | 10<br>10% |
| Measure inter-level metal insulator effective dielectric constant (k) and anisotropy on patterned structures at 5x to 10x local clock frequency (GHz) | 3.5-4.0<br>1.25 | 3.5-4.0 | 2.7-3.0 | 2.7-3.0<br>2.1 | 2.2-2.7 | 2.2-2.5 | 1.6-2.2<br>3.5 |

integrated sensors on systems in the real manufacturing environment. Clustered sensors incorporated in various processes produce a great wealth of data, which, in a nature way, raises a question: how to manage and utilize the data efficiently. Improvement must be

done on the data integration, data analysis automation, and decision support system. A new concept that the metrology community is talking about is integrated metrology, defined as the move toward greater use of measurement data for automated process control, which requires cooperation among metrology suppliers, tool manufacturers, chipmakers and experts with information technology background.

Material complexity and geometrical shrinkage are also metrology drivers. The emerging 300mm wafer processing reinforces the necessity of effective metrology solution. As the semiconductor industry moves down the road to the territory full of uncertainty, metrology validated at a system level is needed to sustain its miraculous exponential growth in the new millennium.

### *1.2: Scope and Goal of this Research.*

This research is aimed at implementing mass spectrometry for real-time *in-situ* chemical sensing in CVD process, establishing wafer state metrology from integrated mass spectrometry signals of different gaseous chemical species in the reaction, and demonstrating and assessing benefit from combining real-time mass spectrometry sensor data with equipment state information to achieve benefits in process control and fault classification. It focuses on a limited subset of options for realizing APC in order to emphasize methods for integrating key pieces and to provide clear pathways to manufacturing benefit. This research is a natural extension of the prior Semiconductor Research Corporation sponsored research at North Carolina State University on chemical sensing, metrology and optimization using *in-situ* mass spectrometry in poliSi and oxide RTCVD. The process under study now is tungsten CVD (W-CVD) on Ulvac-ERA1000, a manufacturing tool. The goals of the research are:

1. To apply real-time, in-situ mass spectrometry to W-CVD processes in a manufacturing cluster tool and to characterize the processes of different reaction mechanisms --- real-time in-situ chemical sensing;
2. To build a data acquisition system to collect data from the equipment auxiliary sensors synchronized with the mass spectrometry signals --- sensor integration;
3. To establish the wafer state metrology using mass spectrometry signals --- W thickness metrology;
4. To demonstrate run-to-run control and real-time end point control methods in concert with mass spectrometry data --- sensor-based process control;
5. To develop a fault-trapping algorithm for selected mechanisms --- fault management.
6. Achievement of these specific goals will illustrated the value of *in-situ* chemical sensing in complex manufacturing process systems and provide clear pathways toward APC methodology.

### *1.3: Organization of the Thesis*

The thesis consists of five more chapters in addition to this introductory chapter

Chapter 2: The W-CVD processes are reviewed, followed by an description of the operating theory of mass spectrometry and its application in semiconductor processing. Finally a brief introduction of the Internal Model Control algorithm for process control is given.

Chapter 3: The experiment procedure is covered in this section. We begin with the presentation of the Ulvac-ERA 1000 W-CVD cluster tool used in this research for

tungsten thin film deposition. Then the implementation of the mass spectrometry sampling system for real-time *in-situ* process monitoring is discussed in detail. The data acquisition system built on the LabView® platform for sensor integration is also described.

Chapter 4: Chapter 4 is the core section of this thesis, in which the results of W thin film thickness metrology and process control (run-to-run and real-time control) obtained in both $H_2$ reduction of $WF_6$ and $SiH_4$ reduction of $WF_6$ processes are shown. A fault-trapping algorithm is illustrated for one selected mechanism involving wafer surface cleanliness.

Chapter 5: This chapter provides a further discussion regarding the real-time *in-situ* chemical sensing using mass spectrometry in a multi-component reaction system like W-CVD process.

Chapter 6: The thesis is concluded with a summary of the contributions of this research and some thoughts of possible future works.

## 2. Real-time *in-situ* Chemical Sensing, Sensor-based Thin Film Thickness Metrology and Process Control in W-CVD Process Using Mass Spectrometry.

Chemical vapor deposition, defined as the formation of the desired nonvolatile thin film on the substrate from the gaseous precursors containing the required constituents by chemical reaction is widely used for thin film synthesis in integrated circuit (IC) fabrication. With good control of the process parameters, it provides a way to deposit high quality films with excellent step coverage, which is critical to devices having small feature size and high aspect ratio patterns. Polysilicon, silicon dioxide, silicon nitride, and refractory metal films like W are routinely deposited using this technique. The CVD processes can be categorized differently using different criteria. For example, by pressure regime of operation, chemical vapor deposition can be classified into atmosphere-pressure CVD (APCVD) and low-pressure CVD (LPCVD), while according to the source of the energy for the chemical reaction, it falls into thermal CVD (TCVD) and plasma enhanced CVD (PECVD). Table 2.1 illustrates the characteristics and applications of the most common CVD processes [xv]. Another important CVD process not included here is atomic layer deposition, which finds its application in area such as high k dielectric materials and in semiconductor epitaxy.

Table 2.1: Characteristics and applications of CVD processes.

| Process | Advantages | Disadvantages | Applications |
|---|---|---|---|
| APCVD | Simple reactor, fast deposition, low temperature | Poor step coverage, particle contamination low throughput | Low-temperature oxide |
| LPCVD | Excellent purity and uniformity, conformal step coverage, large wafer capacity, high throughput | High temperature, low deposition rate | High-temperature oxides, silicon nitride, poly-Si, W, $WSi_2$ |
| PECVD | Low temperature, fast deposition, good step coverage | Chemical and particle contamination | Low-temperature insulators over metals, passivation (nitride) |

Whatever types the processes belong to, five steps almost always occur in all CVD reactions as depicted in Figure 2.1 [xvi]. Take the W-CVD process from $WF_6$ and $SiH_4$ mixture for example. The five steps are:

1. Transport of reacting gaseous species: $WF_6$ and $SiH_4$ to the substrate surface
2. Absorption or chemisorption, of the species: $WF_6$ and $SiH_4$ on the substrate surface
3. Heterogeneous surface reaction at the substrate surface
4. Desorption of gaseous reaction products : $SiF_4$ and $H_2$
5. Transport of reaction products: $SiF_4$ and $H_2$ away from the substrate surface.

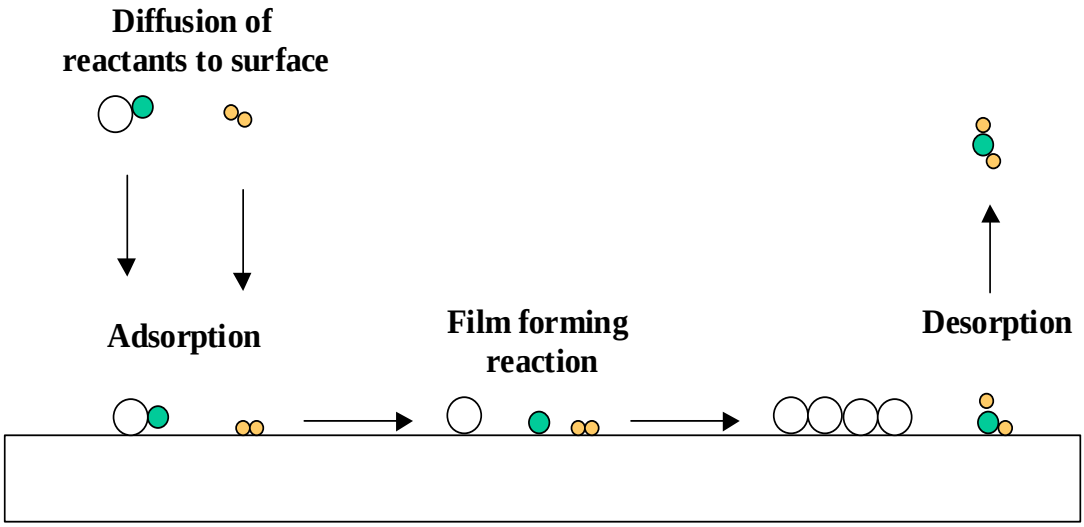


Figure 2.1: The sequence of reaction steps in a CVD reaction.

Each of the five steps above can be the rate-limiting step depending on the chemistry and process parameters, e.g. temperature. Generally speaking, at low deposition temperature, the process is in the kinetic-limiting regime and the deposited film will show better step coverage. As the temperature goes up, the transport step will start to become the rate-limiting step.

In this research, W thin film was deposited in a lamp heated single wafer cold wall W-CVD cluster tool. The gaseous products and reactants involved in the reaction were monitored using mass spectrometry. The obtained mass spectrometry signals were applied for W thin film thickness metrology and process control. Later in this chapter, W-CVD processes of different reaction mechanisms will be reviewed first. A good understanding of reaction mechanisms is of great importance for both process and metrology development. Following that will be an introduction of the mass spectrometry.

It answers three fundamental questions: how it works, how to interpret the signals, what is its significance for semiconductor process? Finally we conclude this section with a description of the IMC run-to-run control algorithm.

## *2.1: Fundamentals of W-CVD Process*

### 2.1.1: Application of W-CVD Process in Semiconductor Process.

Microprocessors (MPUs) are multi-layers structures. A high number of metal layers facilitate the communication between different layers. (Figure 2.2 [xvii]). In order to accommodate on-chip de-coupling capacitors, the growth of metal levels is projected to increase even beyond those specified solely to meet performance specifications. Generally speaking, the good materials appropriate for interconnect (including contact) application must show low resistivity, have good adhesion to Si and $SiO_2$, and maintain stability in the succeeding processes. Refractory material W is widely used for contact and via filling in IC fabrication because of its refractory nature. No reaction between Si and W is likely under normal processing temperature and W does not suffer from electromigration as Al does. Although Cu is going to substitute for Al and W gradually in the higher levels of the hierarchical wiring structure in the forthcoming era of copper, W will still find its place in the contact level.

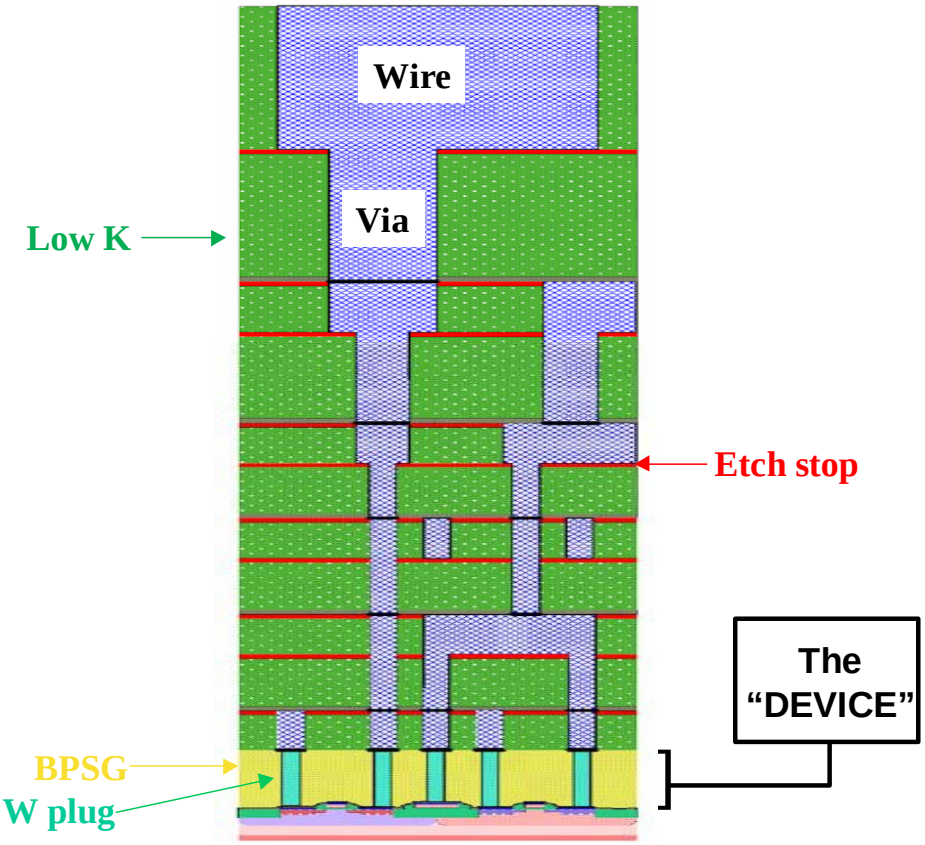


Figure 2.2: Typical MPU cross section showing Cu replaces W for via filling and W is still used in the bottom level for contact filling.

W thin film can be obtained by different chemical reactions among which Si reduction of $WF_6$, $H_2$ reduction of $WF_6$, and $SiH_4$ reduction of $WF_6$ are the most important. $WF_6$ can also react with other metal surfaces such as Al and Ti to deposit W thin film. Actually the reaction rate between $WF_6$ and the metal surface (including Si) is even higher than that of reactions using $H_2$ or $SiH_4$ as reducing agent. Table 2.2 [xviii] gives the Gibbs free energies of different W-CVD processes, which can be calculated out from the standard thermo-chemical tables.

Table 2.2: Free energy changes for W-CVD process.

| Reaction | ΔG at 500k (KJ/g-atom W) |
|---|---|
| $WF_6 + 3H_2 \longrightarrow W + 6HF$ | -113 |
| $WF_6 + 1.5\ Si \longrightarrow W + 1.5\ SiF_4$ | -478 |
| $WF_6 + 1.5\ SiH_4 \longrightarrow W + 1.5\ SiF_4 + 3H_2$ | -870 |
| $WF_6 + 1.5\ Ti \longrightarrow W + 1.5\ TiF_4$ | -1037 |
| $WF_6 + 2\ Al \longrightarrow W + 2\ AlF_3$ | -1162 |

The currently accepted CVD method for high aspect ratio contact W fill is a two-step process using combinations of $WF_6$, $SiH_4$, $H_2$, and Ar. The first step referred to as seed layer deposition uses $SiH_4$ to reduce $WF_6$. Following that $H_2$ will be introduced to react with $WF_6$ for sustained W growth. Compared with $SiH_4$ reduction, $H_2$ reduction process generally results in more conformal film [xix]. Usually two different CVD processes are available for W metallization: blanket W-CVD process and selective W-CVD process. As illustrated in Figure 2.3, [xviii], in selective W-CVD process, W thin film is selectively deposited in the contact regime but not on the insulator. While in blanket W-CVD process, W thin film is deposited on the entire wafer and chemical mechanical polishing (CMP) or W dry etching is used following the deposition to remove the W thin film on the insulator and leave W only in the contact region. Blanket W-CVD process with CMP is today's industrial standard for W plug process to avoid the selectivity loss. In the following sections, W-CVD processes using different reduction agents will be reviewed in details.

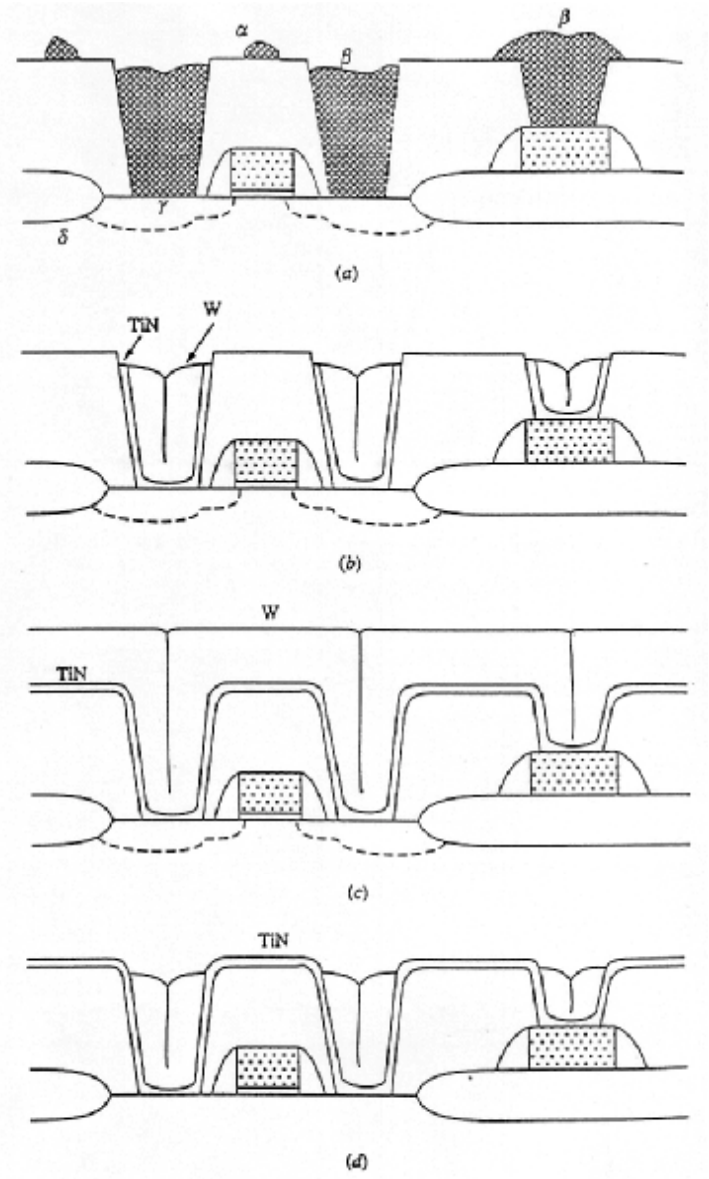


Figure 2.3: CVD W plug processes. (a) Selective W with no barrier layer. (b) Selective W with barrier layer of TiN. (c) Blanket deposition of W on TiN layer. (d) After W etch-back to form W plugs.

### 2.1.2: W-CVD Process by Si-Reduction.

As indicated in the Table 2.2, reaction between $WF_6$ and heated Si wafer surface is thermodynamically favorable. The chemistry is straightforward and can be presented

by the following equations 2-1 & 2-2 for low and high deposition temperature respectively [xx].

$$2WF_6 + 3Si \longleftrightarrow 2W + 3SiF_4\,(g) \qquad (2\text{-}1)$$

$$WF_6 + 3Si \longleftrightarrow W + 3SiF_2\,(g) \qquad (2\text{-}2)$$

Si reduction of $WF_6$ is a self-limiting process. Two different observations have been reported regarding the temperature dependence of the W film thickness by Si reduction reaction. Leusink et al. noted that the W film thickness by Si reduction of $WF_6$ shows Arrhenius-type temperature behavior, ranging from 10nm at 580 K to about 200 nm at 700K [xxi]. The mechanism they proposed suggests that once the Si surface is covered by a seed layer of W, Si has to diffuse through the W film to the surface to get reacted with $WF_6$ for further W deposition. The temperature dependence of the Si diffusion explains the Arrhenius-type temperature dependence of the final layer thickness. Another observation indicated that the W film thickness is around 15-20 nm, independent of the deposition temperature [xxii, xxiii]. Groenen et al. attributed the fixed W layer thickness to the excessive supply of $WF_6$, which forms a layer of $W_xSi_yF_z$ as Si wafer is first exposed to the $WF_6$. Later this layer will be gradually converted to the W and thus results in a layer of W of fixed thickness. The simulation results based on their proposed model match their observation.

W film deposited by Si reduction reaction shows attractive low contact resistance, however the consumption of Si during the process causes localized etching of Si surface, i.e. wormhole formation. To make it worse, lateral growth of W occurs under $SiO_2$ along $SiO_2$/Si interface, which may give rise to reliability problems if contacts are in close proximity. Although these drawbacks prevent its application in IC fabrication, Si

reduction reaction always happens and influences other W-CVD deposition on Si, especially in the initial stage.

### 2.1.3: W-CVD Process by $H_2$-Reduction.

Extensive research has been done on the W-LPCVD process by $H_2$ reduction of $WF_6$ (equation 2-3), which is capable of filling high aspect ratio features with excellent step coverage.

$$WF_6 + 3H_2 \longleftrightarrow W + 6HF(g) \qquad (2\text{-}3)$$

This reaction can be initiated on metal surface that is capable of activating $WF_6$ and $H_2$ through dissociative adsorption. The deposition process usually carried out at 300 to $550^0$C and 0.1 to 100 torr shows deposition rate ranging from $10^1$ to $10^3$ nm/min. The flow rate ratio of $H_2/WF_6$ affects the kinetic behavior of the reaction greatly. It is found that in the high flow rate ratio regime of $15 > P_{H2}/P_{WF6} > 4.5$, deposition rate has a zero order dependence with respect to the $WF_6$ partial pressure, and one-half order dependence with respect to the $H_2$ partial pressure, which could be formulated by equation 2-4

$$r = K_r P_{H2}^{1/2} P_{WF6}^{0} \qquad (2\text{-}4)$$

Where r is the growth rate, Kr symbolizes the rate constant exhibiting an Arrhenius-type temperature dependence, and P represent partial pressures of $H_2$ and $WF_6$. The observed activation energy of $K_r$ varies from 69 to 73 KJ/mole [xxiv].

At the lower ratio regime for instance $P_{H2}/PW_{F6} < 3$, the dependence of deposition rate on the $H_2$ partial pressure was found to change from 0.5 to 1 and the activation

energy is only about 20 KJ/mole. It was demonstrated that these phenomena are not due to the mass transfer limitations, but rather are determined by surface reaction kinetics.

To explain the kinetics of film deposition by $H_2$ reduction, similar models have been proposed by McConica et al and Pauleau et al [xxv-xxvi], assuming that desorption of the reaction product HF is the rate limiting step (equation 2-5) with WF* as the most abundant surface intermediate (masi) at high ratio regime and $H_2$ dissociation be the rate limiting step (equation 2-6) with F* as the masi at low ratio regime. Their models result in expressions for deposition rate, which match experimental observation quite well. However since the presence of undissociated chemisorbed HF on the tungsten surface is not likely according to the theoretical calculations of Arora and Pollard [xxvii], HF is considered to desorb directly in the elementary step in which the H-F bond is formed. The formation of HF according to equation 2-7 appears to be the most probable rate-limiting step.

$$HF^* \longleftrightarrow * + HF(g) \qquad (2\text{-}5)$$

$$H_2(g) + 2^* \longleftrightarrow 2H^* \qquad (2\text{-}6)$$

$$H^* + F^* \longleftrightarrow 2^* + HF\ (g) \qquad (2\text{-}7)$$

Although larger deposition rate and higher conversion rate of $WF_6$ can be achieved at high $P_{H2}/P_{WF6}$ ratio regime, it is favorable to have deposition in the relatively low ratio regime. Hasper et al. reported optimized step coverage at reactant ratio of approximately 4 [xxviii]. Our research results indicate that reactant ratio of 4 is also optimal for the film thickness metrology development using mass spectrometry.

$H_2$ reduction process suffers from the same problem as Si reduction process, because the reaction product HF can attack $SiO_2$ and $WF_6$ is ready to etch Si even in the presence of $H_2$. A barrier layer e.g. TiN is required prior to the W deposition to shield $Si/SiO_2$ from $HF/WF_6$. This drawback prompts people to look for other reducing agents for $WF_6$-based W-CVD. Different reactants have been explored, such as $GeH_4$ and $SiH_2F_2$, $SiH_4$ proves to be superior and is widely used in industry especially for seed layer deposition.

### 2.1.4: W-CVD Process by $SiH_4$-Reduction.

The first use of $SiH_4$ as the reducing agent for W-CVD process was recorded in the Japanese patent application of Furuyama and Moriya [xxix]. The reaction can be expressed by the following two equations 2-8 [xxx] & 2-9 [xxxi].

$$3SiH_4 + 2WF_6 \longleftrightarrow 2W + 3SiF_4 + 6H_2 \qquad (2\text{-}8)$$

$$2SiH_4 + WF_6 \longleftrightarrow W + 2SiHF_3 + 3H_2 \qquad (2\text{-}9)$$

As opposed to the Si reduction and $H_2$ reduction processes, $SiH_4$ reduction process is not plagued with the problem caused by the consumption of Si. Another advantage related to this process is that it offers a much higher deposition rate and thus the deposition temperature can be lowered down to control the thermal budget but still maintain acceptable deposition rate. This is extremely important for the shallow junctions needed in 0.25um technology and beyond. However since there is no Si consumption in the $SiH_4$ process, the adhesion between W film and the substrate is poor. Fortunately the barrier layer (TiN) beneath W serves as a glue layer and provides good adhesion for W film.

Research work of Yu et al. [xxxii] indicates that the $SiH_4$ reduction process proceeds like this: $SiH_4$ first reacts with the fluorine-covered surface to form a silicon layer and gaseous products such as $H_2$, $SiF_4$ and HF will be evolved. Next $WF_6$ reacts with this Si layer and deposits a new W layer. The reaction then repeats the Si and W deposition cycles to sustain W film growth. X-ray diffraction analysis demonstrated the formation of polycrystalline α-W at $P(SiH_4)/P(WF_6) =< 1$. Increasing the ratio to higher values resulted in W film consisting of a mixture of α-W and β-W [xxxiii]. Compared with β-W, α-W is more desirable because of its low resistivity. McInerney et al. [xxxiv] also reports the onset of gas phase reaction above the threshold ratio of $P(SiH_4)/P(WF_6)=1$. Therefore the ratio of $P(SiH_4)/P(WF_6)$ is kept below one in most of our studies.

Even though the deposition rates appearing in the literature are not entirely keep consistent, usually the deposition rates show a first order dependence on $SiH_4$ and a zero or slightly negative order dependence with respect to $WF_6$ for the low ratio regime of $P(SiH_4)/P(WF_6)<0.3$ [xxxv, xxxvi]. See equation 2-10.

$$r = Kr\, P^{1}_{SiH4} P^{n}_{WF6} \qquad (2\text{-}10)$$

Where n is a small number between -0.2 and 0. In the temperature region of 145 to $395^0$C, the Arrhenius plots are nolinear with maximum deposition rates near $300^0$C [xxxiii]. The apparent activation energies of 27KJ/mole ($150\text{-}200^0$C), 50KJ/mole ($450\text{-}500^0$C) [xxxv] and 28KJ/mole ($300\text{-}500^0$C) [xxxvii] have been reported. As the ratio of $P(SiH_4)/P(WF_6)$ approach one, the dependence of deposition rate on $P_{SiH4}$ and $P_{WF6}$ change to second order and minus-first order respectively [xxxiii]. Different models have been proposed to interpret the kinetic behavior of $SiH_4$ reduction process, which fall into three different categories: Langmuir-Hinshelwood model (L-H model), Eley-Rideal

model (E-R model), and Steady-state Approximations model (S-A model). In accordance with the L-H model, the proposed surface reactions involve only chemisorbed species. Ammerlaan [xxxiii] pointed out that L-H model could explain the kinetic behavior of $SiH_4$ reduction process at the region of $P_{SiH4}/P_{WF6} =< 0.3$, assuming that the dissociative adsorption of $SiH_4$ is the rate-limiting step. However the kinetics transition at the higher $P_{SiH4}/P_{WF6}$ region, i.e. the change from the first and small negative order dependence to the almost second and minus-first order dependence, could not be derived from the L-H model. Using E-R mechanism, Hsieh developed a model for which the simulation results match the experiment results published by Rosler et al [xxxv]. Based on the recognition that there may be more than one non-equilibrated step in the process, another approach in modeling was taken by Ammerlaan [xxxiii]. In contrast with L-H model and E-R model, the reaction pathway comprise several non-equilibrated steps and the adspecies can occupy multiple sites on the surface. The deposit rate expressions obtained shows excellent agreement with the experimental observation as illustrated by equations 2.11 & 2.12 below [xxxiii].

Low ratio region: $r = K [P_{SiH4}]^{12/11} [P_{WF6}]^{-1/11}$ (2-11)

High ratio region: $r = K [P_{SiH4}]^{2} [P_{WF6}]^{-1}$ (2-12)

In order to explain the non-linear arrhenius plots with maximum deposition rate at around $300^0$C, the concept of mobile precursor state is invoked. Dissociative chemisorption of a molecule occurs via a precursor state, which is stabilized by physisorption interactions with the surface. The chemisorption won't happen unless the mobile precursor diffuses on the surface and encounters unoccupied sites before it desorbs. So when the energy for desorption from precursor state is higher than the

activation energy for transition to the chemisorbed state, the chemisorption rate of the species will decrease with the temperature, which leads to a negative value of the apparent activation energy as in $SiH_4$ reduction process.

### *2.2: Fundamentals of Mass Spectrometry.*

Mass spectrometry is a microanalytical technique with high sensitivity and chemical selectivity requiring only a few nano-moles of sample to obtain characteristic information regarding the molecular weight and the structure of the analyte . The four most common mass spectrometry types are magnetic, quadrupole, time-of flight, and ion cyclotron, among which quadrupole mass spectrometry has been widely implemented as an invaluable analytical tool for process contamination identification, gas purity analysis, vacuum system leak detection, chemical reaction verification, photoresist detection, endpoint detection, tool diagnostics, and preventive maintenance in semiconductor manufacturing. More advanced application of mass spectrometry was demonstrated by Greve et al.[xxxviii] and Evans et al.[xxxix]. Greve et al. established a closed-loop control system in PECVD silicon nitride process based on species concentration measured by quadrupole mass spectrometry, while Evans et al. applied it for closed-loop control in molecular beam epitaxy (MBE). In our research quadrupole mass spectrometry is employed as a real-time *in-situ* monitoring tool in W-CVD process in attempts to develop sensor-based W film thickness metrology and process control. In the next two subsections, an introduction regarding mass spectrometry operation theory and mass spectrometry data interpretation will be given.

### 2.2.1: Theory of Operation of Mass Spectrometry.

Mass spectrometry consists of two components: sensor that functions only under high vacuum and an electronics module, which operates the sensor. The Inficon Transpector sensor (H300amu and H200amu) includes three parts, see Figure 2.4 [xl].

1. Ionizer (ion source)
2. Quadrupole mass filter
3. Ion detector

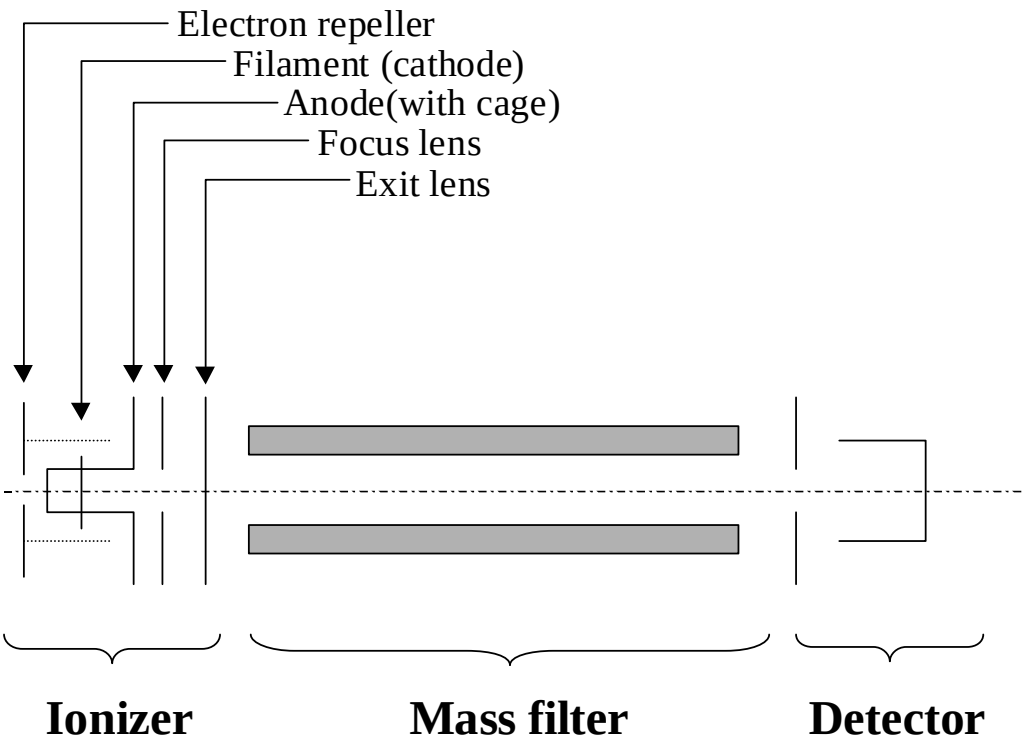


Figure 2.4: Schematic of the sensor of quadrupole mass spectrometry.

The sensor analyzes gases by ionizing some of the gas molecules (in the ion source) and separating the ions by mass/charge ratio (in the mass filter). The mass/charge ratio is unique for each substance and can be used to identify the gas molecules from which the ions were created. The magnitudes of ion current detected by ion detector are used to determine the partial pressures of the corresponding gases.

### Ion source

The structure of ion source is depicted in Figure 2.4. Inside the ion source, a heated filament emits electrons, which all accelerated to energies sufficient to ionize them and give them electrical charge. The filament usually is made of iridium with either a thorium-oxide or yttrium-oxide coating, which can be turned on in high pressure

without undergoing instantaneous destruction. However when fluorine or chlorine containing species are present, a tungsten filament is the more desirable choice. The term "emission current" refers to the stream of electrons emitted by the heated filament and usually is below several thousand microamperes. Emission current need be controlled precisely to keep the measurement of the mass spectrometry stable. The anode is positive with respect to the filament and the potential between the anode and filament is determines the electron energy, which in turn determines how the gases will be ionized by the electron. By adjusting the electron energy, it is possible to distinguish the ions of the same mass/charge ratio but from different species. For example, ions of 20amu could be $HF^+$ or $Ar^{2+}$. If the ions are $Ar^{2+}$, then the ion current will reduce to background level after the electron energy is lowered to 35ev, which is below 43.5ev, the minimum energy required to remove two electrons from Ar to produce $Ar^{2+}$. The ions exit the ion source through the source exit lens negatively biased with respect to anode. The potential difference between source exit lens and anode is the ion energy.

### Mass filter

Mass filter is the core of mass spectrometry. The mass filter in a quadrupole mass spectrometer consists of 4 cylindrical rods positioned in a square array. Ions from the ion source will be subject to the electrical field in the mass filter and only those of specific mass/charge ratio will pass the mass filter and be detected by the ion detector. A combination of DC and RF voltage is added to the two pairs of rods as indicated by the following two equations.

$$X = V\cos(\omega t) + U \qquad (2\text{-}13)$$

$$Y = V\cos(\omega t + \pi) - U \qquad (2\text{-}14)$$

The applied DC and RF voltages create an electric field inside the ionizer as expressed by equation 2-15[xli] .

$$\Phi = (U + V\cos\omega t)(x^2 - y^2)/r_0^2 \qquad (2\text{-}15)$$

The force imposed on the ions by the above field is

$$F_x = zE_x = -z\frac{\partial \Phi}{\partial x} = -z(U + V\cos\omega t)x / r_0^2 \qquad (2\text{-}16)$$

$$F_y = zE_y = -z\frac{\partial \Phi}{\partial y} = z(U + V\cos\omega t)y / r_0^2 \qquad (2\text{-}17)$$

$$F_z = 0 \qquad (2\text{-}18)$$

The trajectory of the ions in the mass filter will be derived from the following second order partial differential equations, so called Mathieu's differential equations.

$$M\ddot{x} = F_x = -z(U + V\cos\omega t)x / r_0^2 \qquad (2\text{-}19)$$

$$M\ddot{y} = F_y = z(U + V\cos\omega t)y / r_0^2 \qquad (2\text{-}20)$$

$$M\ddot{z} = 0 \qquad (2\text{-}21)$$

Solving these equations, we will get two sets of solutions: (i) the stable solutions for which x and y remain finite for all values of time, t, and (ii) the unstable solutions for which x and y become infinite as t approaches ∞. The unstable solution means that the ions will oscillate with the electric field, hit the rods, and be annihilated, while the stable solution means the ions can pass the mass filter and be

detected by the ion detector. Figure 2.5 [xli] shows the stability region for quadrupole mass filter. Where $\alpha=4zU/m\omega^2r_0^2$, $q=2zv/m\omega^2r_0^2$.

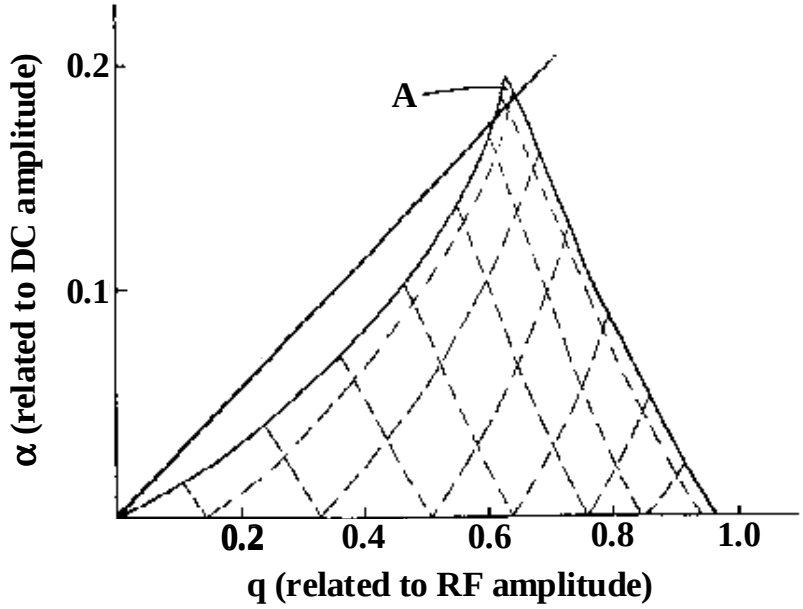


Figure 2.5: Stability diagram for quadrupole mass filter.

For fixed U, V, ω, and $r_0$, only ions of certain mass/charge ratios fall into the stability region of the above figure. The value of $\beta = U/V=\alpha/2q$ defines how wide that mass range can be. Usually to achieve high resolution, a fixed β value of 0.168 is selected. During the measurement, masses can be scanned from low mass region to high mass region by either varying the frequency while keeping RF and DC voltage constant or by adjusting the RF and DC voltage proportionally in accordance with the β value ($\beta = 2U/V = 0.168$) while keeping frequency fixed. Nowadays, almost all quadrupole mass spectrometry belongs to the second type, for it is much easier to vary the voltage rather than the high frequency.

### Ion detector

The ion detector detects ions passing the mass filter and it can be a simple Faraday Cup (FC), Electron Multiplier (EM), or a combination of both, e.g. Channel Electron Multiplier/Faraday Cup Detector (CEM/FC). The Faraday cup typically is a metal plate or a cup-shaped electrode, on which ions impinge and get neutralized. The current it draws from the connected circuit due to the neutralization of the impinged ions is equal to the ion beam current hitting the detector. FC is a simple, cheap, and stable detector. However its low sensitivity limits its application. Electron multiplier acts as a preamplifier for sensitivity improvement. When an ion accelerated by the EM voltage (1 KV or larger) strikes the EM surface, it will generate one or more electrons. This amplification process is repeated itself so that a large number of electrons can result from one incident ion. EM usually is placed before the FC, which measures the electron output current of EM. The ratio of the electron output current to the incident ion current is defined as EM gain. The drawback for EM is that its gain can degrade after being exposed to high pressure. The Channel Electron Multiplier/Faraday Cup detector is a combination of FC and EM. Its improvement over EM is that it uses continues dynode element made of a special type of glass rather than the traditional discrete dynode EM. Thus it has a longer lifetime compared with EM. Nevertheless, fluorine-contained species can attack CEM and cause degradation too.

## 2.2.2: Qualitative and Quantitative Interpretation of Mass. Spectrometry Data.

Interpretation of mass spectrometry data requires a good understanding of the ionization process that gases undergo within the ion source. For most of the gas molecules, it is very likely that electron bombardment by 70ev (or larger) electrons will

cause both dissociation and ionization. Illustrated below are just a few examples that may occur in the ion source.

$$XYZ + e^- \longrightarrow XYZ^+ + 2e- \qquad \text{(single charged)}$$

$$XYZ^{2+} + 3e- \qquad \text{(double charged)}$$

$$XY + Z^+ + 2e^- \qquad \text{(fragmentation)}$$

$$XY^+ + Z + 2e^- \qquad \text{(fragmentation)}$$

Where the first two represent ionization and the last two involve ionization and dissociation as well. $XYZ^+$ is the single charged ion; $XYZ^{2+}$ is the double charged ion; $XY^+$ and $Z^+$ are fragments of XYZ. So to interpret the mass spectrometry data correctly, we must be familiar with the multiple charged ions and fragmentation patterns of different species. Libraries of the fragmentation patterns of the most common species are available and are very helpful in qualitatively analysis. Besides the ionization and dissociation process, other unintended chemical effects such as wall effects and chemical reactions also exist in the ionizer. These effects will give rise to signals that can not be associated with the chemistry inside the system being monitored and need be taken into account in the data analysis. We are going to see more of these effects as we go along with this thesis and more discussion will be given at that time.

To interpret mass spectrometry quantitatively, we need first make clear one concept: sensitivity, which is defined by the following equation.

$$S_{ab} = I_{ab}/PP_a \qquad (2\text{-}22)$$

Where $S_{ab}$ is the instrument sensitivity (amps/torr) for mass b from specie a, $I_{ab}$ is the ion current of mass b from specie a, and $PP_a$ is the partial pressure of specie a. $S_{ab}$

consists of two components: $M_{ab}$ and $A_a$. $M_{ab}$ is the materials factor and $A_a$ is the analyzer factor. The general expression for $S_{ab}$ will be [xl]

$$S_{ab} = FF_{ab} \times XF_{ab} \times TF_b \times DF_{ab} \times G \times S_{N28} \qquad (2\text{-}23)$$

Where FFab is the fragmentation factor for mass b from substance a, XFab is the ionization probability of substance a relative to nitrogen, TFb is the transmission factor, the fraction of total ions at mass b which pass through the mass filter, DFab is the detection factor for mass b ions from substance a, relative to nitrogen at 28amu, G is the electron multiplier gain for nitrogen ions at 28 amu, and S is the sensitivity for nitrogen at 28amu. Most of the parameters are available from various tables. Knowing the sensitivity and the ion current, the partial pressure of the corresponding specie can be calculated easily based on equation 2-21. In order to have consistent and repeatable measurement, the sensitivity has to be kept constant with minimum variation. Sensitivity is considered as a criterion to evaluate the performance of the mass spectrometry. However, sensitivity change always exists, which requires careful calibration before serious quantitative measurement can be done. The way to calibrate mass spectrometry is to introduce a known amount of calibration gas of the desirable mass. The value of the measured ion current will then be used to calculate sensitivity according to equation 2-21. Equation 2-21 indicates that the ion current will increase proportionally with partial pressure of the sampled substance, while that is only true for a certain pressure region. Outside this region, non-linearity behavior will be observed. Usually the larger the region, the better the mass spectrometry, because non-linearity will cause difficulty in data analysis.

Nowadays, lots of efforts have been spent trying to produce mass spectrometry that can be operated under higher pressure so that complex and expensive pressure

reduction system can be avoided. One solution is miniature quadrupole mass spectrometry [xlii]. The sensor of miniature quadrupole mass spectrometry has dimensions comparable to the mean-free path of ions at high pressure and it can be operated at pressure as high as 10 mTorr. However, more work is necessary to improve its performance.

### *2.3: Fundamentals of IMC Run-to-run Control Algorithm.*

APC promises benefit through both fault management and course correction e.g. run-to-run control and real-time control. The importance of process control has been recognized gradually by semiconductor industry, as the industry goes to bigger wafer size and smaller device feature size. Part of our research is to accomplish the sensor-based film thickness process control in W-CVD process on a commercial cluster tool using run-to-run control algorithm.

Run-to-run control is a form of discrete process and machine control in which the product recipe with respect to a particular machine and machine process is modified from one wafer to the next as opposed to real-time control during the processing of a single wafer [xliii]. A great deal of groundbreaking work has been done on the run-to-run control algorithm within the context of semiconductor manufacturing [xliv, xlv, xlvi]. Most existing run-to-run controllers are developed using model based approaches. These models could be either linear models [xliv], [xlvii] or non-linear models [xlviii, xlix]. Our discussion here is restricted to linear models only, for usually the relationship between the process responses and control variables can be linearly approximated over the region of interest [xliv]. The parameters in the linear model are updated after every run based on the data from previous runs. The updated model is then used to determine the control recipe for

the next run. One way to update the model is Exponentially Weighted Moving Average (EWMA) [xlvi]. However in the presence of drift, such as temperature drift due to thermocouple degradation, EWMA (type I controller) will not be able to compensate the steady drift and results in an offset in the process outputs. Consequently EWMA is modified using the internal model control (IMC) structure offset (type II controller) to completely eliminate the offset. The general IMC structure for run-to-run control is illustrated by Figure 2.6, [xlvi] on the next page.

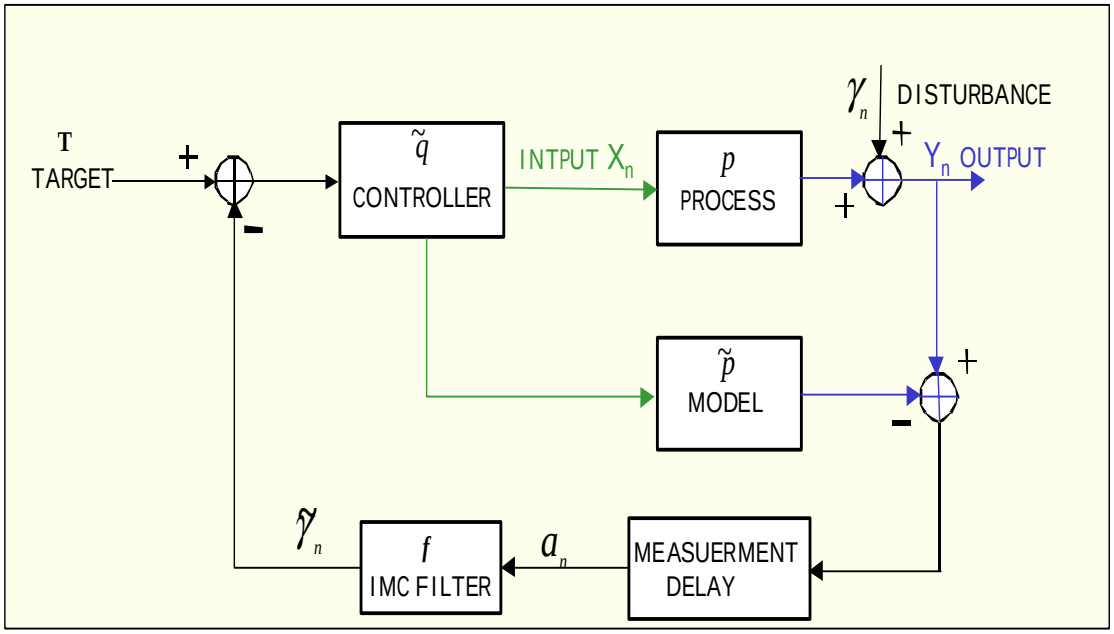


Figure 2.6: General IMC structures for run-to-run control. n denotes the run number.

Let the linear system and the model be represented by the following two equations respectively.

$$y_n = \gamma_n + \beta x_n \qquad (2\text{-}24)$$

$$\bar{y}_n = \bar{\gamma}_{n-1} + \tilde{\beta} x_n \qquad (2\text{-}25)$$

The IMC controller equivalent to pure EWMA controller will be

$$p = \beta;\ \tilde{p} = \tilde{\beta} \qquad (2\text{-}26)$$

$$q = \frac{1}{\tilde{\beta}} \qquad (2\text{-}27)$$

$$\tilde{\gamma}_n = \alpha \tilde{\gamma}_{n-1} + a_n(1-\alpha) \qquad (2\text{-}28)$$

Where $\alpha$ is the only tuning parameter for the controller. As opposed to EWMA, the modified filter for type II controller can be expressed as

$$\begin{aligned} \tilde{\gamma}_n &= \alpha \tilde{\gamma}_{n-1} + \tilde{a}_n(1-\alpha) \\ \tilde{a}_n &= \beta_0 a_n + \beta_1 a_{n-1} + \ldots + \beta_\eta a_{n-\eta} \end{aligned} \qquad (2\text{-}29)$$

$$\begin{aligned} \beta_k &= \frac{(\theta-1)\alpha-\theta}{(1-\alpha)} \cdot \frac{6k}{\eta(\eta+1)(2\eta+1)} \qquad k=1,\ldots,\eta \\ \beta_0 &= 1-\beta_1-\beta_2-\ldots-\beta_\eta \end{aligned} \qquad (2\text{-}30)$$

$\alpha$ and $\eta$ are the two tuning parameters. $\alpha$ lies between [-1,1], while $\eta$ is a positive integer. $\theta$ denotes the number of delayed runs or measurements. For details about the IMC controller design, refer to [1].

Despite the progress in run-to-run control algorithm, two factors prevent its wide application in semiconductor manufacturing. One is the lack of physically based model needed to drive the controller; the other is the lack of generic framework to facilitate the implementation of the control algorithm. For the first barrier, Stefani et al. used

empirical-based response surface model (RSM), which adequately comprehends the process behavior as a substitution to the physically based model and realized process control to compensate for process shifts [li]. As to the second obstacle, Moyne et al. at University of Michigan demonstrate a well-established control framework which is a multi-level control system including real-time equipment control and process control as well as discrete (run-to-run) control. Hopefully with persistent efforts, these two barriers will eventually be overcome and the practice of run-to-run process control will be widely accepted in semiconductor manufacturing.

# 3. Experimental Procedures.

Our research focuses on the real-time *in-situ* chemical sensing sensor based thin film thickness metrology, and process control in W-CVD process using mass spectrometry. The tool used for the W deposition is Ulvac-ERA 1000. Two mass spectrometry sampling systems of different design and location have been constructed: (i) downstream sampling system implemented on the exhaust line of the CVD system; (ii) direct sampling system attached to the reactor chamber. Tool state signals from Ulvac-ERA 1000, such as temperature, pressure, and flow rate, were captured synchronously with mass spectrometry signal. A data acquisition system was built to enable tool state data collection using data acquisition board from Computer Board□ running on LabView□ platform. The W deposition was characterized by the mass spectrometry and optimized for process and metrology development. Signals of the reaction product generation and reactant depletion have been detected and used to provide a measurement of the W film deposited.

## *3.1: Ulvac ERA-1000 W-CVD Cluster Tool*

### 3.1.1: Overview of ERA-1000

Ulvac-ERA 1000 W-CVD cluster tool is a lamp heated, cold wall, single wafer system. It is designed for selective W-CVD process from $SiH_4/WF_6$ mixture under an operation pressure constraint of 1 Torr. As illustrated in Figure 3.1, Ulvac-ERA 1000 consists of two identical process chambers, a load lock chamber and a buffer chamber for wafer transfer. For each reactor, there are two sets of pumps: (i)

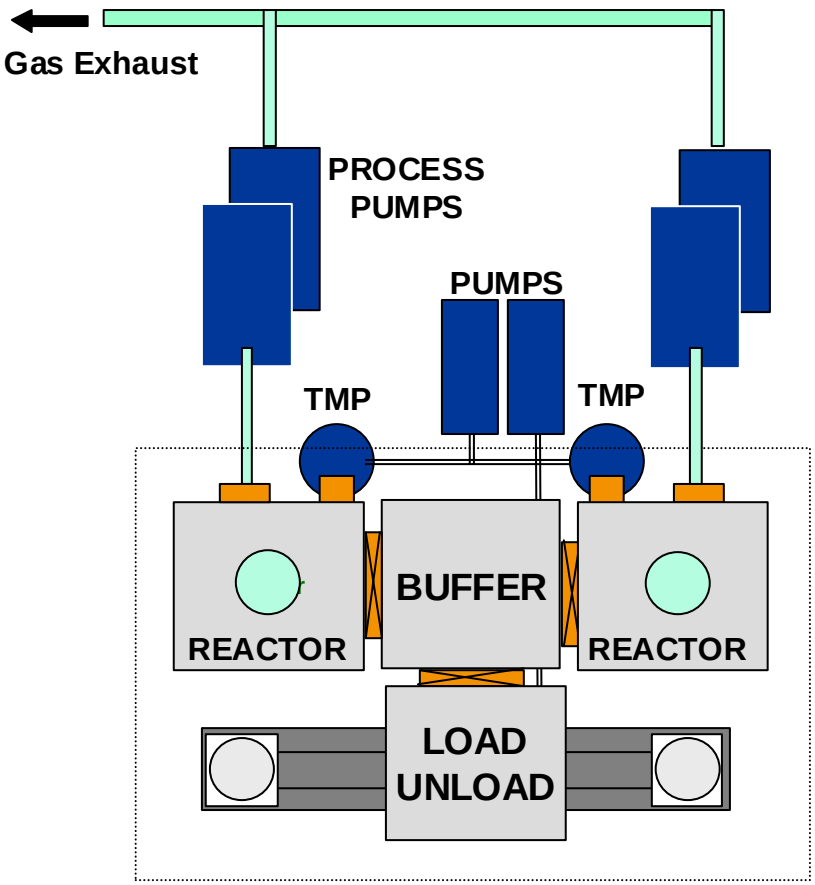


Figure 3.1: Top view of Ulvac-ERA 1000 W-CVD cluster tool.

process pumps, a rotary pump and a Roots blower pump for processing the wafers; (ii) a turbo molecule pump and a mechanical backing up pump for maintaining the vacuum. In the standby mode, the turbo pump is able to keep the chamber under high vacuum of about $10^{-7}$ torr to minimize the contamination detrimental to both deposition and chemical sensing. Ulvac-ERA 1000 is capable of processing wafers up to 8" in diameter, allowing for high speed filling of high aspect ratio (3:1) contact and via holes [[lii]]. With good control of the process conditions, selectivity and low contact resistance can be achieved with a high throughput of about 15-18 wafers/hour for deposition of 8000A film by $SiH_4$ reduction process. Special considerations have been given in reactor

design to control the particle generation during deposition, which is a common problem in W-CVD process especially for selective CVD. Although the reactor is water-cooled to reduce unwanted deposition on the wall, accumulation of W and W oxide were still observed after running for a long time. Fortunately the system includes plasma self cleaning capability. By running the appropriate recipe, it can automatically plasma clean and condition the chamber. Three different plasma modes are available allowing the operator to clean any particular location in the reactor.

### 3.1.2: Process chamber configuration

Figure 3.2 [[liii]] depicts the lamp-heated, cold wall, single wafer reactor, with an octagonal shape to avoid turbulence at the corners. Gas flow in a reactor is always critical to a CVD system. The ERA-1000 is designed to deliver a controlled gas flow, providing superior repeatability and uniformity to the deposition process. During the process, $WF_6$, $SiH_4$, and the carrier gas are introduced through a two dimensional nozzle installed on one side of the reactor to form a sheet-like laminar gas flow over the wafer, while $H_2$ enters the chamber through the showerhead on the top. The advantage of this configuration lies in that $H_2$ flow helps keep the showerhead temperature low so the deposition on the showerhead is minimized. Deposition on the showerhead will not only cause particle generation but also block out the radiant heat from infrared heating lamp mounted above the chamber. Our experience tells us that once the deposition on the showerhead starts, selectivity loss will deteriorate very quickly and degrade deposition as well as chemical sensing.

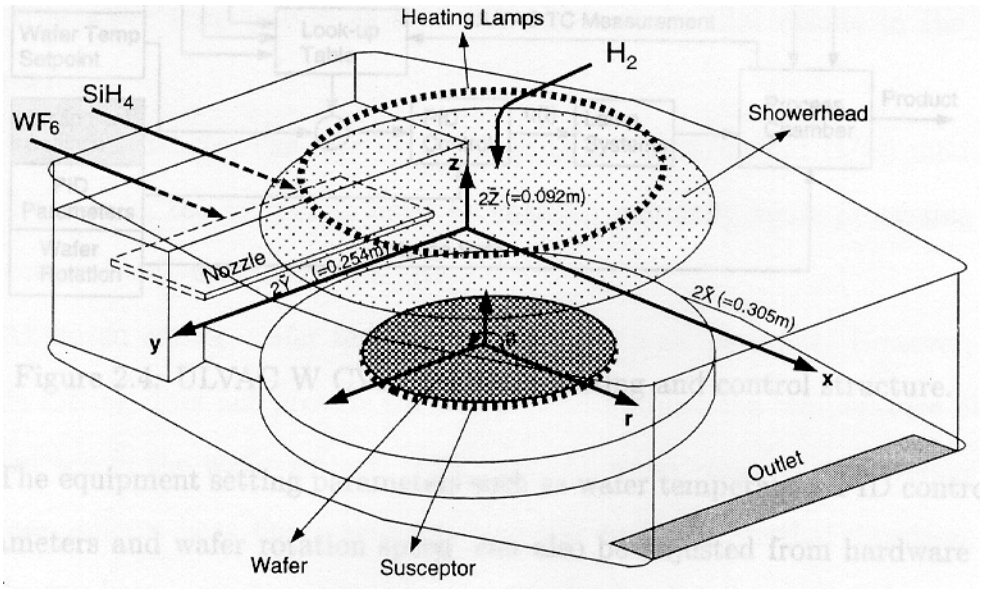


Figure 3.2: Schematic of Ulvac-ERA 1000 W-CVD reactor [liii].

### 3.1.3: Processing procedure.

Equipped with a powerful remote control system, Ulvac-ERA 1000 has full capability of automatic wafer transfer and process execution. Manual operation is also available and offers much more flexibility in tool maintenance. Prior to deposition, the process recipe is edited first and saved in the controller on the touch screen. Values of all process parameters such as pressure, temperature, and flow rates are given for each step of the recipe. Illustrated below is a typical multi-step recipe used in our research (Table 3.1).

Table 3.1: A typical multi-step recipe for W deposition.

| Recipe Name: | Step # | Time (sec.) | Temp. | Pres. (mtorr) | Bypass[1] | $WF_6$ (sccm) | $H_2$ (sccm) |
|---|---|---|---|---|---|---|---|
| 62399A | 1 | 300 | 0 | 500 | 0 | 0 | 2 |
| | 2 | 30 | 0 | 500 | 1 | 10 | 40 |
| | 3 | 360 | 0 | 500 | 0 | 10 | 40 |
| | 4 | 180 | 550 | 500 | 0 | 0 | 40 |
| | 5 | 120 | 500 | 500 | 1 | 10 | 40 |
| | 6 | 360 | 500 | 500 | 0 | 10 | 40 |
| | 7 | 180 | 0 | 500 | 0 | 10 | 40 |

Each recipe can have up to 12 steps and as many as 100 different recipes can be stored in the system. After recipe editing, the controller can execute the process automatically. All the information in the recipe will be transferred to the corresponding controllers such as throttle valve pressure controller, thermo-couple temperature controller, mass flow controller, and programmable logic controller (PLC) of the Ulvac-

ERA 1000. The process parameter readings from these controllers will be displayed on the screen throughout the entire process. The main controller also offers output signal ports where data acquisition can be accomplished easily with a data acquisition system built on data acquisition board[2] by Computer Board¤. (More details are presented in the section 3.3 regarding data acquisition.) After the process is done, the wafer will be transferred out and unloaded automatically. The chamber is then set back to standby mode, available for the next wafer processing.

## *3.2: Implementation of Mass Spectrometry for Real-time Sensing in W-CVD Process on Ulvac ERA-1000 W-CVD Cluster Tool.*

### 3.2.1: Downstream Sampling System.

Initially a downstream sampling system was constructed and installed on the exhaust line of Ulvac-ERA 1000 outside the cleanroom (see Figure 3.3). The main advantage of this configuration is that the sampling system requires no major modification to the existing process tool and saves the valuable space in the clean room. It is isolated from the Ulvac-ERA 1000 by a normally closed gate valve, which will be open during process for sampling and has no disturbance to the upstream reaction in the chamber. This configuration was successful for the polysilicon CVD process, however it turns out to be problematic for W-CVD process. The reason comes

[1] Value 1 means the $WF_6$ is sent into the bypass line.
[2] Valve state data is recorded from the PLC.

from the presence of the extremely reactive precursors and product, i.e. HF and $WF_6$. They readily react with impurities existing in the reactor, such as water, even at the

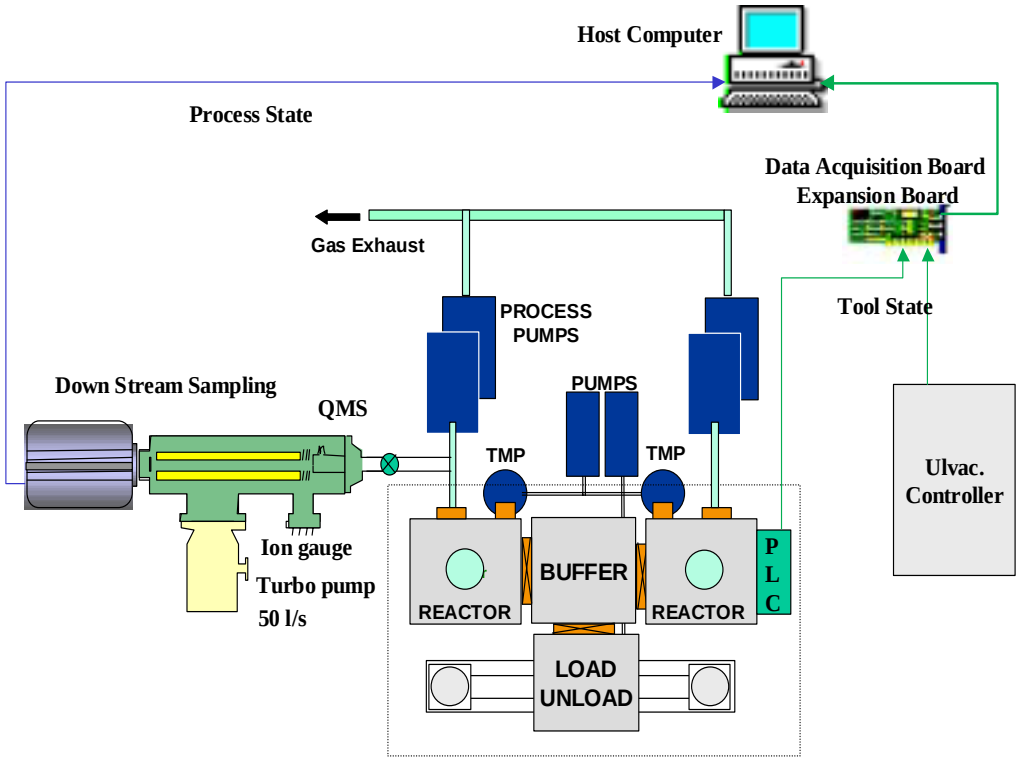


Figure 3.3: Configuration of the mass spectrometry downstream sampling system.

room temperature (see equation 3.1 below) [liv] and condense on the huge surface of the exhaust line. Although this imposes no problem on the process itself, it does make process analysis and sensor-based wafer state metrology difficult. What the down stream sensor sees is a combination of wall effects and process reaction on the wafer, which are not easy to distinguish from each other. Large wall surface also implies that it will take a long time for the wall to reach equilibrium. Baking the exhaust line may help, however such a long exhaust line made any effort to bake quite impractical.

$$WF_6 + H_2O \longleftrightarrow WOF_4 + WO_x + HF \qquad (3\text{-}1)$$

### 3:2.2: Direct Sampling System.

Due to the concerns mentioned above, the initial down stream sampling system was abandoned and a new sampling system was set up for direct sampling from the reactor chamber. This way, the exhaust line is bypassed and most of the wall surface is eliminated (see Figure 3.4). A rough estimation reveals that when the process pressure in the reactor is $5x10^{-1}$Torr, the pressures in the ion source region and the mass spectrometry manifold will be $1.65x10^{-4}$ Torr and $1.6x10^{-6}$ Torr respectively. This is in agreement with our observation. (See Appendix 1 for the mathematical derivation.) As seen in Figure 3.4, in order to improve the dynamic behavior of the sampling system, the inter-stage of the turbo drag pump is used to draw a small amount of gas actively from the reactor side. With this feature, a short response time of several seconds (the response time of the mass spectrometry signal to the chemistry change in the reactor) has been recorded. For processes longer than two minutes, the 3-4 seconds delay usually is acceptable and can also be factored in while analyzing data. To have further control of the already greatly reduced wall effect, the entire sampling system including the mass

spectrometry manifold and the line between the manifold and the reactor are baked at $70^0$C. Such a warm wall at around $70^0$C is considered to be optimal for our configuration, because baking at lower temperature will not be enough to prevent condensation on the wall, while too high a wall temperature may promote chemical reaction and deposition.

Figure 3.4: Configuration of the mass spectrometry direct sampling system.

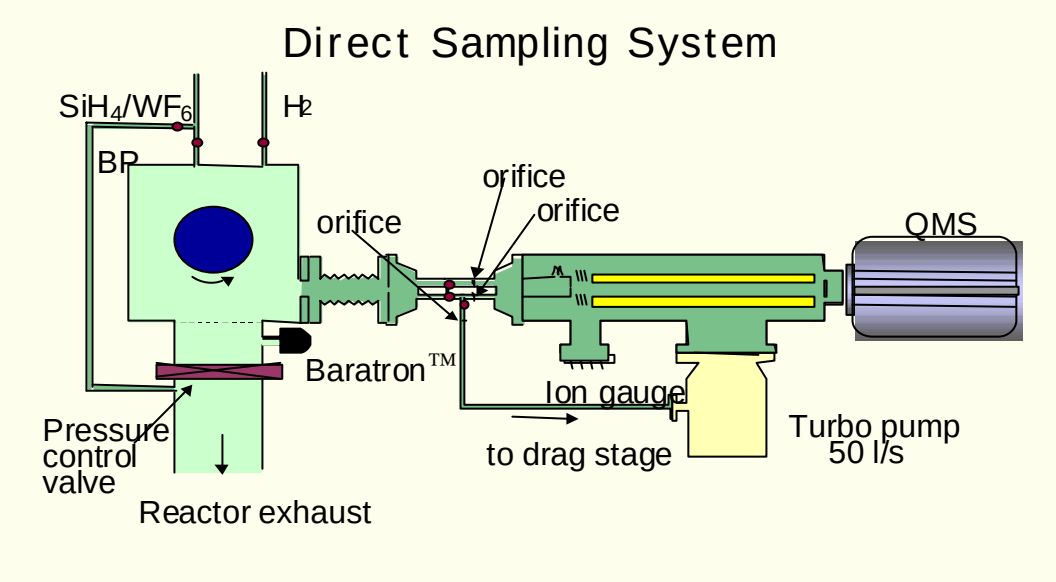


The mass spectrometers applied in our research are H300M (Faraday cup mode) for $H_2$ reduction process and H200M (Electron multiplier mode at 1KV acceleration voltage) for $SiH_4$ reduction process. RS232 communication supports the communication between the host computer and Transpector. The software used to operate the mass spectrometry is TransepctView□, which is built on LabView□ platform and provides two different modes of data acquisition: (i) Spectrum scanning mode, (ii) Histogram scanning mode. For histogram scanning mode, time evolution of up to 10 user-defined species up to 300amu for H300M or 200amu for H200M can be monitored.

### *3.3: Data Acquisition and Sensor Integration*

Sensor-based process control, defined as the application of APC with all or most of the data supplied by *in-situ* sensors, is the core of metrology integration. To accommodate sensor-based process control, more and more sensors are incorporated on the process tool in an evolutionary process. These sensors (add-on or original) provide real-time information regarding the process and tool status, which is invaluable for process analysis, equipment diagnosis, and process control. In order for sensors to support process control efficiently, several requirements have to be met.

1. Sensor can be installed on the process tool with a small footprint and requires no major modification to the tool.
2. All sensor data have a time stamp from a common clock to allow merging wafer and tool data for data comparison.

In our research, Ulvac-ERA 1000 equipment state signals were captured synchronously with mass spectrometry signal. Table 3.2 includes all sensor signals collected and Figure 3.5 shows some of the integrated sensor signals revealing subtle but important dynamics.

Table 3.2: Integrated sensor data collection.

| Signals | Pressure | Temperature | Mass flow controller 1 ($WF_6$) | Mass flow controller 2 (Ar) | Mass flow controller 3 ($H_2$) |
|---|---|---|---|---|---|
| Signal range | 1-1000 mtorr | 0-800$^0$C | 0-50 sccm | 0-200 sccm | 0-2000 sccm |
| Voltage range | 0-10 volts | 0-10 volts | 0-10 volts | 0-10 volts | 0-10 volts |

~

| Signals | Mass flow controller 4 ($SF_6$) | Mass flow controller 5 ($N_2$) | Mass flow controller 6 ($SiH_4$) | Valves 1, 11,41 | Butterfly valve position |
|---|---|---|---|---|---|
| Signal range | 0-50 sccm | 0-200 sccm | 0-20 sccm | Open / Close | (0-100%) |
| Voltage range | 0-10 volts | 0-10 volts | 0-10 volts | 0 / 24 volts | 0-10 volts |

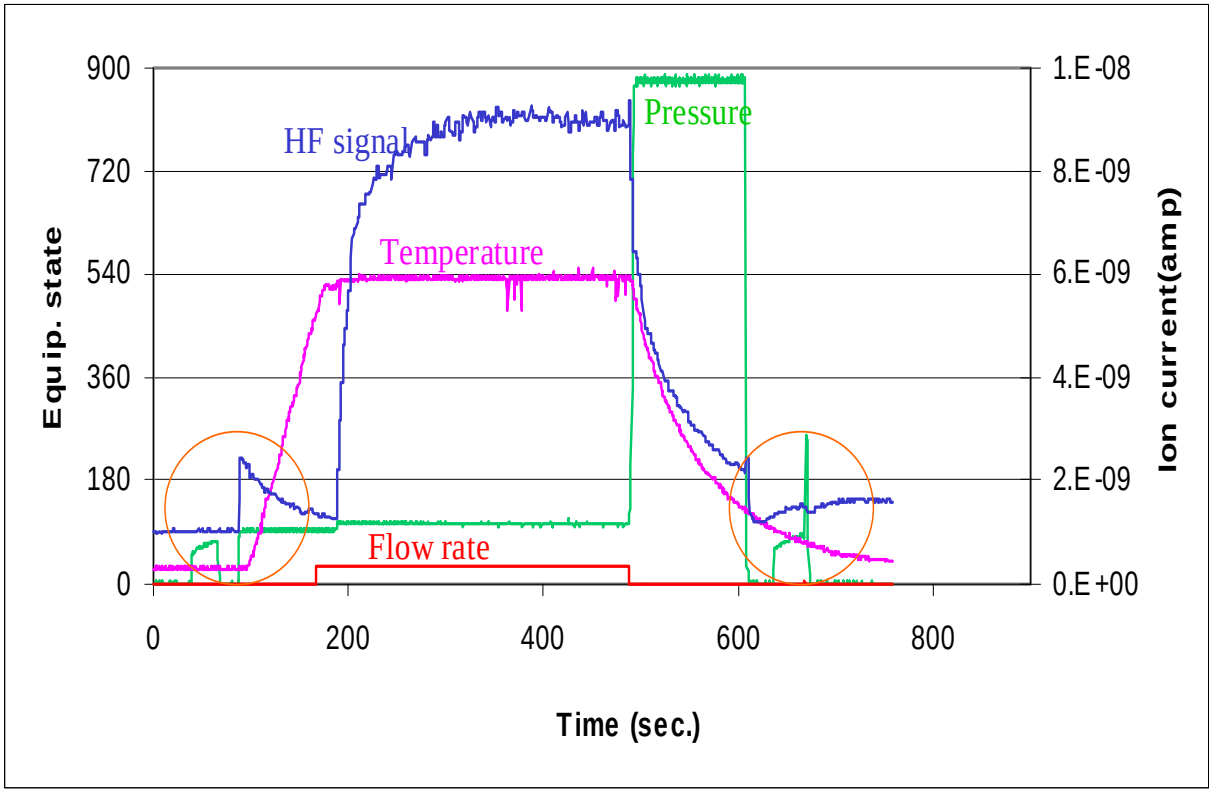


Figure 3.5: Integrated sensor signals.

### 3.3.1 Implementation of Sensor Integration

Data acquisition board DAS 08H from Computer Board® was used for data acquisition. It is featured with 12 analog input channels and 2 digital output channels and is capable of measuring signals of up to 10 volts. To expand the channel number to accommodate all the necessary tool state signals, expansion board EXP 32 from Computer Board® was deployed and the total number of available channels reaches 32, consisting of 2 bands each with 16 channels. Input of EXP 32 is hardwired to the signal outputs located at the rear rack of the main controller for temperature, pressure, and mass flow rates measurement, while valve status is measured from the PLC. (See Figure 3.3 in previous section 3.2.1) Output of EXP 32 is plugged into DAS 08H, which is installed in the expansion chassis of the host computer. Both DAS 08H and EXP 32 are running on Labview® platform, enabling incorporation of the LabView® application that operates DAS 08H and EXP 32 with TranspectorView®. So after starting, TranspectorView® collects data from data acquisition board (tool state signals) and mass spectrometry (mass spectrometry signal) synchronously (See Figure 3.6). Both sets of data share the same clock time and sampling rate. Sampling rate of 2 Hz can be achieved. All data is saved in asci format for future analysis using applications like Origin and Excel. To get more information about the configuration of DAS 08H and EXP 32, refer to manuals [lv, lvi].

### 3.3.2 Challenges in Implementation.

The complexity of TranspecterView® that caused the difficulty in integrating it with the LabView® applications for data acquisition boards without sacrificing the integrity of the program accounts for the major challenge encountered in the sensor integration. The final integrated program must support the synchronous capture of tool

state data and mass spectrometry data. Furthermore, in order to facilitate sensor based process control, special functionality such as integrating mass spectrometry data of particular species over time had been added to TranspecterView□ too. This is not trivial by any means, especially considering the elusive nature of graphic language such as LabView□ with which TranspectorView□ is programmed.

Another challenge that we experienced is that the signals we collected were of different types (single-ended, differential signal, and float differential signal) and ranges (+- 5 volts and +- 24 volts). They need be distinguished and treated differently. For example, single-ended signal can be measured easily, while cautions must be taken to measure floating differential signals, i.e. to prevent ground loop.

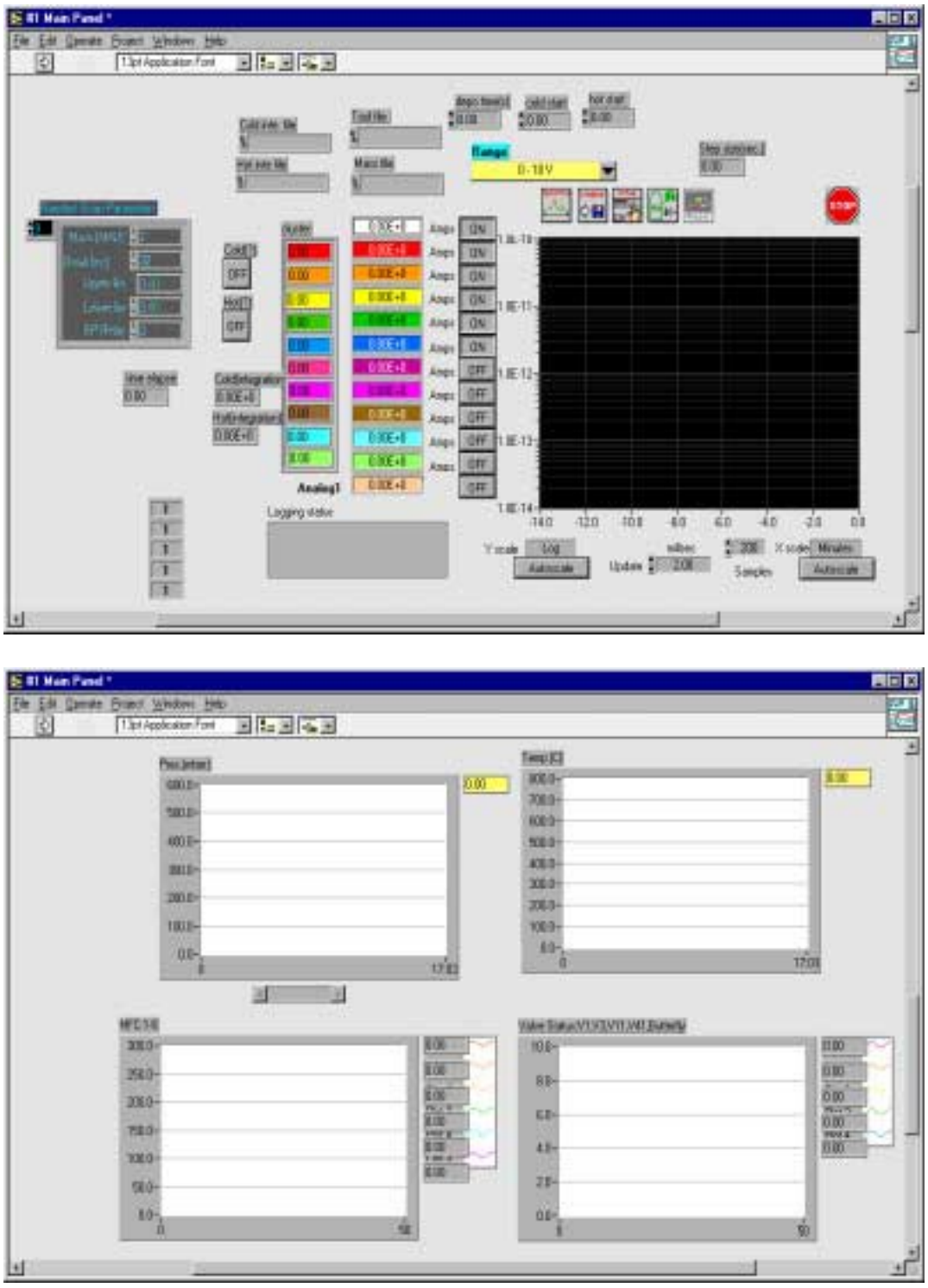

Figure 3.6: Snapshots of the graphic interface for sensor integration.

### *3.4: W-CVD Process on Ulvac-ERA 1000 W-CVD Cluster Tool.*

Our $WF_6$-based W-CVD processes utilize either $H_2$ or $SiH_4$ as the reducing agents. We started with $H_2$ reduction experiment because we were not cleared for the safety issues associated with $SiH_4$ in the beginning. W thin films of various thickness were grown on bare 4" Si wafer. Since the main goal of this research is to develop sensor-based thin film thickness metrology and process control using mass spectrometry, contact/via filling properties were not a major concern at this stage. Non-patterned bare Si wafer serves this purpose very well. All wafers used have undergone 10% HF solution dipping, DI water rinsing, and $N_2$ drying to remove native $SiO_2$. In order to prevent re-oxidation, the wafer was loaded into the immediately after the cleaning procedure. It has been founded that the dipping time is critical to assuring oxide free wafer surface. Any remaining $SiO_2$ will retard the nucleation of W film and results in non-uniform W film. Mass spectrometry detects the W growth on clean and unclean Si wafer at different rates, which are dependent on the surface conditions. This is used later for fault detection.

As explained before, $WF_6$ is extremely reactive and readily reacts with impurities on the reactor wall. The reaction contributes to the reactant depletion and product generation, just as does the process reaction on the Si wafer surface. Another issue that need be considered is $WF_6$ and HF condensation on the walls even at elevated temperature. To control the influence of wall effects on chemical sensing, a conditioning cycle of 30-60 minutes was always implemented before processing. In $H_2$ reduction experiment, $H_2$ and $WF_6$ at 4:1 ratio were introduced into the unheated reactor to allow the wall to reach equilibrium. In the beginning the ratio of $WF_3O^+$ (fragment of product from reaction between $WF_6$ and $H_2O$ or $O_2$) mass spectrometry signal to $WF_5^+$ signal is

5:1. After conditioning for a certain period of time (usually half an hour to an hour) the ratio can be reversed to 1:5, which is a sign that oxygen/water impurities have been substantially reduced. In the $SiH_4$ reduction process, $SiH_4$ diluted in Ar was used to condition the wall. $SiH_4$ is expected to react with condensed $WF_6$ to leave behind a clean wall surface.

After deposition the film weight was measured off line by STYLUS□ microbalance with a resolution of $10^{-4}$ g, which corresponds to a thin W layer of 6.6 Å on 4" wafer. Once the film weight is known, the average thickness can be easily calculated from the known wafer area (4" wafer) and W density (19.3g/$cm^3$). This proves to be a much faster and accurate way to determine film thickness compared to lithograph patterning and profilometry.

### 3.4.1: W-CVD Process by $H_2$ Reduction

#### 3.4.1.1 Process Development.

In semiconductor manufacturing, blanket W-CVD is the process of choice as opposed to selective W-CVD. The deposition is usually carried out at 40-100 torr by $H_2$ reduction of $WF_6$ followed by CMP process to remove extra W deposited on the insulator. Unfortunately Ulvac-ERA 1000 is designed for selective W-CVD from a mixture of $SiH_4/WF_6$ under 1 Torr, too high an operation pressure for selective W-CVD process causes selectivity loss at high pressure. Within this pressure limitation, the $H_2$ reduction process involves very low utilization efficiency of $WF_6$, which poses a variety of challenges both fundamental and practical to chemical sensing.

In order to improve the reactant conversion rate under the pressure constraints, we first tried deposition at higher deposition temperature. However, selectivity loss at high

temperature prevented us going too far in this direction. It was observed that at high temperature[3] (>525$^0$C) or pressure (>0.5 Torr), W deposition on the quartz showerhead and susceptor would start shortly after several runs. Therefore an optimal temperature of 500$^0$C was selected along with operating pressure of 0.5 Torr for most of the $H_2$ reduction experiments. Simulation results based on the Hsieh's model indicate that within this process window the reaction is kinetics-limited. Reducing the total flow rate of the reactants at constant pressure will have no obvious effect on the deposition rate and thus the conversion rates of the reactants will be enhanced. In practice, the flow rates of $H_2$ and $WF_6$ were cut down from initially 200 and 50 sccm to 40 and 10 sccm. This improves conversion rate of $WF_6$ to around 3-4%, giving deposition rate of about 216Å/min calculated according to the W film weight and deposition rate. See Table 3.3.

[3] The temperature here is the nominal temperature which is about 150-200$^0$C lower than the true wafer temperature [liii]

Table 3.3: Deposition rate and conversion rate of $WF_6$ in W-CVD process from $H_2$(40sccm)/$WF_6$(10sccm) mixture at $500^0$C and 0.5 Torr.

| Wafer # | 2 | 3 | 4 | 5 | 6 | 7 | Average |
|---|---|---|---|---|---|---|---|
| Deposition rate(Å/min.) | 197 | 229 | 224 | 219 | 215 | 209 | 216 |
| Conversion rate | 3.63% | 4.22% | 4.13% | 4.03% | 3.96% | 3.86% | 3.97% |

Equations 2.1,2.2, and 2.3 as repeated below show the chemistry of the main reactions involved in the W-CVD process by $H_2$ reduction of $WF_6$.

$2WF_6 + 3Si \longleftrightarrow 2W + 3SiF_4$ (g) (Nucleation)

$WF_6 + 3Si \longleftrightarrow W + 3SiF_2$ (g) (Nucleation)

$WF_6 + 3H_2 \longleftrightarrow W + 6HF$(g) (Sustained deposition)

The Si reduction reaction always happens and is responsible for the W seed layer deposition during the nucleation stage. In the presence of $H_2$, one more reaction is observed. See equation 3-2.

$Si + WF_6 + H_2 \longleftrightarrow W + 2SiHF_3$(g) (3-2)

After Si wafer is covered with a W seed layer, the Si reduction process is retarded and W film growth will be sustained by $H_2$ reduction. Table 3.4 below lists the major species observed in the mass spectrometry. The mass spec. fragmentation patterns

of these species need be monitored to characterize the process and develop film thickness metrology.

Table 3.4: The major species existing in $H_2$ reduction W-CVD process on pure Si wafer surface and their corresponding fragmentation pattern.

| Species | Fragment Pattern (amu) | Source | Category |
|---|---|---|---|
| $SiF_4$ | $SiF_3^+$ (85amu) | Si reduction | Product generation |
| $SiF_3H$ | $SiF_2H^+$ (67amu) | Si reduction | Product generation |
| HF | $HF^+$ (20amu) | $H_2$ reduction | Product generation |
| $WF_6$ | $WF_5^+$(277,278,279,281 amu)[4] | H2&Si reduction | Reactant depletion |
| $H_2$ | $H_2^+$ (2amu) | $H_2$ reduction | Reactant depletion |

Figure 3.7 illustrates the time evolution of $SiF_4$, $SiF_3H$, and HF generated in W-CVD process from $H_2/WF_6$ mixture. As explained before, Si reduction is a self-limiting process which dominate the nucleation stage. $SiF_3$ and $SiF_2H$ signals appears as sharp, narrow peaks. Both signals rise up dramatically as soon as Si wafer is exposed to $WF_6$ and then drop down quickly after the wafer is covered with a W seed layer. As opposed to $SiF_3$ and $SiF_2H$, HF signal lasts through the entire processing cycle.

The HF product signal takes a much longer time to return back to the background level after $WF_6$ flow is terminated at the end of the process.. Three mechanisms have been proposed to explain the slow decay of the HF signal after process ends.

[4] 4 peaks represent 4 W isotopes (182,183,184,186). 184 is the most abundant one.

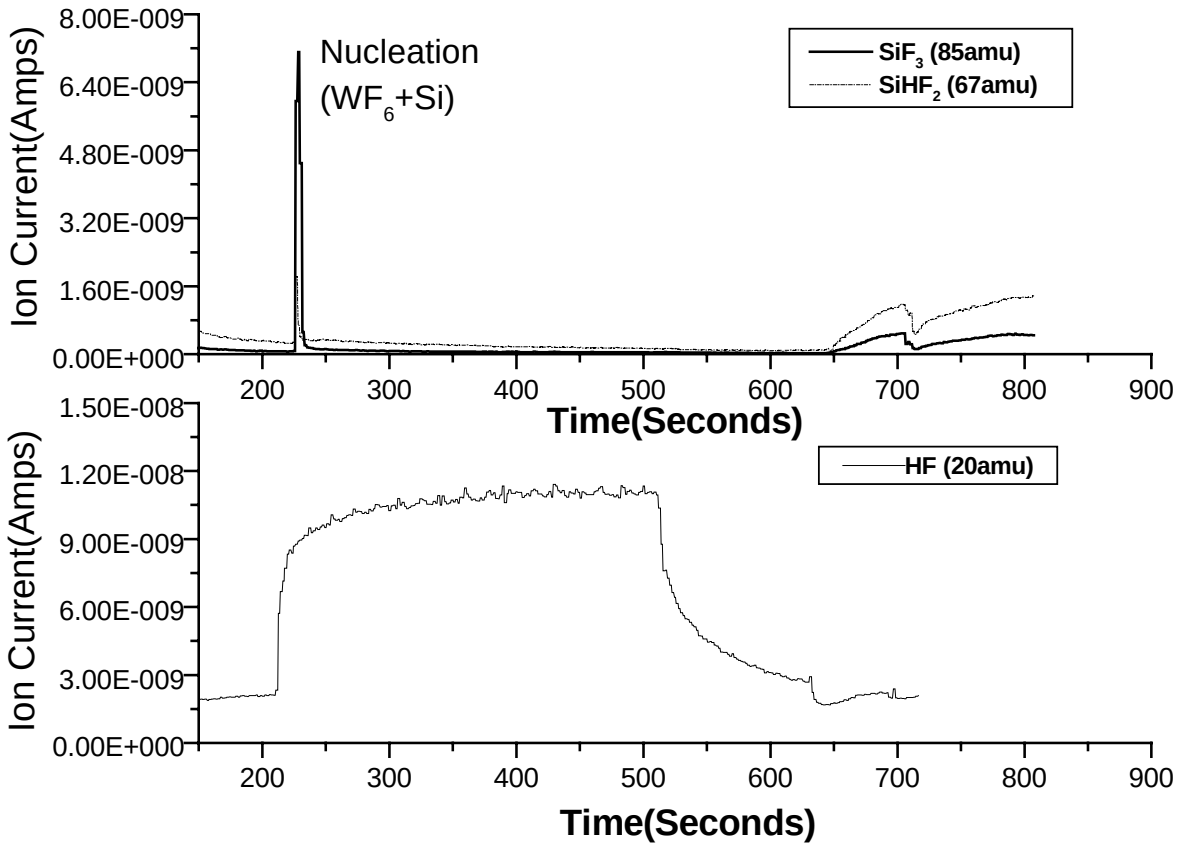


Figure 3.7: Mass spectrometry signals for product generation in W-CVD process from $H_2/WF_6$ mixture.

1. The $H_2$ flow which is maintained during wafer cooling reacts with $WF_6$ on the reactor wall and pump line to generate HF.

2. Because of the hot filament in the mass spec. ion source, the temperature can reach several hundred degrees. Thermal reaction of $H_2$ with $WF_6$ desorbing on these walls is likely. A layer of gray/blue deposition (presumably $WO_x$) was observed on the ceramic parts of the ion source. In fact this deposition sometimes caused emission failure in the mass spectrometry due to leakage current.

3. Ion-molecule reaction in the mass spec. ion source can occur between $H_2$ and $F^+$ to generate HF.

Ion-molecule reaction involves the reaction of ions as created in the mass spec. with neutral molecules leading to the detection of ion currents, which could not appear, by direct ionization of any species known to be present. Examples are ions of mass to charge ratio of 3 and 19, which could only be explained by ion molecule reactions shown below in equations 3-3 and 3-4 [lvii].

$$H_2^+ + H_2 \longleftrightarrow H_3^+ + H \qquad (3\text{-}3)$$

$$H_2O^+ + H_2O \longleftrightarrow H_3O^+ + OH \qquad (3\text{-}4)$$

or $$H_2^+ + H_2O \longleftrightarrow H_3O^+ + H$$

One postulated ion molecule reaction path for HF generation is given in equation 3-5, though other reaction paths are possible.

$$F^+ + H_2 \longleftrightarrow HF^+ + H \qquad (3\text{-}5)$$

Experiments were set up to study HF generation in the ion source. To reduce the interference of wall reaction (path one above), $H_2$ and $WF_6$ were delivered into the reactor separately with $H_2$ through the calibration system[5] and $WF_6$ through the reactor with no lamp heating. This way $H_2$ and $WF_6$ only meet in the ion source and the considerable HF observed must result from reactions in the mass spec. ion source. From the experiment results, a response surface model of HF signal as a function of $H_2$ and $WF_6$ partial pressure can be obtained using Echip▫, which may be used to establish an empirical model based simulator for chemical reaction in the ion source.

### 3.4.1.2 Film Characterization.

Auger analysis results of the W film obtained from the $H_2$ reduction process reveal only minimal amount of fluorine (Figure 3.8). At the Si/W interface, $W_xSi_y$ was detected with no surprise. That shall result from the Si reduction reaction during the initial nucleation stage of the process. RBS results also indicate incorporation of Si in the W film but with limited amount of no more than 10-15%. For the W film deposited in $H_2$ reduction process, the three layers are: (i) 1500Å/W-95%,Si-5%; (ii)200Å/W-88%, Si-12%; (iii) Bulk/Si-99%, W-1%. More analysis techniques are needed to characterize this $W_xSi_y$ layer thoroughly.

Atomic Force Microscope demonstrate that the roughness of the W film is about 18 nm, which is quite large but not surprising considering the morphology is always a problem for W film deposition [xix].

[5] For more details about calibration system, see chapter 5

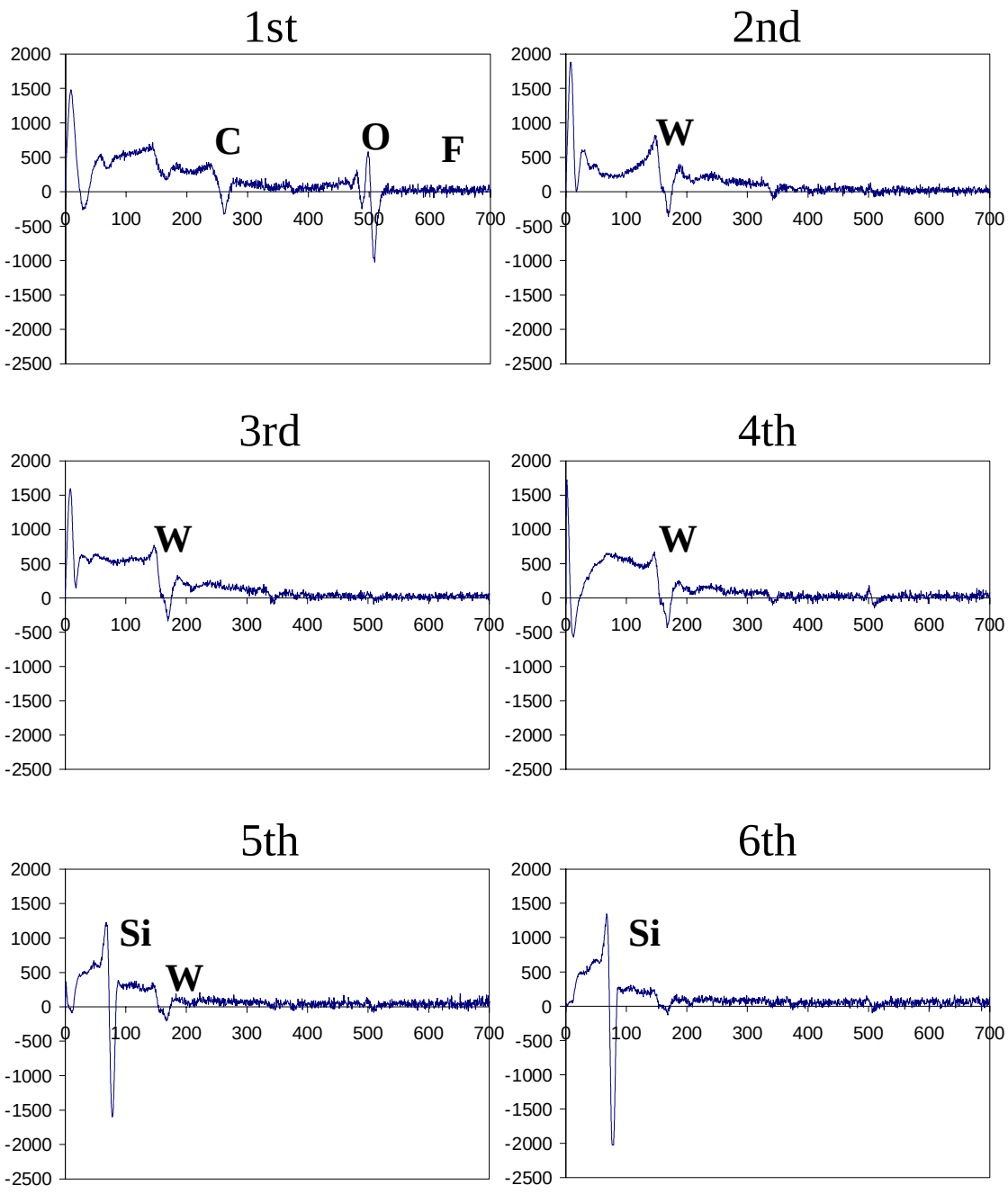


Figure 3.8: Auger analysis result of W film prepared by $H_2$ reduction process.

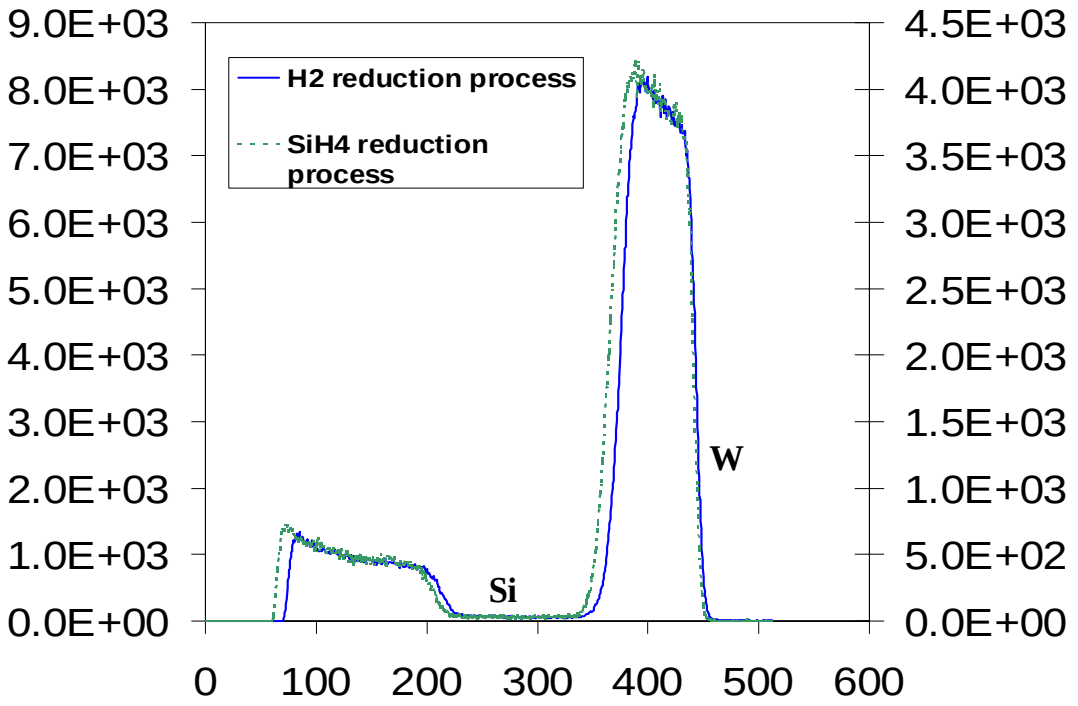


Figure 3.9: RBS results of the W films by both $H_2$ reduction process and $SiH_4$ reduction process.

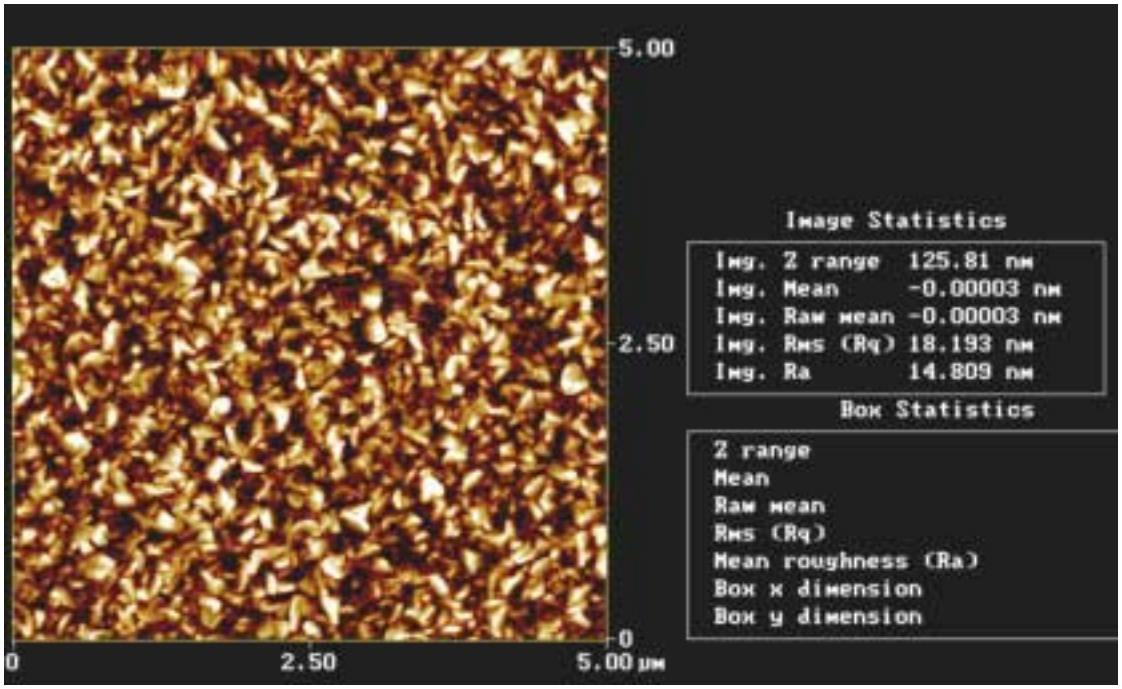


Figure 3.10: AFM image of the W film deposited by $H_2$ reduction process.

### 3.4.2: W-CVD Process by $SiH_4$ Reduction

#### 3.4.2.1 Process Development.

In semiconductor manufacturing, tungsten fill consists of two steps. The first, as seed layer deposition, uses $SiH_4$ to reduce $WF_6$ with Ar as the diluting gas. $SiH_4$ in the process helps to prevent fluorine attack of the oxide and substrate Si in areas where they may not be fully protected with a barrier layer, e.g. TiN. Compared with $H_2$, $SiH_4$ is a much more effective reducing agent, so that the $SiH_4$ reduction process usually is carried out at relatively low temperature and pressure while still keeping sufficient growth rate and conversion rate. In most of our $SiH_4$ experiments, deposition temperature and

pressure were fixed at $250^0C$[6] and 0.1 Torr. The flow rates of $SiH_4$ and $WF_6$ were 8 sccm and 10 sccm respectively, diluted in 180 sccm Ar. The ratio of $SiH_4/WF_6$ is intentionally kept below 1, the threshold ratio, above which high resistivity β phase W appears.

Equations 2-8 and 2-9 shown below represent the main reactions happening in the $SiH_4$ reduction process, which is rapid enough that it dominates over Si reduction.

$$3SiH_4 + 2WF_6 \longleftrightarrow 2W + 3SiF_4 + 6H_2 \qquad \text{(path one)}$$

$$2SiH_4 + WF_6 \longleftrightarrow W + 2SiHF_3 + 3H_2 \qquad \text{(path two)}$$

Table 3.5 below lists the major species existing in the $SiH_4$ reduction process and the fragment pattern of these species that need be monitored to characterize the process and develop film thickness metrology. Figure 3.11 depicts the mass spectrometry signals for the major species in $SiH_4$ process. Note that all the signals showed abrupt change around 45 seconds after the deposition cycle started. Product and reactants signals show complementary behavior implying a sudden increase of the process reaction. Two possible reasons have been considered. First because of the lattice difference between W and Si, W-CVD process on bare Si wafer using $SiH_4$ reduction of $WF_6$ requires an incubation time for nucleation. Similar behavior has already been observed in other metal film CVD processes. The second possibility is that compared with Si, W has a much lower emissivity so that the radiative heat loss of the wafer will be reduced after the bare Si wafer is covered with a W seed layer. This suggests that the initial stages of the deposition process, during which the bare silicon is covered by W, involve a temperature increase of up to $50^0C$ and that temperature increase caused the enhancement of the

[6] Refer to nominal temperature, which may be about $100^0C$ lower than true wafer temperature [liii].

chemical reaction on the wafer surface. However the low activation energy of $SiH_4$ reduction process makes this possibility unlikely.

Table 3.5: The major species existing in $SiH_4$ reduction W-CVD process on pure Si wafer surface and their corresponding fragmentation pattern.

| Species | Fragment Pattern (amu) | Source | Category |
|---|---|---|---|
| $SiF_4$ | $SiF_3^+$ (85amu) | $SiH_4$ reduction | Product generation |
| $SiF_3H$ | $SiF_2H^+$ (67amu) | $SiH_4$ reduction | Product generation |
| $H_2$ | $H_2^+$ (2amu) | $SiH_4$ reduction | Product generation |
| $WF_6$ | $WF_5^+$(277,278,279,281 amu) | $SiH_4$ reduction | Reactant depletion |
| $SiH_4$ | $SiH_2^+$ (30amu) | $SiH_4$ reduction | Reactant depletion |

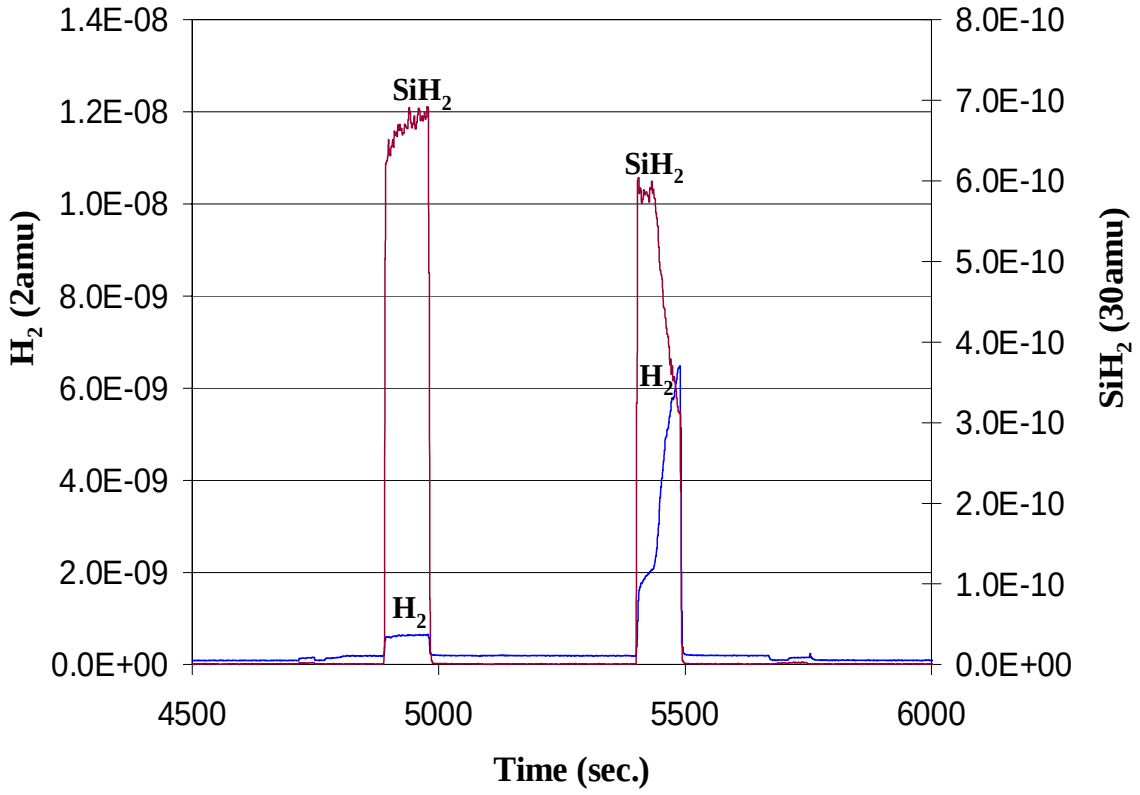


Figure 3.11: Mass spectrometry signals for $H_2$ generation and $SiH_4$ depletion in W-CVD process from $SiH_4/WF_6$ mixture.

$SiH_4$ reduction process suffers from poor adhesion to the bare Si substrate. Normally the barrier layer TiN would serve as a glue layer and provides good adhesion for W film. However, in our research W was deposited directly on the Si wafer surface with no barrier layer between W film and substrate. For W films thicker than 1000Å, flaking occurs regularly. An expedient solution was to use the Si wafers already covered with W film from previous $H_2$ reduction processes for these $SiH_4$ experiments. This good adhesion of underlying W layer to Si helps to prevent flaking, W films as thick as 3000Å have been obtained successfully by $SiH_4$ reduction. Since the underlying W film had undergone different $H_2$ reduction processes, the surface conditions of these W-capped wafers vary one from each other, which makes the subsequent $SiH_4$ reduction process rather variable in terms of film thickness and quality. But it also provides a perfect scenario to demonstrate the benefit of sensor-based real-time control. Table 3.6 lists the deposition rate and conversion rate of $WF_6$ obtained in $SiH_4$ reduction experiment at $250^0$C and 0.1 torr. Evidently, the conversion rate is about 5 times that of $H_2$ reduction process, which explains the much better metrology results from $SiH_4$ process. It is also quite interesting that no obvious abrupt change of the mass spectrometry signals was observed. See chapter 4 for the plot of the experiment results of the W-Capped wafer.

Table 3.6: Deposition rate and conversion rate of $WF_6$ in W-CVD process from $SiH_4$(8sccm)/$WF_6$(10sccm)/Ar(180sccm) mixture at $250^0$C and 0.1 Torr.

| Wafer # | 1 | 2 | 3 | 4 | 5 | 6 | Average |
|---|---|---|---|---|---|---|---|
| Deposition rate (A/min.) | 1118 | 1138 | 1219 | 1038 | 1048 | 1060 | 1103 |
| Conversion rate | 20.6% | 21.0% | 22.5% | 19.2% | 19.3% | 19.5% | 19.6% |

### 3.4.2.2 Film Characterization.

RBS results (see Figure 3.9) show no obvious difference is seen between the films obtained using $H_2$ and $SiH_4$, although it is expected that film prepared by $SiH_4$ reduction process may contain more Si. However, the AFM images show great difference between them as seen in Figure 3.10 and Figure 3.12 on the next page. The average roughness is reduced to about 12nm.

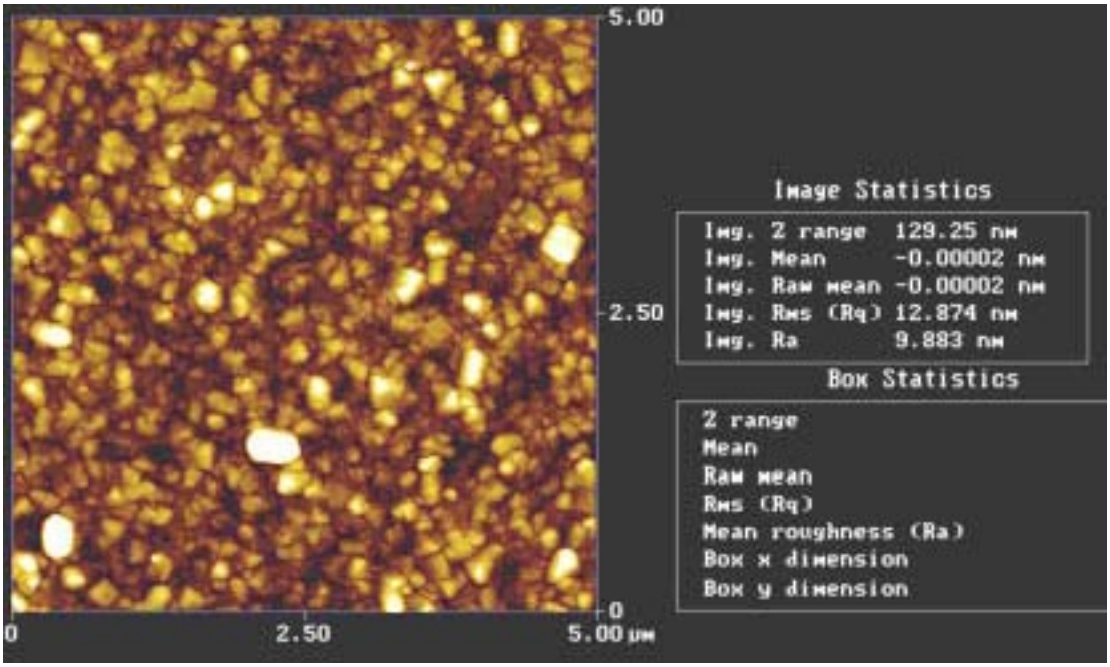


Figure 3.12: AFM image of W film obtained by $SiH_4$ reduction process.

# 4. Experimental Results

## *4.1: W Thin Film Thickness Metrology Using in-situ Mass Spectrometry Sensing.*

Mass spectrometry is capable of providing real-time measurement of individual species concentration in the chemical reaction system. For given stoichiometry of the chemical reaction, the time integration of mass spectrometry signals of these species can be related to the amount of thin film deposited on the substrate. For instance, according to the overall chemical reaction equation of W-CVD by $H_2$ reduction of $WF_6$ as shown below, every 6 molecules of HF will be generated when one W atom is deposited on the wafer. Similarly, every 3 depleted $H_2$ molecules correspond to the deposition of one W atom.

$$WF_6 + 3H_2 \longleftrightarrow W + 6HF$$

Previous research on polysilicon deposition at NCSU [iv] demonstrates that mass spectrometry can use integrated $H_2$ reaction product signals as in-situ measurements of deposited Si thin film thickness with an error of about 10%. The goal of our recent work is to achieve a corresponding mass spectrometry-based thin film thickness metrology in W-CVD process, a more complex reaction system due to the presence of multiple reactants and higher reactivity of reactants and products.

The metrology results obtained from HF signal in $H_2$ reduction process show an uncertainty of around 7%. This accuracy has been improved to better than 2% error using $SiH_4$ reduction process with a higher conversion rate (by a factor of 5), which makes this technique viable for real semiconductor manufacturing.

### 4.1.1: W Thin Film Thickness Metrology in W-CVD Process by $H_2$ Reduction.

#### 4.1.1.1 Metrics for W film thickness metrology.

From the discussion in last chapter, we understand that the observed HF mass spectrometry signal has multiple contributions. Some is from HF generated in the process reaction on the silicon wafer, while other contributions are related to the HF generation in the ion source and wall surface of the reactor representing the background for the true HF generation. Thorough investigation is necessary to quantify the contributions from each different source. To measure the background for HF signal, an unheated wafer cycle is incorporated in the process before the deposition cycle. In this unheated wafer cycle, the same amount of reactants are delivered into the reactor as in the true deposition cycle except that the wafer is not heated and thus no process reaction is likely.

The mass spectrometry signals for HF and $H_2$ recorded in a typical process cycle have been plotted in Figure 4.1. The whole process cycle includes five steps. They are: (i) flush the reactor with $H_2$; (ii) unheated wafer cycle; (iii) heat up wafer; (iv) heated wafer cycle during W deposition on wafer takes place; and (v) cooling down cycle. In the first and last step only $H_2$ (40sccm) flows into the reactor, while in the unheated wafer cycle and heated wafer cycle the same amount of reactants (10 sccm $WF_6$ and 40 sccm $H_2$) are delivered into the reactor. The process conditions are nominally temperature $500^0$C and pressure 0.5 Torr.

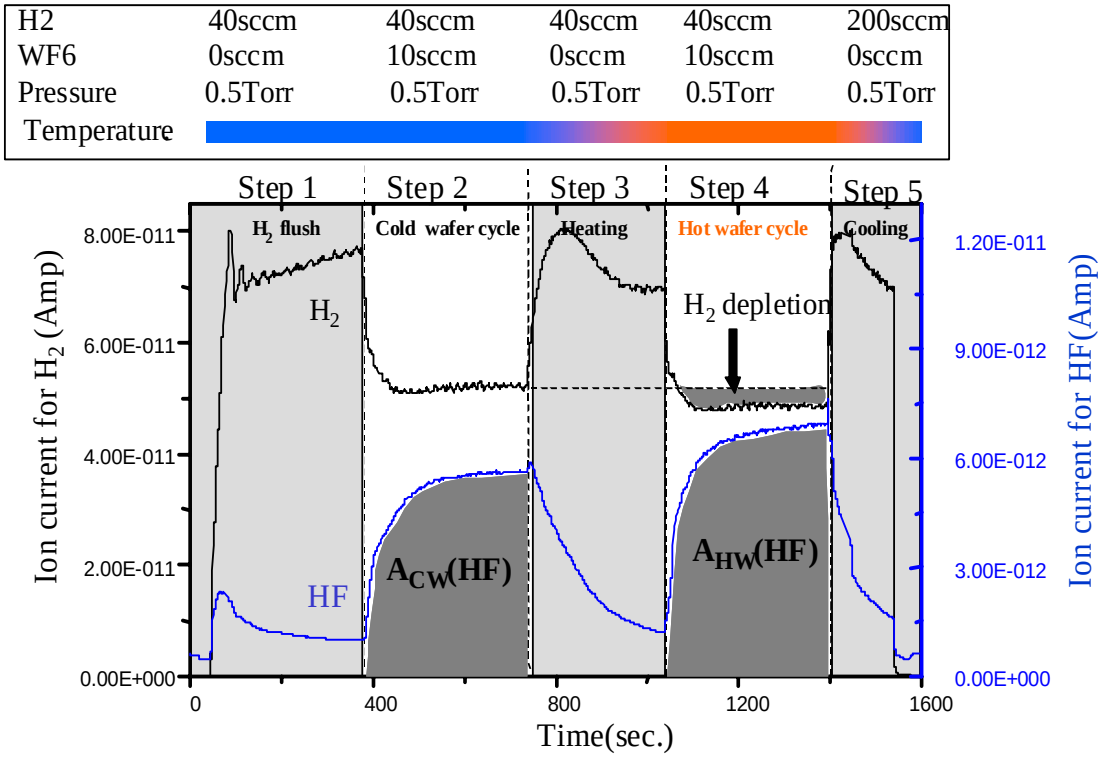


Figure 4.1: Time evolution of $H_2$ and HF mass spectrometry signals in a typical $H_2$ reduction W-CVD process cycle including five steps.

Please note that the temperature measurement using a thermocouple wafer and the simulation of the temperature profile in the reactor show that the wafer temperature may be $150^0$C lower than the nominal temperature and it also takes a long time for the temperature to stabilize at the elevated temperature [liii]. In order to reduce the temperature drift and achieve higher temperature within the deposition cycle, the temperature in the heating up cycle was set up $50^0$C higher than the final deposition temperature in the real deposition cycle.

The significant HF signal observed in the unheated wafer cycle corresponds to the HF generated in the ion source of the mass spectrometry and on the wall of the reactor, when no deposition occurs on the cold wafer surface. The difference between the HF signals in the unheated wafer cycle and in the deposition cycle represents HF generated in the process reaction, which is attribute to the W deposition on the wafer. We normalized this difference by the HF background and finally come up with metrics for the W film thickness as expressed by the following equation 4-1

$$S_{HF} = \frac{A_{HW}(HF) - A_{CW}(HF)}{A_{CW}(HF)} \times t \qquad (4\text{-}1)$$

Where A is the area beneath the HF signal, i.e. the time integration of HF signal; HW denotes hot wafer cycle; CW symbolizes cold wafer cycle; t represents the deposition time. Similarly for $H_2$ depletion, the metrology signal is formulated by equation 4-2, indicating a decrease in $H_2$ signal from "cold wafer" to "hot wafer" stage due to the depletion of $H_2$ in the process reaction.

$$S_{H_2} = \frac{A_{CW}(H_2) - A_{HW}(H_2)}{A_{CW}(H_2)} \times t \qquad (4\text{-}2)$$

While the above mathematical manipulation may seem somewhat cumbersome, it compensates for two important effects so that we can compare results obtained on different days. First it subtracts the background signal associated with the species observed during cold wafer cycle. Second it normalize the (hot-cold) metric signal by dividing the cold wafer signal.

#### 4.1.1.2 Metrology results based on HF signal and $H_2$ signal in $H_2$ reduction process

Figure 4.2 depicts the time evolution of $H_2$ and HF mass spectrometry signals recorded in a 3-wafer deposition run. Altogether about 40 wafers have been processed under the same processing conditions, except the deposition times are varied. The normalized HF generation signals and $H_2$ depletion signals of all these wafers have been calculated according to equation 4-1 & 4-2 and plotted vs. W thin film thickness as shown in Figure 4.3 & Figure 4.4. A linear relationship is evident in the metrology result from HF signal with the correlated coefficients equal to 0.95.

Please note that the linear regression fit intercept the Y-axis at about 318 Å, which implies that a layer of W film was deposited without generating HF. We associate this intercept with the W film deposited during the nucleation stage by Si reduction, for no HF is generated in the Si reduction reaction. To verify the above assertion, the $H_2$ reagent was substituted by Ar and a few deposition runs were carried out. In the absence of $H_2$ only Si reduction reaction may occur, and the weight of the

W seed layer was found 265 ± 20 Å, close to the value (318 ± 47Å) obtained by the HF data. This value is also in line with the published research results in the literature.

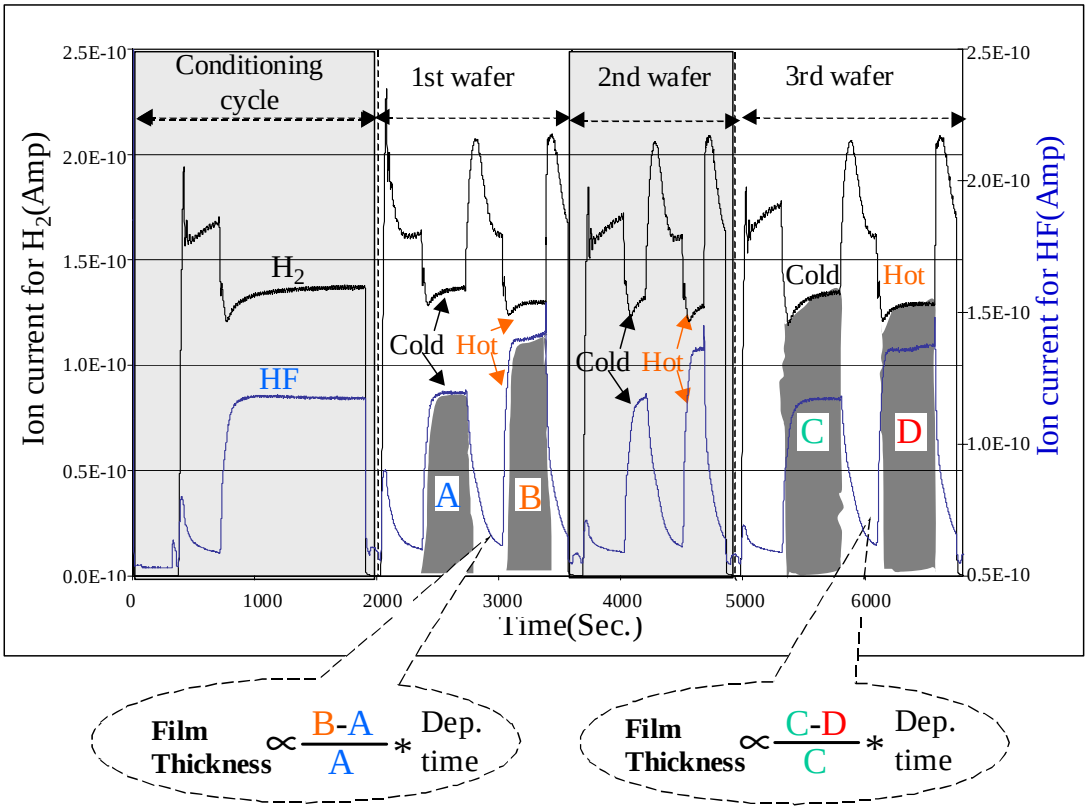


Figure 4.2: Time evolution of the HF and $H_2$ mass spectrometry signals recorded in a 3-wafer deposition run by $H_2$ reduction of $WF_6$. A conditioning cycle of about 30 minutes is included before the process to equilibrating the reactor and the sampling system. The process conditions for all these wafers are exactly the same except for the deposition time.

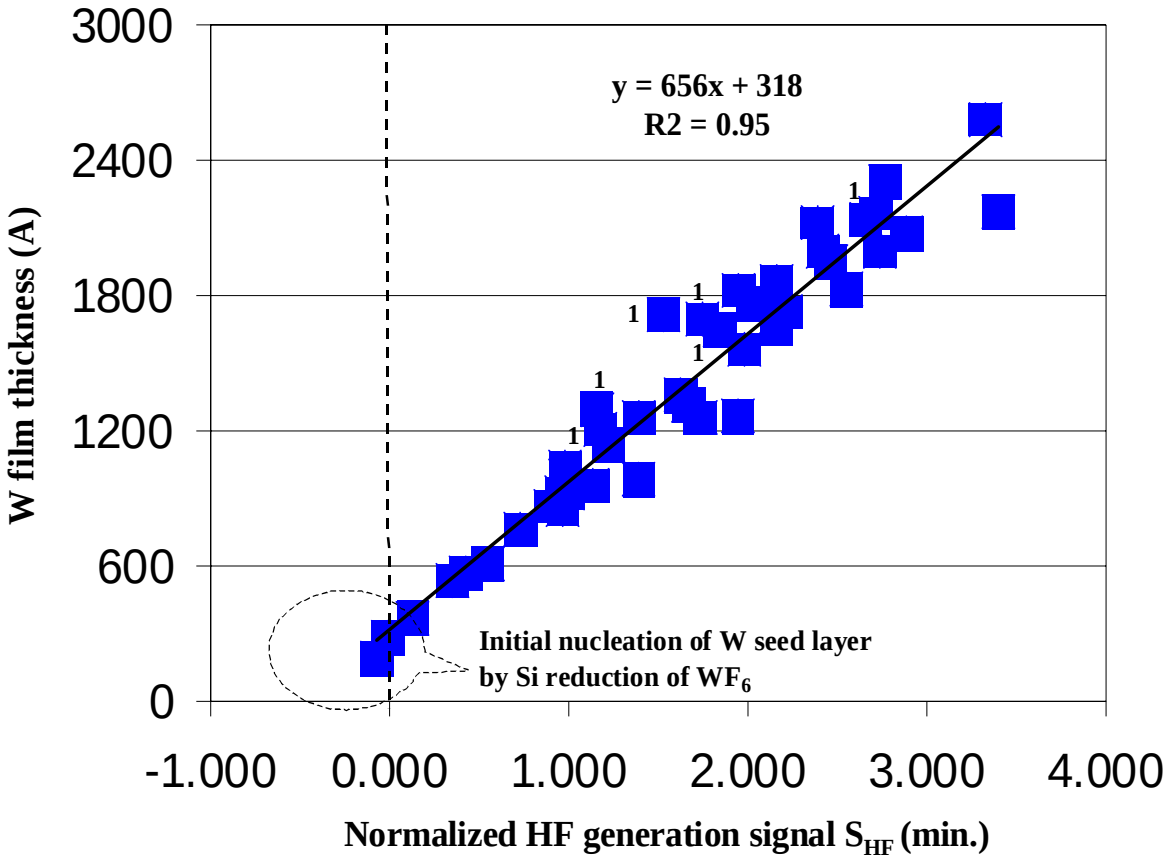


Figure 4.3: Metrology results from $S_{HF}$ in $H_2$ reduction W-CVD process

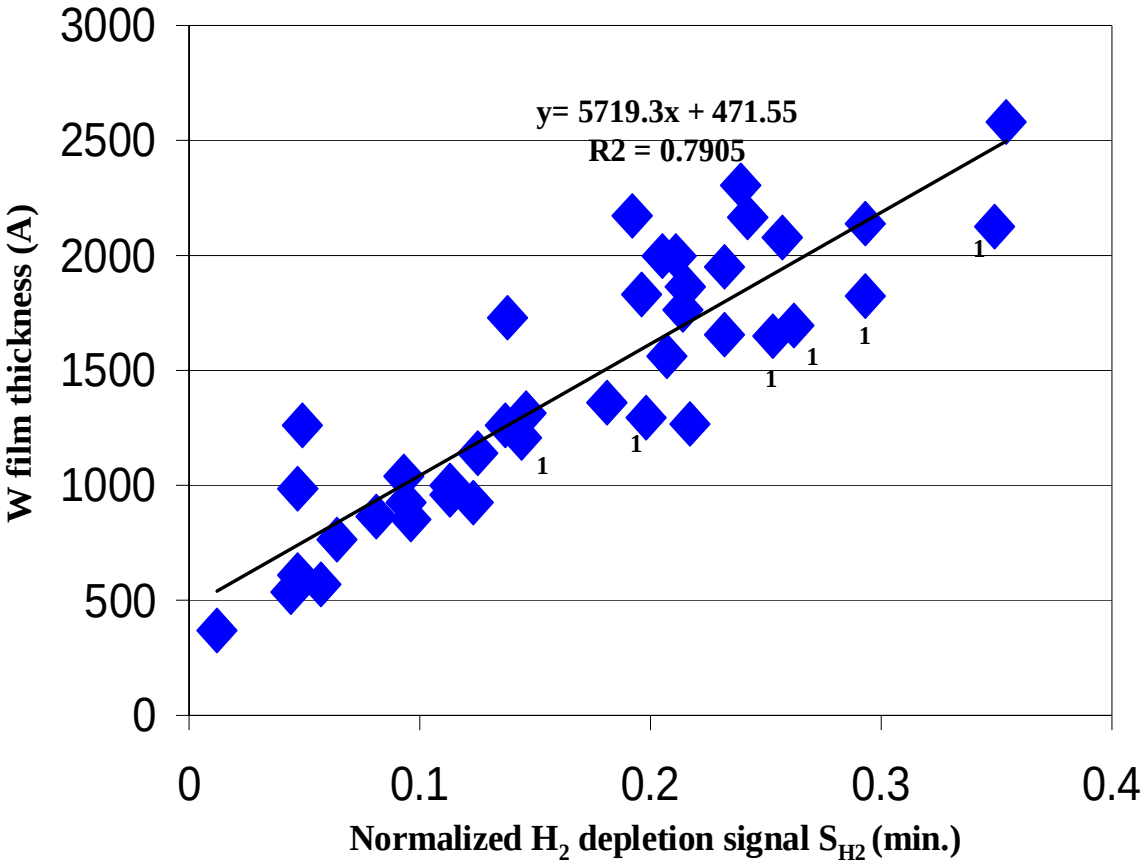


Figure 4.4: Metrology results from $S_{H2}$ signal in $H_2$ reduction W-CVD process.

To have a better evaluation of the metrology results, the residual for each data point was calculated, where the residual is defined as the difference between the actual y-values for each data point and the values resulting from the linear regression fitting. Then the absolute value of the residual was divided by the measured value to obtain the relative error. The average uncertainty calculated for the HF data was 7% while for the $H_2$ data was 16%. For the deposition of 5000Å W, that corresponds to error of about 350Å and 800Å respectively. Obviously the $H_2$ depletion signal does not produce as good a thickness metrology indicator as HF generation signal does. This is not a surprise at all considering the extremely low conversion rate of $H_2$ (3%).

Much better results can be expected if the conversion rate is improved to be comparable to today's industry standard which is 40-50% conversion. Two approaches have been considered to enhance the utilization of the reactants. (1) increase the process temperature and pressure, or (2) use a more efficient reducing agent to replace $H_2$. Since (1) involves substantial equipment modification (now in progress), we chose to concentrate on (2), employing the $SiH_4$ reduction process. As shown in Table 3-6, much higher conversion rates have been achieved leading to improved metrology results.

#### 4.1.1.3 First wafer effect.

Some data points in Figure 4.3 & Figure 4.4 are marked by a number “1”. These points represent the first wafers in each batch (total of 6 batches). For the HF based metrology, these points exhibit a systematic deviation from the linear regression fitting: all such points lie to the “left and above” of the best fit, while for the $H_2$ data, they all lie to the “right and below” of the regression line. The explanation to this systematic deviation can be found by a close look at the mass spectrometry signal in Figure 4.2. It is clear that in the cold wafer cycle of the first wafer, the HF signal baseline is somewhat higher than the baseline for the succeeding wafers. The reason is that during the cooling cycle of each wafer, the $H_2$ flow helps to remove the absorbed $WF_6$ from the wall and leaves a relatively cleaner surface for the next wafer. Therefore the HF generation in the cold wafer cycle caused by the wall reaction will be reduced for the following wafer. That is why the first wafer usually has the largest HF signal baseline. Such a large HF baseline for the first wafer will lead to an overestimation of $A_{cw}(HF)$ and thus a undervalued HF generation signal $S_{HF}$ according to equation 4-1,

which explains the observed first wafer effect. For the same reason, a larger $S_{H2}$ value will result from the smaller $H_2$ signal baseline (generation and depletion signal always show the opposite behavior) and consequently all the $H_2$ based first wafer data points sit to the right of the fitting line.

### 4.1.2: W Thin Film Thickness Metrology in W-CVD Process by $SiH_4$ Reduction.

#### 4.1.2.1 Metrics for W film thickness metrology.

To enhance the reactant conversion rate, we initiated W-CVD process using $SiH_4$ as the reducing agent. The overall chemical reaction equations are shown below.

$$3SiH_4 + 2WF_6 \longleftrightarrow 2W + 3SiF_4 + 6H_2$$

or $$2SiH_4 + WF_6 \longleftrightarrow W + 2SiHF_3 + 3H_2$$

Figure 4.5 shows $H_2$, $SiF_3$, and $SiH_2$ mass spectrometry signals in a typical process cycle. Just like $H_2$ reduction process, an unheated wafer step was incorporated and altogether the whole process cycle consists of 5 steps. What is different this time is that both $H_2$ and $SiF_3$ signals are quite small in the unheated wafer cycle, only 10% of the values in the heated wafer cycle, which suggests a higher deposition rate and less wall reaction. The metric defined for the W film thickness using $H_2$ generation signal can be expressed by the following equation 4-3.

$$S_{H_2} = A_{HW}(H_2) - A_{CW}(H_2) \qquad (4\text{-}3)$$

Where A is the area beneath the $H_2$ signal, i.e. the time integration of $H_2$ signal; HW denotes hot wafer cycle; CW symbolizes cold wafer cycle. Because no obvious drift of the sensitivity was observed, the normalization procedure carried out

during analyzing the $H_2$ reduction experiments results is saved. That is why $A_{HW}(H_2)$-$A_{CW}(H_2)$ i.e. the difference between integrated $H_2$ signals in unheated wafer cycle and heated wafer cycle is not divided by $A_{CW}(H_2)$. Similarly, the metrics based on $SiF_3^+$ and $SiH_2^+$ signal can be formulated by equations 4-4 & 4-5.

$$S_{SiF_3} = A_{HW}(SiF_3) - A_{CW}(SiF_3) \tag{4-4}$$

$$S_{SiH_2} = \frac{A_{CW}(SiH_2) - A_{CW}(SiH_2)}{A_{CW}(SiH_2)} \times t \tag{4-5}$$

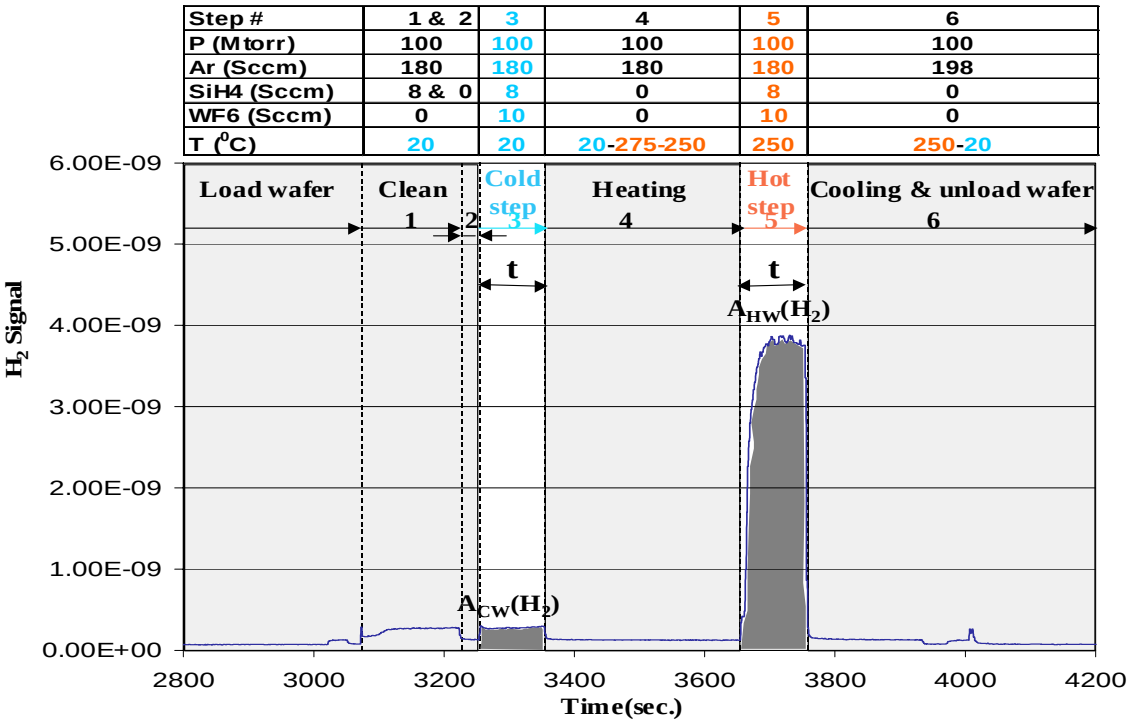
Step # | 1 & 2 | 3 | 4 | 5 | 6
P (Mtorr) | 100 | 100 | 100 | 100 | 100
Ar (Sccm) | 180 | 180 | 180 | 180 | 198
SiH4 (Sccm) | 8 & 0 | 8 | 0 | 8 | 0
WF6 (Sccm) | 0 | 10 | 0 | 10 | 0
T (°C) | 20 | 20 | 20-275-250 | 250 | 250-20
Load wafer
Clean
Cold step
Heating
Hot step
Cooling & unload wafer
1
2
3
4
5
6
t
t
$A_{HW}(H_2)$
$A_{CW}(H_2)$
$H_2$ Signal
6.00E-09
5.00E-09
4.00E-09
3.00E-09
2.00E-09
1.00E-09
0.00E+00
2800
3000
3200
3400
3600
3800
4000
4200
Time(sec.)

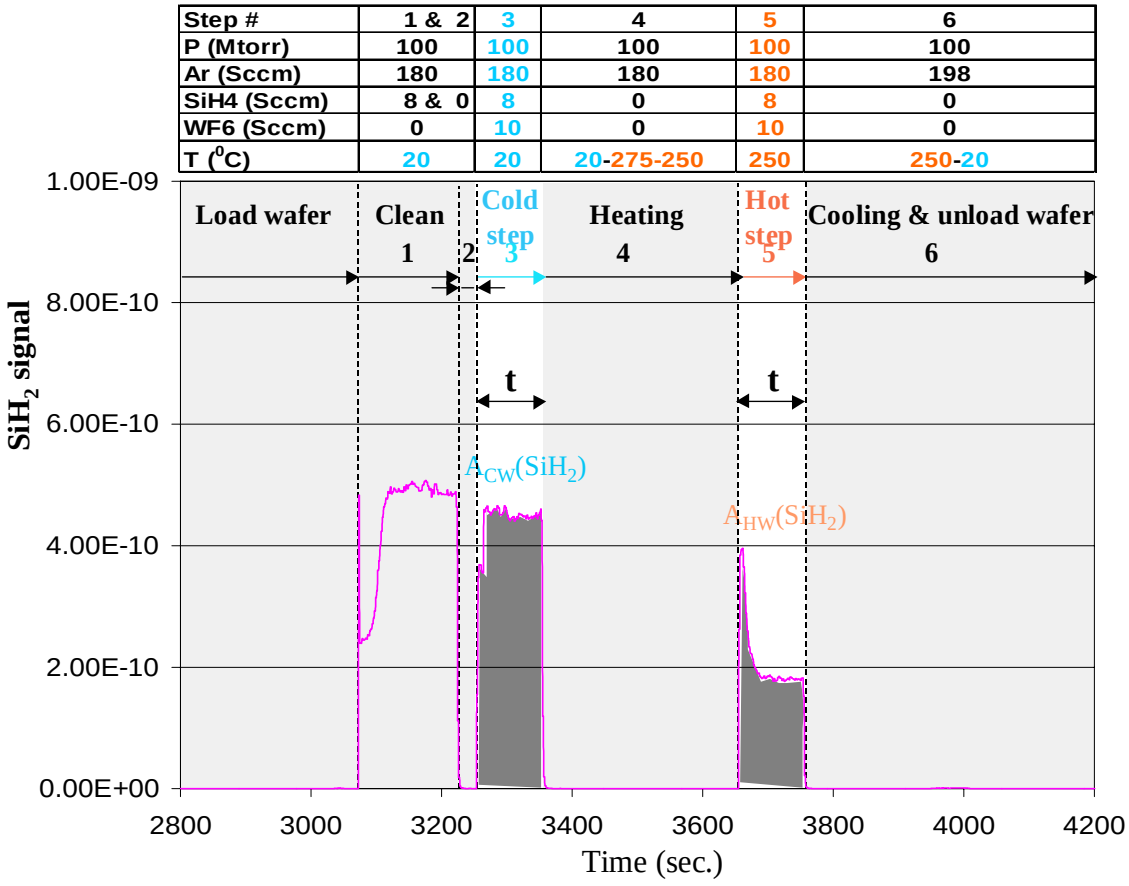
Step # | 1 & 2 | 3 | 4 | 5 | 6
P (Mtorr) | 100 | 100 | 100 | 100 | 100
Ar (Sccm) | 180 | 180 | 180 | 180 | 198
SiH4 (Sccm) | 8 & 0 | 8 | 0 | 8 | 0
WF6 (Sccm) | 0 | 10 | 0 | 10 | 0
T (°C) | 20 | 20 | 20-275-250 | 250 | 250-20
Load wafer
Clean
Cold step
Heating
Hot step
Cooling & unload wafer
1
2
3
4
5
6
t
t
$A_{CW}(SiH_2)$
$A_{HW}(SiH_2)$
$SiH_2$ signal
1.00E-09
8.00E-10
6.00E-10
4.00E-10
2.00E-10
0.00E+00
2800
3000
3200
3400
3600
3800
4000
4200
Time (sec.)

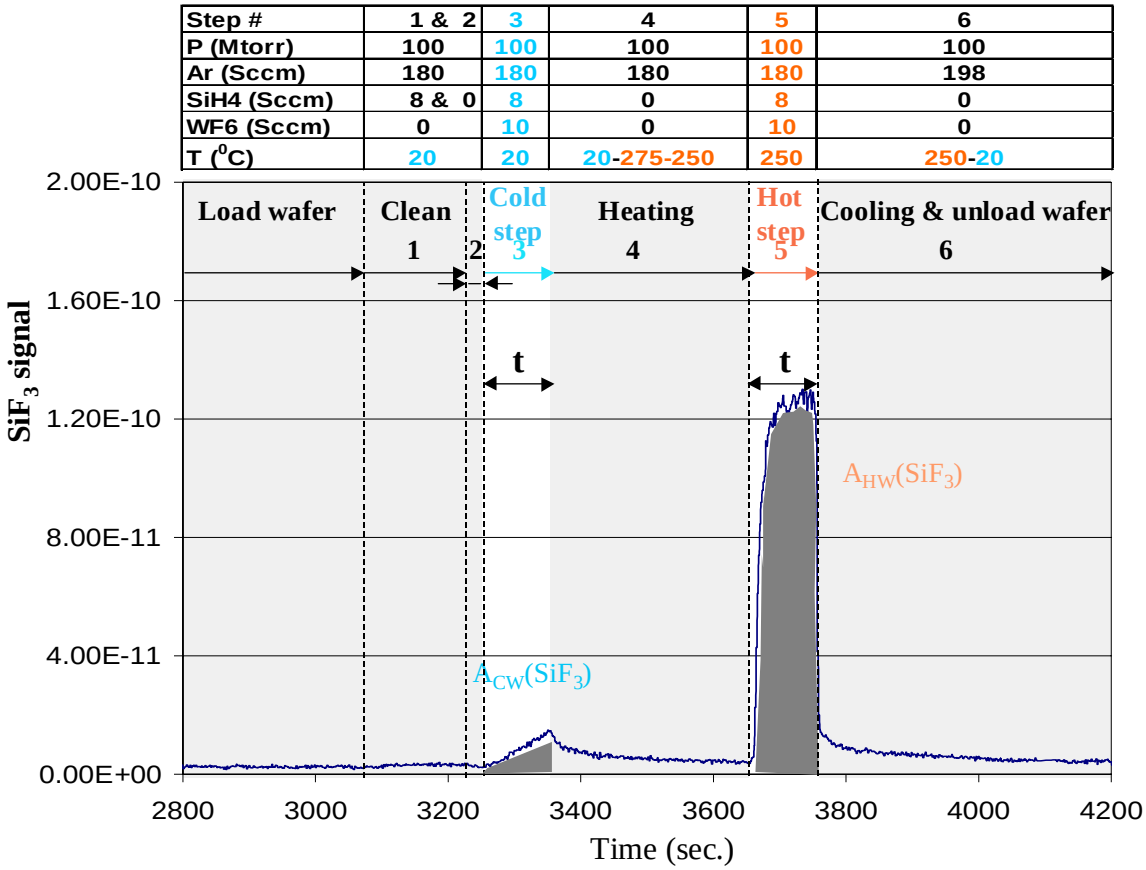


Figure 4.5: Time evolution of $H_2$, $SiF_3$, and $SiH_2$ mass spectrometry signals in a typical $SiH_4$ reduction W-CVD process.

#### 4.1.2.2 Metrology results based on $H_2$, $SiF_3$, and $SiH_2$ signals in $SiH_4$ reduction process

A total of about 37 wafers have undergone the same processes as illustrated in Figure 4.5 with varying deposition times. A linear relationship was established between the film thickness and integrated mass spectrometry signals $S_{H2}$, $S_{SiF3}$, $S_{SiH2}$ derived from equations 4-3, 4-4, and 4-5 (see Figure 4.6, Figure 4.7, and Figure 4.8. All these three sets of data show significant improvement over the metrology result of $H_2$ reduction process, while $S_{H2}$ yields the best fitting with the film thickness with a correlated coefficient $R^2$ of 99%. The improvement in the accuracy of the metrology results is manifested best by a comparison of the statistical data (see Table 4.1), where residue and relative error are defined as explained in previous section 4.2.1.2. A plot of the relative error of each wafer vs. the processing time shows no obvious correlation between the magnitude of the error and the processing time (see Figure 4.9).

No first wafer effect was found in the $H_2$ product data for $SiH_4$ reduction. Unlike experiments with $H_2$ reduction, the regression fitting lines obtained here point to the origin of the axis with no intercept. That is because the $SiH_4$ reduction process dominates over Si reduction and there is only minimal wall reaction.

Table 4.1: Comparison of the statistic analysis data for the metrology results of $H_2$ reduction process and $SiH_4$ reduction process. The metrology results from $A_{HW}(H_2)$ was improved to $1.55 \pm 1.38\%$. $A_{HW}(H_2)$ is the integration of $H_2$ signal in the deposition cycle.

| Process | $H_2$ reduction | | $SiH_4$ reduction | | | |
|---|---|---|---|---|---|---|
| Metrology | $S_{H2}$ | $S_{HF}$ | $S_{H2}$ | $A_{HW}(H_2)$ | $S_{SiF3}$ | $S_{SiH2}$ |
| Average | 16.1% | 6.45% | 1.25% | 1.55% | 1.86% | 2.83% |
| Standard deviation | 11.8% | 5.56% | 1.09% | 1.38% | 1.38% | 2.59% |

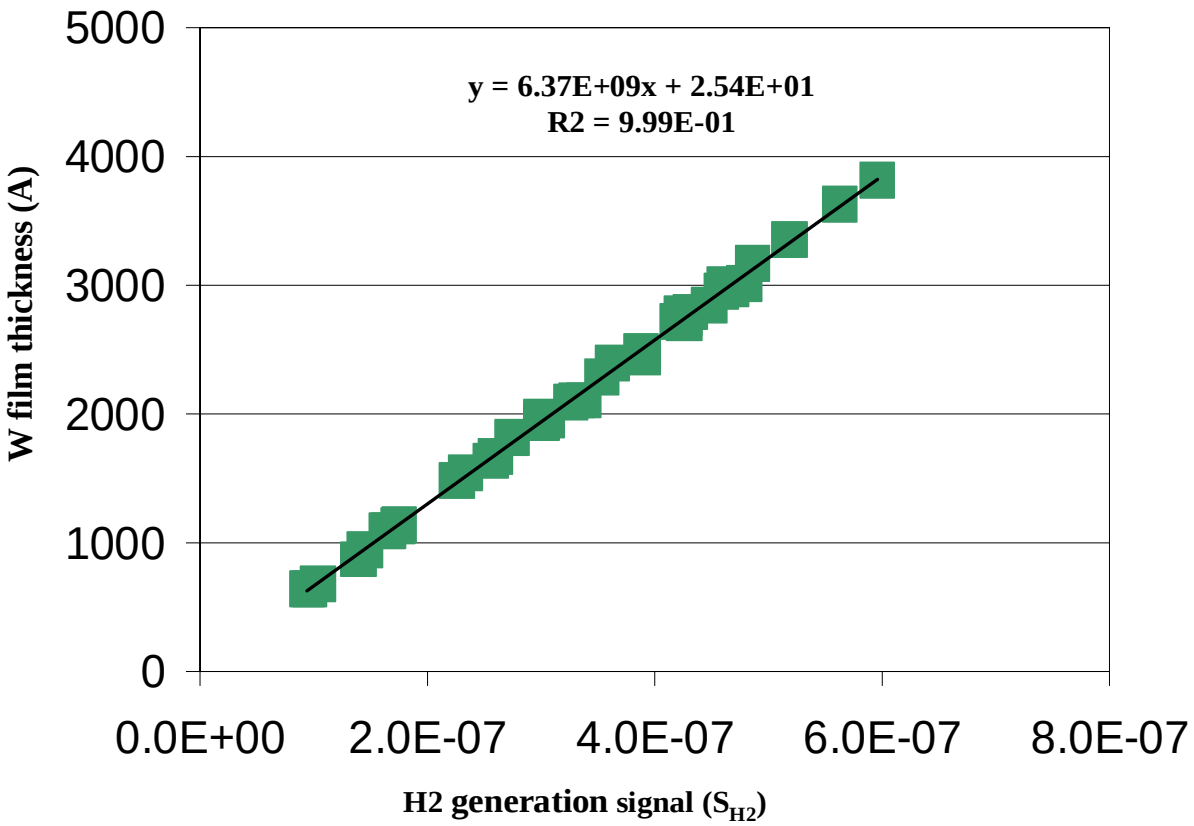


Figure 4.6: Metrology results from $S_{H2}$ in $SiH_4$ reduction W-CVD process.

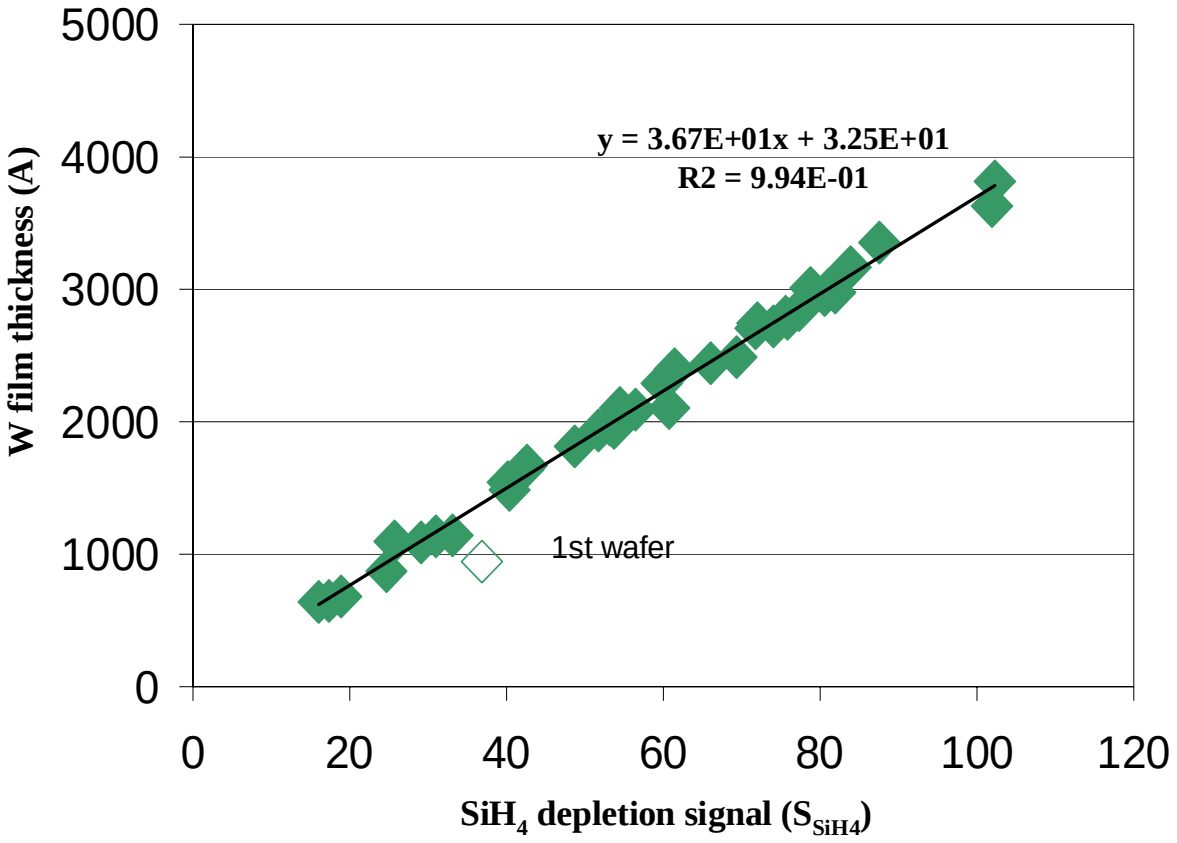


Figure 4.7: Metrology results from $S_{SiH2}$ signal in $SiH_4$ reduction W-CVD process.

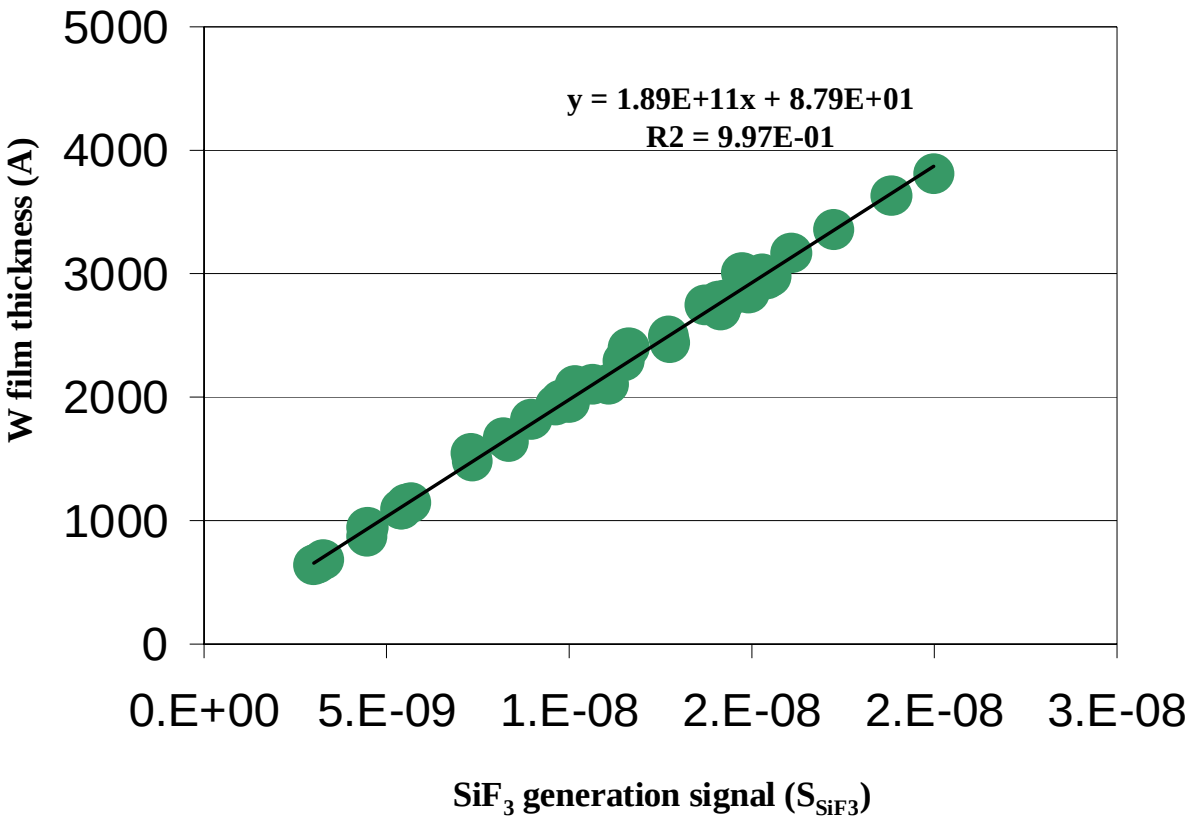


Figure 4.8: Metrology results from $S_{SiF3}$ signal in $SiH_4$ reduction W-CVD process.

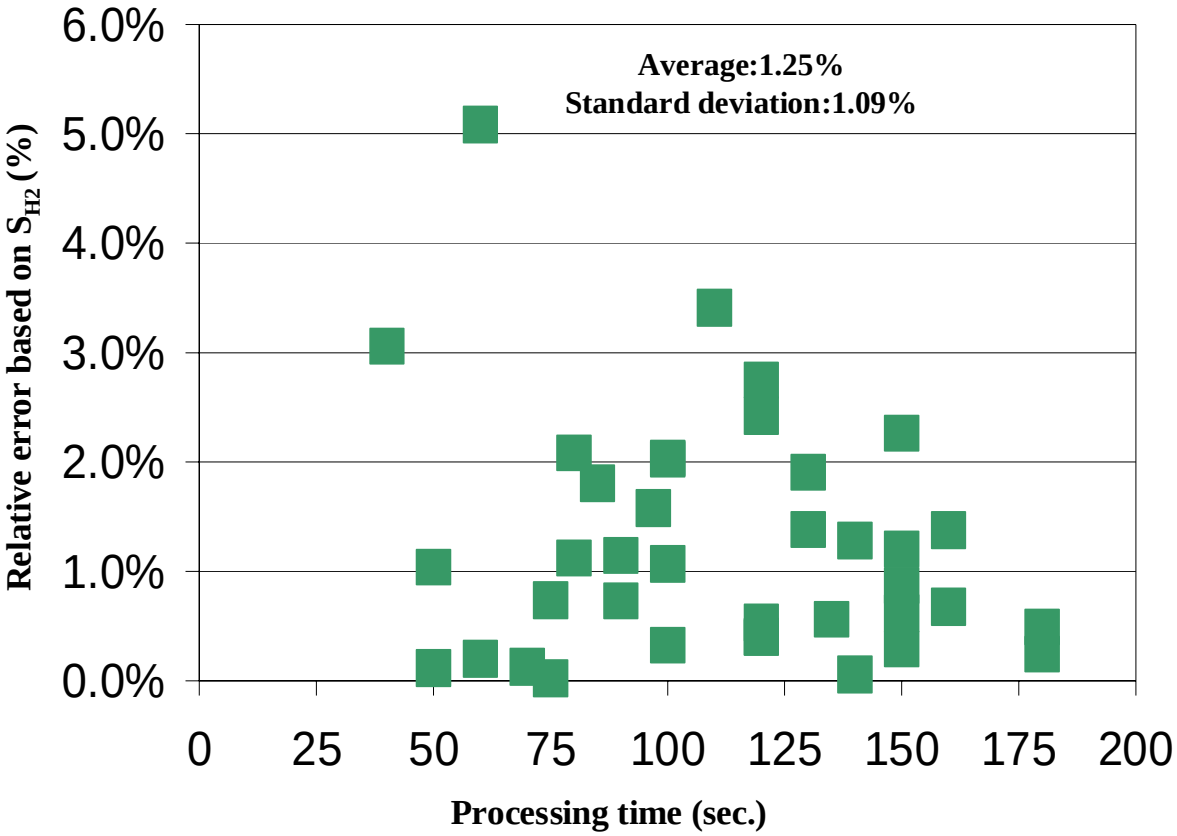


Figure 4.9: Plot of the metrology error based on $S_{H2}$ vs. the processing time.

The experiment with $SiH_4$ reduction owes its success to two factors: (i) higher conversion rate, (ii) small drift due to wall reaction and sensor. As we noted before the cold wafer cycle was critical to the metrology development for $H_2$ reduction process. However, this nonproductive step is absolutely not acceptable in real semiconductor manufacturing because it would noticeably increase cycle time and cost. The higher conversion rate present in this $SiH_4$ reduction process clearly enables the omission of the cold wafer cycle. We expect conversion rates at least this high to be typical in

CVD manufacturing processes, so the prognosis for mass spec. based thickness metrology is good.

Analysis ignoring the unheated wafer cycle was also carried out. $A_{HW}(H_2)$ was plotted vs. film thickness in Figure 4.10. The open data points present the results from the previous 37 wafers, while the solid data points were obtained in process with no cold wafer cycle. The solid data points are all slightly to the right of the fitting line. That is because after running for about 5 weeks (on the average two days a week, 8 hours a day) deposition started to occur on the wall. Therefore for the same mass spectrometry signal, a small part of the film was grown on the reactor wall and showerhead instead of the wafer surface. The statistical analysis indicates that the average error and standard deviation for metrology results from $A_{HW}(H_2)$ are 1.55% and 1.38% respectively, which implies that omitting an unheated wafer cycle is essentially equivalent in accuracy. In the succeeding W film thickness real-time control experiments all wafers were processed without unheated wafer cycle, and $A_{HW}(H_2)$ instead of $S_{H2}$ was taken as the control variable.

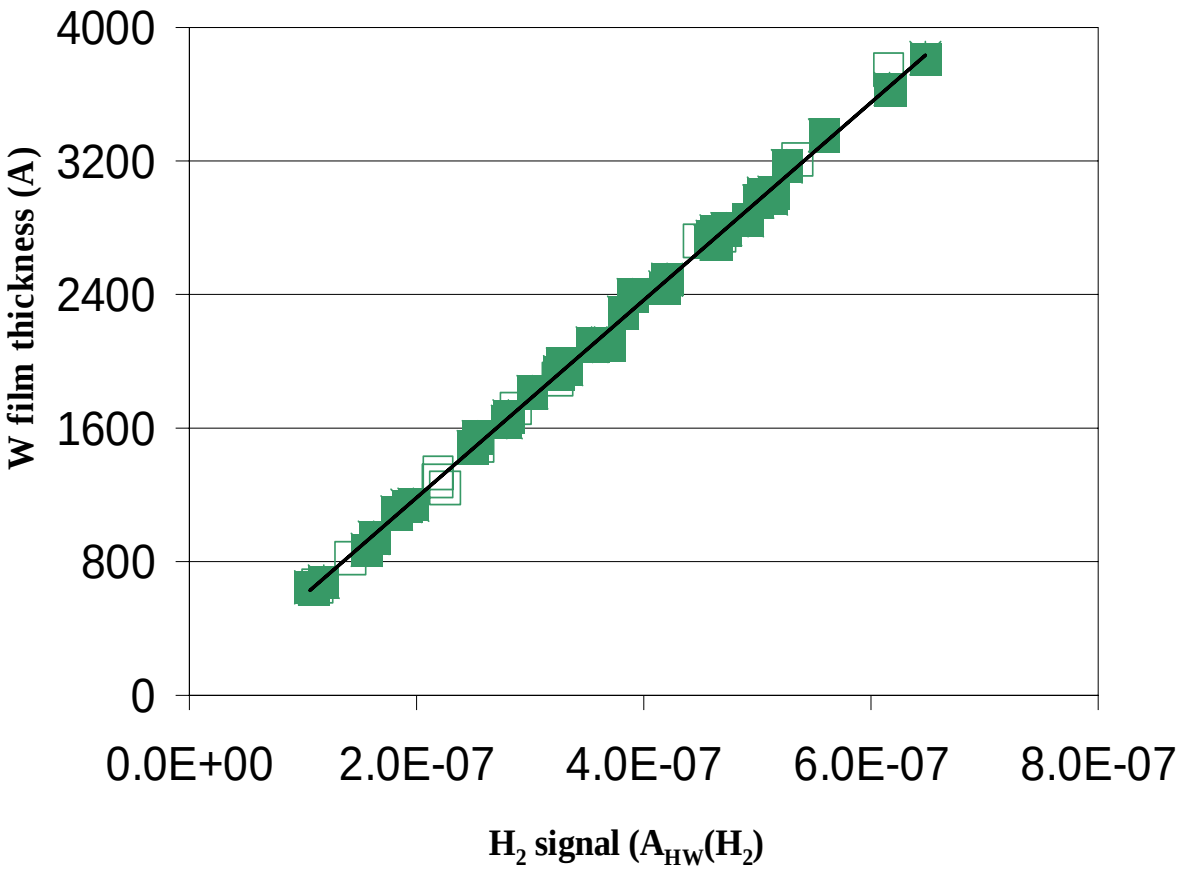


Figure 4.10: Metrology results from $A_{HW}(H_2)$ in $SiH_4$ reduction W-CVD process.

### *4.2: Mass Spectrometry-based Process Control of W Thin Film Thickness*

Mass spectrometry-based W thin film thickness control is the goal of our research. It justifies all the efforts to develop the film thickness metrology using mass spectrometry. From the previous section, we know that W film thickness metrology has been established successfully in both $H_2$ reduction process and particularly in $SiH_4$ reduction process. Plots in Figure 4.3 & Figure 4.6 indicate the obvious linear relationship between the integrated mass spectrometry signals and the film thickness. The uncertainties of 7% and 2% are not perfect but sufficient for us to exploit sensor-based process control. The objective of the control experiments is to develop a control

methodology which exploits *in-situ* sensor-based metrology to maintain the W film thickness at target by adjusting deposition time in the presence of disturbance; either systematic or random. Two different control strategies have been applied in the control experiments: run-to-run control (for $H_2$ reduction W-CVD process) and real-time end point control (for $SiH_4$ reduction W-CVD process). The experimental results indicate that run-to-run control can handle systematic drift well, but random variation can be controlled only by real-time control.

### 4.2.1: Run-to-run Control of W Thin Film Thickness in W-CVD Process by $H_2$ Reduction.

From the metrology results, we know that film thickness can be controlled at the target by controlling the mass spectrometry signal. In W film thickness control experiments, two linear static models derived from the W film thickness metrology results (with an error of about 7%) were employed to drive a robust IMC run-to-run control algorithm system as shown in section 2.3. To demonstrate the benefit of this sensor-based run-to-run process control, a systematic temperature drift of $-5^0$C per wafer was introduced deliberately[7], which would result in the film thickness declining by 40-50% after 10 wafers, i.e. $50^0$C decrease. In the run-to-run control system as shown in section 2.3, normalized HF generation signal (defined by equation 4-1) was taken as the control variable. The deposition time was adjusted according to compensate the effect of temperature drift on the deposition in order to maintain the HF generation signal at target.

[7] The temperature drift is added because it is our observation that in the absence of disturbance, the process variation will be less than 7%, which is the accuracy of the metrology

#### 4.2.1.1 Linear static models for run-to-run control algorithm.

Two linear static models had been obtained from a set of $H_2$ reduction W-CVD processes with about 40 wafers and are explicitly stated below.

1. A model between the W film thickness with the deposition time (Figure 4.11 (a)).
2. A model between the normalized HF signal ($S_{HF}$ as defined by equation 4-1) and the deposition time (Figure 4.11 (b)).

The first model was applied with the off-line actual film thickness measurement to test the control algorithm and the second model then was incorporated into the controller for sensor-based process control.

#### 4.2.1.2 Run-to-run control experiment results.

Initial experiments were performed with the micro-balance so as to test the robustness of the control algorithm described in chapter 2. The experiment results are plotted in Figure 4.12. A target W film weight of 0.02 g was chosen, corresponding to a deposition time of 5.82 minutes according to the model relating the W film weight to the deposition time (bullet one above). The W film weight obtained during the first run is somewhat different from the target value due to the plant-model mismatch. Consequently for the first 6 wafers, the type I controller was doing the job to handle the discrepancy between the static model and the plant, which is considered as step like disturbance. After 6 wafers, a temperature drift of $-5^0$C was introduced and the controller was switched to type II controller, which is designed to handle aging-like drift. Figure 4.12 indicates that this control is successful to about 3%, which we

estimate as the micro-balance accuracy. Also depicted in Figure 4.12 is the projected W film weight in an open loop system showing a large declining of the film weight if no correction action was taken to compensate for the temperature drift.

Figure 4.11: Linear static model for run-to-run process control (a) model between W film thickness and deposition time, (b) model between HF generation signal and

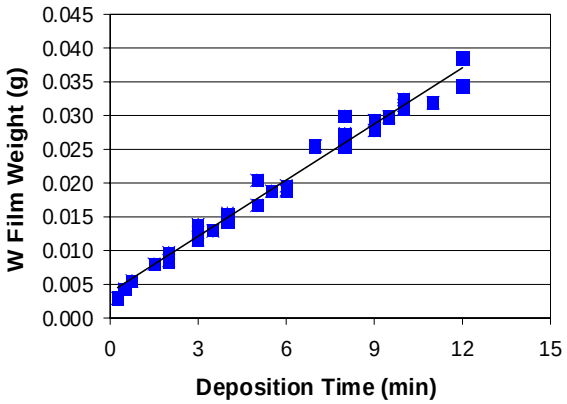


Film Weight (g)=0.0028 * t + 0.0035

(a)

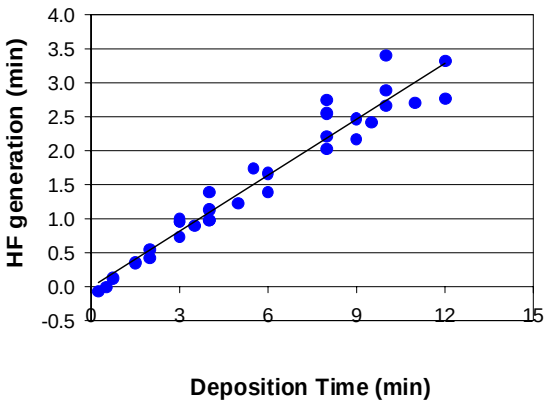


HF generation (min)=0.2751 * t -0.0146

(b)

deposition time.

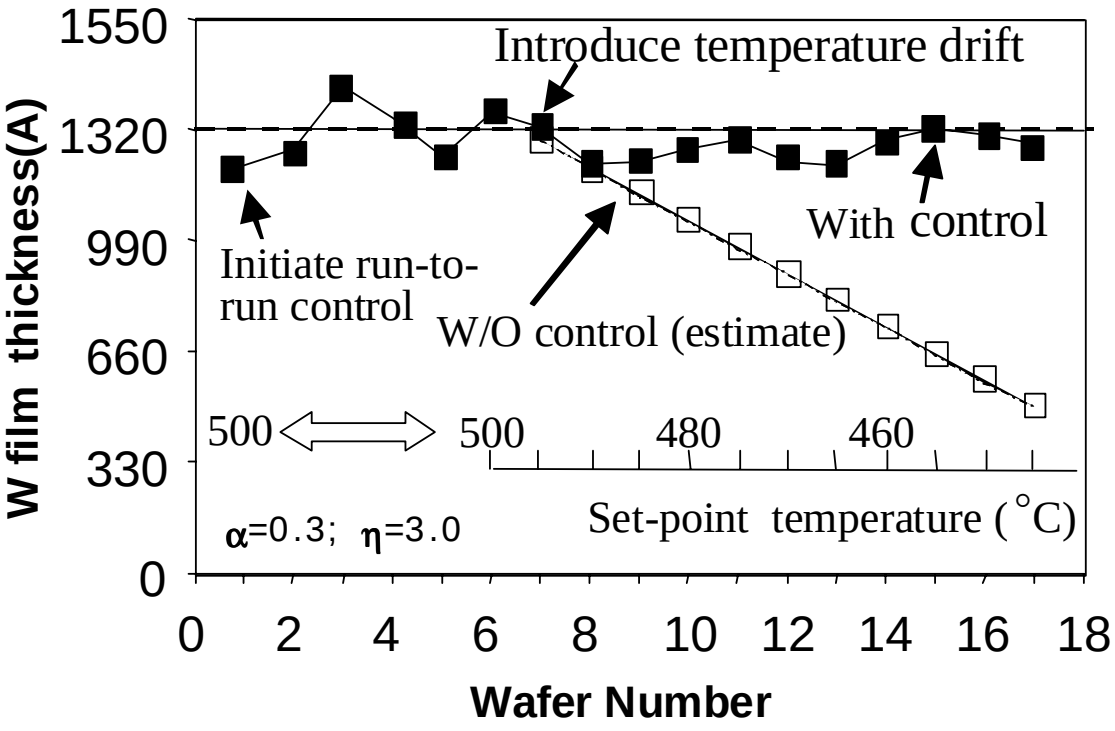


Figure 4.12: W film thickness vs. run number. A target of 1320Å was set for W film thickness and the film thickness derived from the film weight was taken as the input for the controller. After 6 wafers were processed with type I controller, a temperature drift of $-5^0$C per run was introduced. The controller was trying to maintain the film thickness from dropping due to the temperature drift by adjusting the deposition time.

Following the test of control algorithm, the linear static model relating the integrated HF generation signal to the deposition time (bullet two above) was applied in the real test for the potential use of sensor-based metrology as a basis for run-to-run control applications. We are trying to bring and maintain the W film thickness constant by keeping the HF signal at target. Here the HF signal obtained for the first wafer was taken as the target value and we started introducing temperature drift since

the second wafer. This way the discrepancy between the model and the plant is eliminated, which saves us several runs with the type I controller. The experiment results are shown in Figure 4.13. We can see that the HF generation signal is controlled within 10% of the target value. The curve of projected HF signal without control in Figure 4.13 (a) is derived from the experiment results by rescaling the deposition time and shows what the temperature drift would have done without control. In these experiments, post process measurements of the film weight were also carried out (see Figure 4.13 (b)) but not used for control. As seen in Figure 4.13 (b), the W film weights resulting from run-to-run control of the *in-situ* HF metrology signal were fairly stable and were about 7-8% off the target value, which is comparable to the accuracy of the metrology.

The experiments discussed above demonstrate that wafer state metrology based on *in-situ* mass spectrometry can provide a basis for effective run-to-run control in the presence of significant systematic process drift. Control results consistent with the metrology capability had been obtained and the benefit from sensor-based control is obvious. Improvements in metrology accuracy are necessary in attempt to achieve better control results.

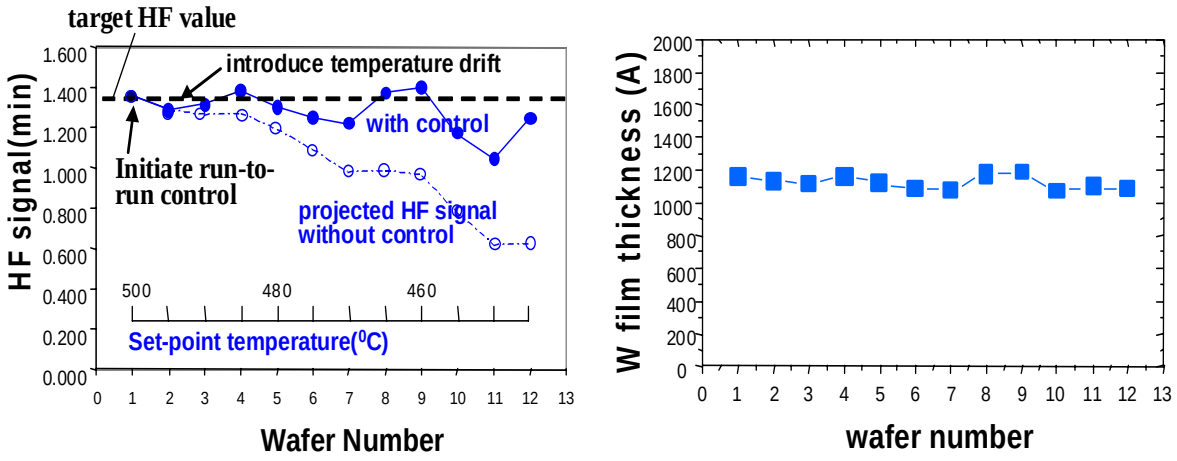


Figure 4.13: (a) Integrated HF generation signal vs. run number. The initial run defines the target HF value and the temperature drift was introduced from the second run. (b) W weight vs. run number.

### 4.2.2: Real-time Control of W Thin Film Thickness (Endpoint Detection) in W-CVD Process by $SiH_4$ Reduction.

The run-to-run control experiments in $H_2$ reduction W-CVD process bring us to a conclusion that the robust IMC run-to-run control algorithm can handle systematic long-term process drift effectively (on the time scale of multiple wafers). The presence of random disturbance in contrast requires real-time process control. Real-time end point process control using integrated mass spectrometry signal has been performed in $SiH_4$ reduction W-CVD process. This practice is similar to the application of mass spectrometry in end point detection in plasma etch, except that here it is our attempt to keep the integrated mass spectrometry at target so as to maintain the film thickness constant. Because the uncertainty of the metrology results for $SiH_4$ reduction process

is better than 2%, which is less than the process variation[8], real-time process control was implemented in processes with deliberately introduced temperature drift (as in the run-to-run control experiments) and with no intentional disturbance at all.

The methodology can be perceived like this: $H_2$ reaction product is monitored in real-time and the integration of $H_2$ signal over the process time is calculated and taken as the control variable. Whenever the integrated signal reaches the pre-selected target value, the process will be terminated. See Figure 4.14. The W film thickness metrology illustrated in Figure 4.10 determines that the film thickness will be kept constant with a constant integrated $H_2$ signal.

It is worth mentioning that in order to enable real-time control, a new Brooks™ control system was used to substitute the original Ulvac controller for CVD process execution, which offers a lot more flexibility, allowing us to terminate the process as the mass spectrometry signal hits the trigger value.

[8] The wafers used in $SiH_4$ reduction process had undergone different H2 reduction processes. The surface status varies one from each other, which led to larger process variation than normal.

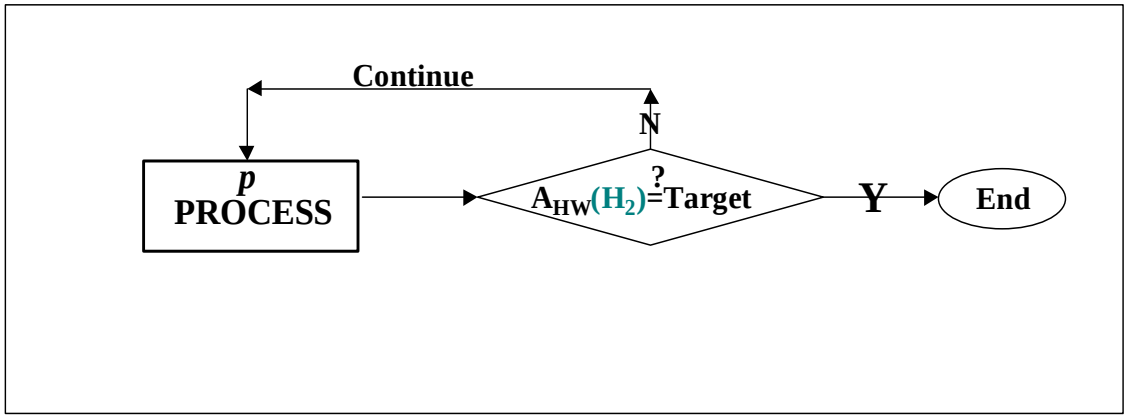


Figure 4.14: Diagram of real-time end point control algorithm.

The two sets of control experimental data are shown in Figure 4.15 & Figure 4.17. In Figure 4.15, the first wafer defines the target integrated $H_2$ value $A_{HW}(H_2)$ of 4.3E-7 (amp-Sec.). The same target was used in the succeeding experiments too. The measured film weight of the first wafer is 0.0375 g as compared to 0.0385g, the calculated film weight corresponding to an integrated $H_2$ value of 4.3E-7 (amp-Sec.) based on the $H_2$ metrology results illustrated in Figure 4.10, which gives a 2.5% error. Similar to run-to-run control experiment, a systematic temperature drift of $-10^0$C per run initiated since the third wafer. The deposition time is adjusted in real-time such that the control variable, i.e. $A_{HW}(H_2)$ is kept at the target. The solid data points represent $A_{HW}(H_2)$ and film weight obtained with control; the open data points indicate the projected $A_{HW}(H_2)$ value by re-scaling the deposition time. Obviously the film weight is quite stable and controlled within 3% of target in the presence of the temperature drift throughout the course of a seven-wafer run (except for the last wafer processed at $200^0$C, which shows a relative large discrepancy as seen in the plot of the data error vs. run number (Figure 4.16)). This discrepancy at low processing

temperature is considered due to the wall reaction, which is independent on the processing temperature and will take a larger share in the final mass spectrometry signal as the process reaction on the wafer surface is reduced at the lower deposition temperature. That means not the entire mass spectrometry signal observed shall be related to the W deposition on the wafer and explains why the film weight is less than expected.

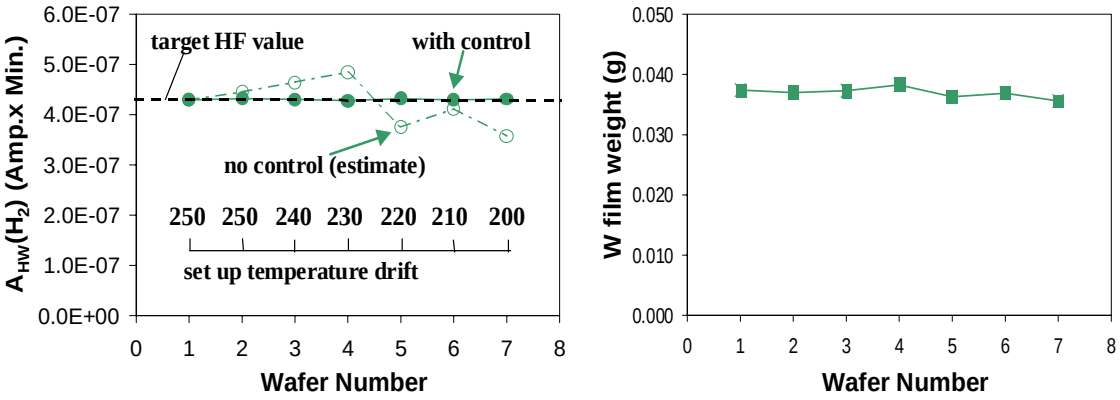


Figure 4.15: $H_2$ signal $A_{HW}(H_2)$ and W film weight vs. run number. The initial run (150 seconds) defines the target $H_2$ value ($A_{HW}(H_2)$) of 4.3E-7 corresponding to a film weight of 0.0375g and the temperature drift of $-10^0$C per run was introduced since the third wafer. The solid data points represent $A_{HW}(H_2)$ obtained with real-time control; the open data points indicate the projected $A_{HW}(H_2)$ without control obtained by re-scaling the deposition time. The squares in the plot on the right show the corresponding film weight.

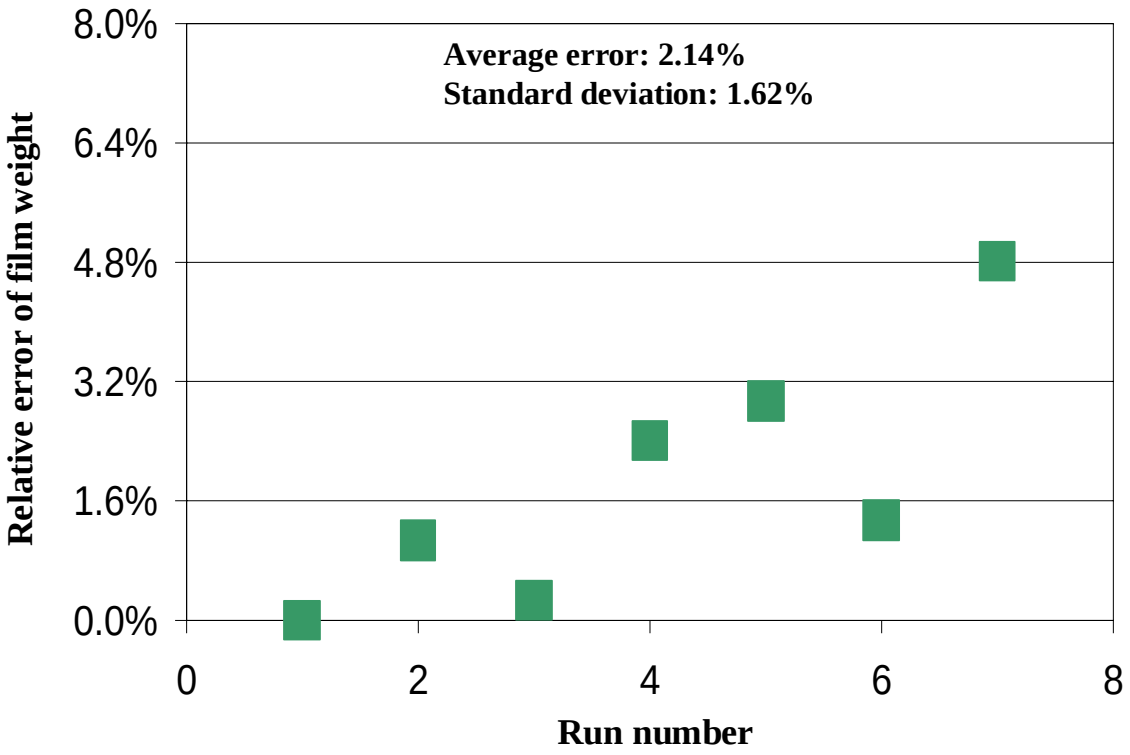


Figure 4.16: Relative error of film Weight vs. run number.

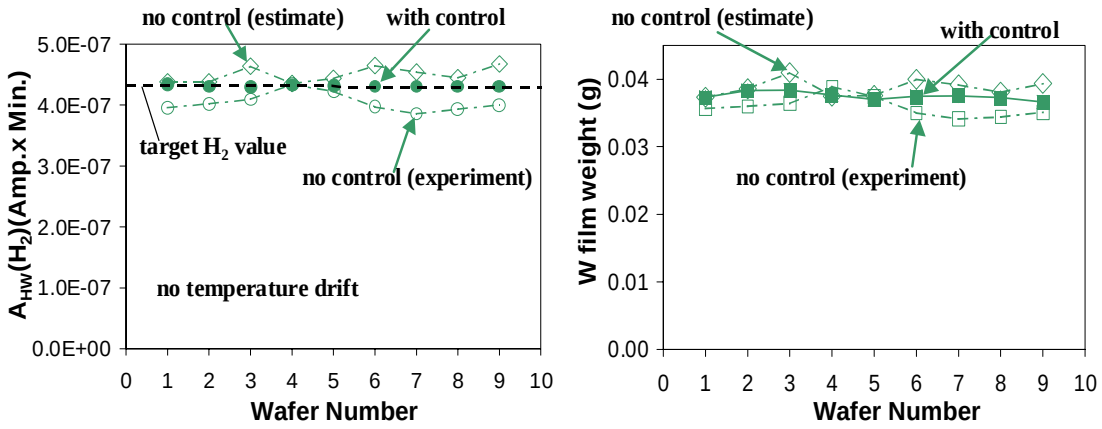


Figure 4.17: W film weight vs. run number. No temperature drift was added. The same target $H_2$ value ($A_{HW}(H_2)$) of 4.3E-7 was used.

It is interesting to note that in Figure 4.15 the projected film weight for the fourth wafer at $230^0$C is the largest suggesting a maximum deposition rate at lower temperature than proceeding wafers. Usually the deposition rate should be smaller at lower deposition temperature. This means that statistical variation between wafers dominates over the intentionally introduced temperature drift. The explanation for this abnormal behavior lies in the different surface morphology of the wafers used for the control experiments. As explained in last chapter, to prevent flaking due to the poor adhesion between the Si wafer and the W film deposited by $SiH_4$ reduction of $WF_6$, W-capped silicon wafers were used in $SiH_4$ reduction W-CVD process. This initial W layer was prepared by $H_2$ reduction process and provides good adhesion between the Si wafer and the succeeding W deposited by $SiH_4$ reduction process. The different processes that these W-capped wafer had undergone before determine that the wafer surface conditions were quite different and therefore maximum deposition rate were observed at $230^0$C instead of $250^0$C. This result delivers a very important message that sensor-based real-time control is capable of handling the random disturbance

during wafer processing. As shown in our case, the mass spectrometry signal tells that for the wafer processed at $230^0$C, a shorter deposition time instead of a longer one that may be expected by most people is proper to keep the film weight at the target. What makes this extremely invaluable is that all the corrections were done even with no clue to the source of the disturbance.

In the right diagram of Figure 4.17, the solid squares represent the film weight obtained with control and the same target of 4.3 E-7 was chosen for the control variable $A_{HW}(H_2)$ . Even though no systematic temperature drift was introduced in this set of experiments, the wide variation of wafer surface conditions offers enough process variation that real-time control can be implemented to correct the variations. The open squares symbolize the measured film weight in the open loop system and a constant deposition time was selected for these wafers. The open diamonds denotes the projected film weight by re-scaling the deposition time. It is very clear from Figure 4.18 that the weight of the film obtained in the open loop system has a much wider distribution. With real-time control, film weights were brought closer to the target. The statistical data for all these processed wafers are listed in Table 4.2. The standard deviation of the film weight was cut down from 0.0015g to 0.0006g after applying real-time end point control. The projected film weight with no control by rescaling the deposition time and the measured film weight for wafers in the open loop system show similar statistic behavior despite the fact that the film weight averages sit on the different sides of the target. This justifies the calculation of the projected film weight by re-scaling the deposition time. However considering the limited number of wafers

involved in this experiment, more experiments may be needed to make the statistic data more meaningful.

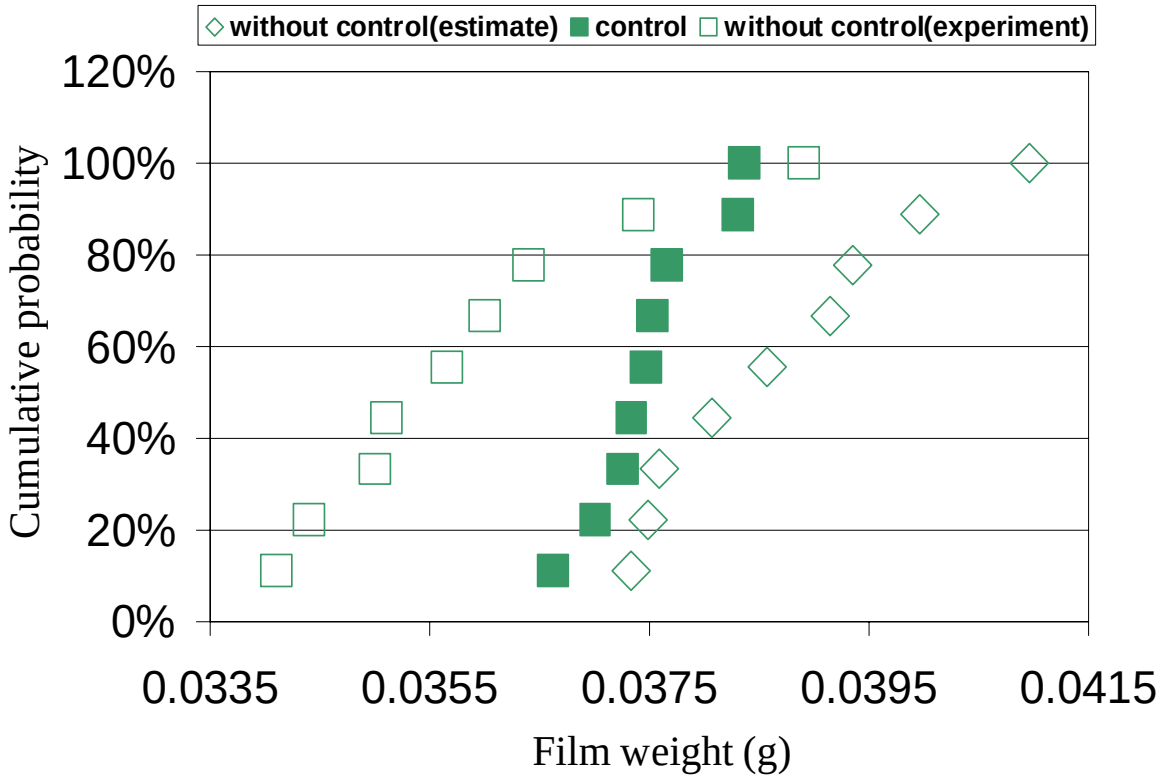


Figure 4.18: Cumulative probability of the film weight.

Table 4.2: The statistical analysis of the control experiment results.

| | With control | Without control (experiment) | Without control (estimate) |
|---|---|---|---|
| Average weight (g) | 0.0375 | 0.0359 | 0.0387 |
| Standard deviation (g) | 0.0006 | 0.0015 | 0.0012 |

### *4.3: Fault Detection*

As explained before, the selective W-CVD process based on a $H_2/WF_6$ mixture is a two-step process, initiated by nucleation of a W seed layer, and followed by steady-state W deposition from $H_2/WF_6$. In our studies of deposition on the Si surface, the nucleation reaction is Si reduction of $WF_6$ (see equations on the next page), consuming a small amount of the Si surface as reactant. Since the process, and hence the nucleation step, is selective, depositing on Si but not on $SiO_2$, the initial deposition can in principle measure whether the starting wafer surface is clean, i.e., oxide-free. Our experiments demonstrated this capability in the time-dependent behavior of the mass spectrometry signal associated with $SiF_4$, the gas phase reaction product of the nucleation reaction.

Here, a fault-trapping algorithm has been developed based on the normalized integration of this $SiF_4$ mass spectrometry signal, so that the resulting surface cleanliness metric (SCM) indicates whether the Si surface was clean. For SCM $\geq$0.7 at 40 sec after process initiation, the surface is considered clean; for SCM$\leq$0.2 at this point, it is considered oxide-covered (not clean), and a fault announcement is issued; and between SCM values of 0.2 and 0.7, a warning is issued.

The implication of this is that inadequate surface cleaning can be detected by mass spectrometry, and in particular during the course of using mass spectrometry as an *in-situ* thickness metrology for run-to-run process control, the goal of this research program. This work might have potential application to blanket W-CVD processes in multilevel interconnects since such process conditions could be approached by going

through the lower pressure regime at sufficient temperature that the initial seed layer growth is selective. It is expected that the traditional selectivity for growth on Si vs. $SiO_2$ may well be repeated in the case of clean vs. oxidized metal at the bottom of contact holes in multilevel interconnects.

### 4.3.1: Detection of $SiO_2$ Covered (Unclean) Wafer Surface.

The process in which the fault-trapping algorithm was established is selective W-CVD process by $H_2$ reduction of $WF_6$ on 4-inch Si wafer. During the nucleation stage, $WF_6$ encounters the clean Si surface and the following three Si reduction reactions take place to deposit layers of W film, forming a seed layer over the surface on which sustained W film growth by $H_2$ reduction of $WF_6$ can continue.

$$2WF_6(g)+3Si(s) \longleftrightarrow 2W(s)+3SiF_4(g)$$

$$WF_6(g)+3Si(s) \longleftrightarrow W(s)+3SiF_2(g)$$

and $$WF_6(g)+2Si(s)+H_2(g) \longleftrightarrow W(s)+2SiF_3H(g)$$

Clearly, the wafer surface condition has a decisive effect on the W film growth: unwanted insulators like $SiO_2$ in the contact window may retard or prevent the nucleation step and the following film growth. Consequently a clean wafer surface, free of $SiO_2$, is needed, which requires removal of native $SiO_2$ from the wafer surface by HF dip before sending wafer into reactor for deposition. We can monitor the wafer surface condition during the nucleation stage by monitoring the mass spectrometry signal for $SiF_4$, a gaseous product of the nucleation reaction. Abnormal $SiF_4$ signal (shape, intensity, or dynamic behavior) may indicate undesirable wafer surface condition, which allows us to come up with an algorithm for fault detection based on

the mass spectrometry signal. Figure 3.6 shows the typical $SiF_3^+$ signal (85 amu, the main ionization fragment of $SiF_4$, a gaseous product of Si reduction of $WF_6$) in W-CVD process carried out on a clean wafer, free of $SiO_2$. The signal is recorded using the direct sampling system with a time resolution of about 0.5 second.

#### 4.3.1.1 Analyzing the $SiF_3^+$ mass spectrometry signal

To quantitatively analyze the $SiF_3^+$ signal for fault trapping algorithm development, integration of $SiF_3^+$ signals over a certain length of time (180 seconds. in our case) has been carried out. The results are plotted in Figure 4.19. In the light of considerable variation of mass spectrometry sensitivity from time to time, it is desirable to normalize the integration results so that a more accurate and meaningful comparison can be made among data recorded on different days. The normalized integration results are depicted in the large graph of Figure 4.20. The main features of the curves are retained except that now all the curves are normalized to end at 100%. The normalized integration value at the time of 40 sec. indicates that the seven curves fall into three different categories representing three different wafer surface conditions, as indicated in Table 4.3.

Table 4.3: Fault trapping algorithm for the selected mechanism: Monitoring the wafer surface status by monitoring the mass spectrometry signal for $SiF_3^+$, Which is the main ionization fragment of $SiF_4$, a gaseous product of the nucleation reaction on wafer surface.

| Curve # | Curve 1 and 2 | Curve 3 and 4 | Curve 5, 6 and 7 |
|---|---|---|---|
| Normalized integration value | $\frac{\int_0^{40} S_{SiF_3}\,dt}{\int_0^{180} S_{SiF_3}\,dt} \le 20\%$ | $20\% \le \frac{\int_0^{40} S_{SiF_3}\,dt}{\int_0^{180} S_{SiF_3}\,dt} \le 70\%$ | $\frac{\int_0^{40} S_{SiF_3}\,dt}{\int_0^{180} S_{SiF_3}\,dt} \ge 70\%$ |
| $SiF_3$ mass spectrometry signal | Delayed broad peak or even double-peak shape | Somewhat delayed and relatively broad. | Narrow and sharp peak |
| Wafer surface status | Oxide-(contaminant-covered) Si surface | Partially contaminated surface | Clean wafer surface |
| Response | Fault detected; error message generated. | Possible fault; warning or caution message generated. | No fault; no action taken. |

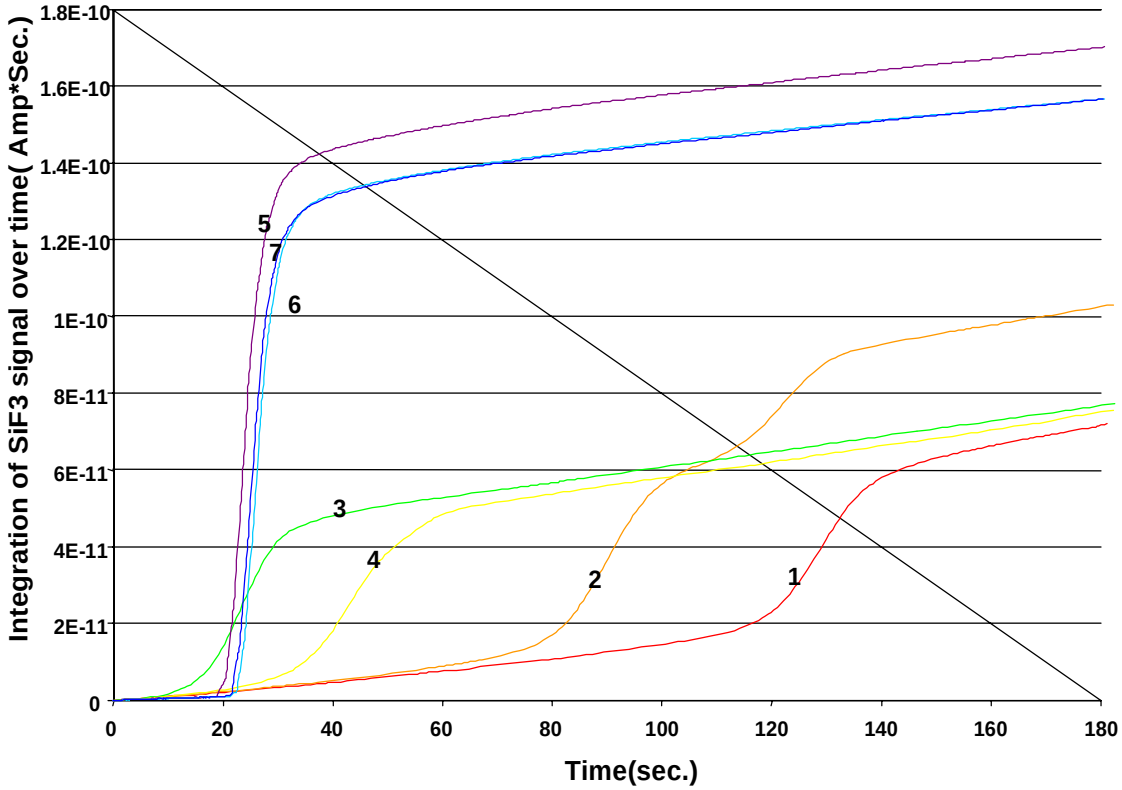


Figure 4.19: Integration of $SiF_3^+$ signals over time. The process conditions are identical (temperature: $450^0$C, pressure: 0.5Torr), while the wafer surface conditions are different.

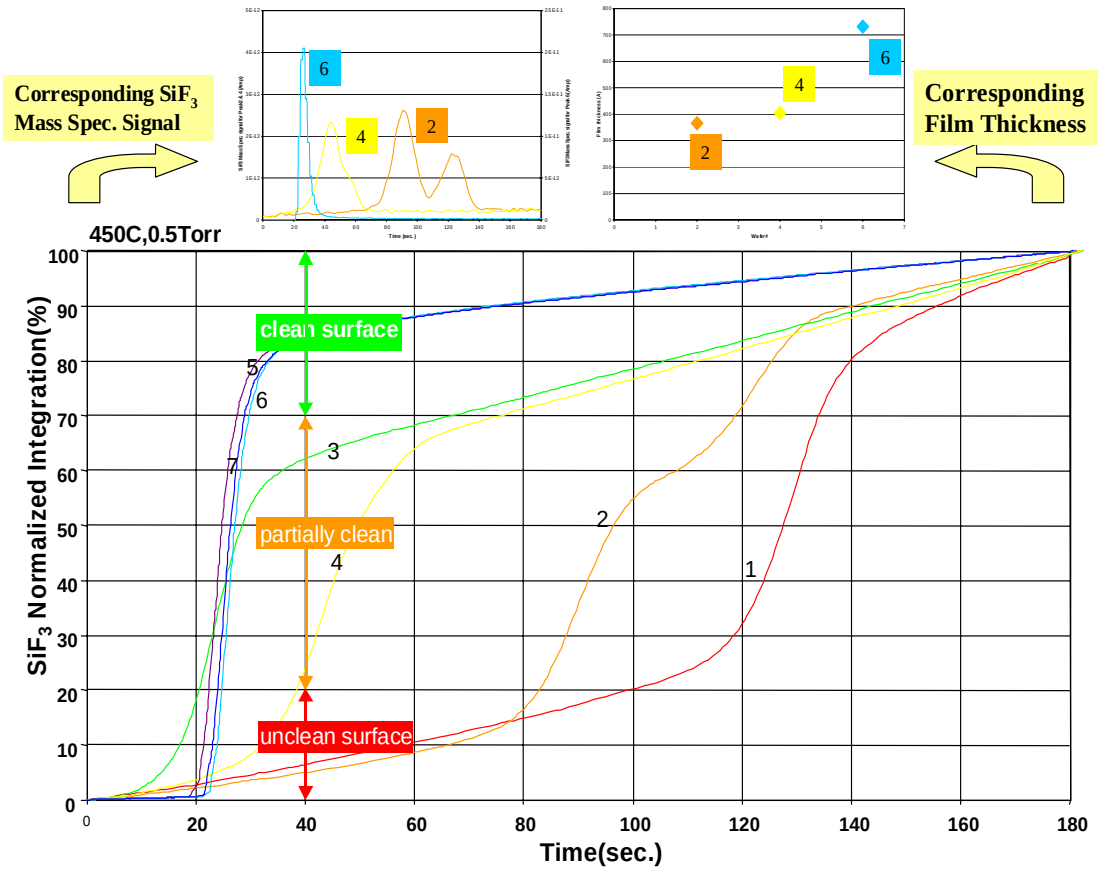


Figure 4.20: The small graph on the left shows the variation of $SiF_3^+$ Mass spectrometry signal during the W-CVD process using $H_2/WF_6$ mixture ($450^0$C, 0.5Torr). The small graph on the right depicts the corresponding film thickness. The large graph indicates the normalized integration of $SiF_3^+$ signal over time. The silicon wafer surface status can be determined on the normalized integration of $SiF_3^+$ signal at the time of 40 seconds as depicted in the diagram.

#### 4.3.1.2 Algorithm development

Table 4.3 illustrates the fault-trapping algorithm. A large normalized integration value (≥70%) at the time of 40 sec. implies a clean wafer surface. A small value (≤20%) indicates an unclean (typically oxide-contaminated) wafer surface, which will result in a low growth rate and non-uniform film. The small graph in the upper left of Figure 4.20 shows the three different types of $SiF_3^+$ mass spectrometry signals corresponding to the three different surface conditions. The blue line (#6) indicates that on the clean wafer surface, the rapid but self-limiting Si -reduction reaction produces a sharp and narrow peak for $SiF_3^+$ shortly (about 20 sec.) after the reactants are introduced into the reactor. However, on the oxide-contaminated surface (#2), the nucleation reaction is retarded. That is why the $SiF_3^+$ signal remains at the low level for an extended period of time (more than 40 sec.) and then starts to climb up. Also worthy of mention is that a secondary peak is observed following the first delayed peak, suggesting delayed nucleation where the surface was originally covered with the $SiO_2$. The intermediate situation (#4) shows a broader peak than that for the clean surface (#6), but not a double peak.

The film thickness data depicted in the small graph in the upper right of Figure 4.20 confirms our analysis above. From the diagram, we can see that after 6 minutes process, the film in #6 (clean surface) is much thicker than the films obtained in processes #2 and #4.

#### 4.3.1.3 Algorithm Implementation

Transpectorview has previously been modified to facilitate integration of a specific mass spectrometry signal at the same time as the signal is being recorded.

The algorithm discussed above can be fairly easily implemented by further modification of the program. After this is finished, the program will be able to generate an error or warning message to the operator during the process whenever the $SiF_3^+$ signal indicates a contaminated wafer is being processed. Further work will attempt to demonstrate that improperly cleaned wafers can be detected as faults during the course of using mass spectrometry based metrology for run-to-run control.

In the construction of the fault-trapping algorithm here, the normalized integration value of $SiF_3^+$ at the time of 40 seconds after the beginning of the process is used as the criteria to determine the wafer surface state. Of course, the process time to an effective measurement point will depend on the specific process parameters. For different process conditions (e.g., temperature or pressure), integration values at a different time should be chosen in the fault-trapping algorithm. A dynamic simulator of the nucleation step will help us to determine the right timing for different process conditions.

# 5. Discussion about Real-time Chemical Sensing Using Mass Spectrometry

## *5.1: Process Drift vs. Sensor Drift [[lviii]].*

Process drift and sensor drift were not uncommon in chemical sensing in a multiple component chemical reaction system such as W-CVD process using mass spectrometry. Usually an observed signal drift can be a result of either a either a process drift or sensor drift. Since it is extremely important to have stable measurement in order to develop film thickness metrology based on the mass spectrometry signals of different species in the chemical system, it is necessary to distinguish between process drift and sensor drift, which usually is quite tricky. Only then we can find out some way to prevent them from happening or minimize their effect on sensor-based metrology.

### 5.1.1: Process Drift

Process drift can happen in many different ways especially in a chemical reaction system using reactive reaction precursors. Listed below is a summary of the most common reasons for process drift.

1. Wall reactions including the surface chemical reaction and condensation of low equilibrium vapor pressure gaseous precursors on the wall
2. Plugged or partially plugged pin hole orifice between the sample gas source and the ion source.

3. Electron induced desorption (EID) [lix, lx] and ion molecule reaction involving both ions and molecules inside the ion source of mass spectrometry.

It should be pointed out all the above chemical effects will be quite severe if the gases involved are chemically active, which is exactly the case with W-CVD process from a mixture of either $H_2/WF_6$ or $SiH_4/WF_6$. In W-CVD process, reactant $WF_6$ and reaction product HF readily react with the impurities such as water vapor inside the reactor and condense on the wall. Therefore $WF_XO_Y$, e.g. $WF_3O$ generation, was detected as a product of the chemical reaction between $WF_6$ and $H_2O/O_2$. Another interesting phenomenon was that the $WF_5^+$ signal was observed to drift up and $WF_3O^+$ drifted down during the conditioning cycle prior to the deposition (see Figure 5.1). That is because less $WF_6$ would condense on the wall or be consumed in the reaction with $H_2O/O_2$ as the wall surface of the reactor approached the equilibrium status and most of the impurities were removed.

To minimize the effect of wall reaction on the chemical sensing, the sampling system shall be brought as close to the reactor as possible, for this will eliminate most of the wall. Baking the system and a conditioning cycle will also help to solve this problem to some extent. Baking the system desorbs different species from the wall and reduce further adsorption, while a conditioning cycle can equilibrate the wall surface before serious measurement is made during wafer processing.

The tens of micron-size pinhole orifice used for pressure reduction is another potential source of process drift. As shown in the sampling system configuration

diagram in chapter 3, the orifice in our system is only 38 to 300 μm in diameter, which can become plugged and result in a decrease of the pressure in the close ion source. So the orifice need be checked regularly to make sure that it is clean and not clogged.

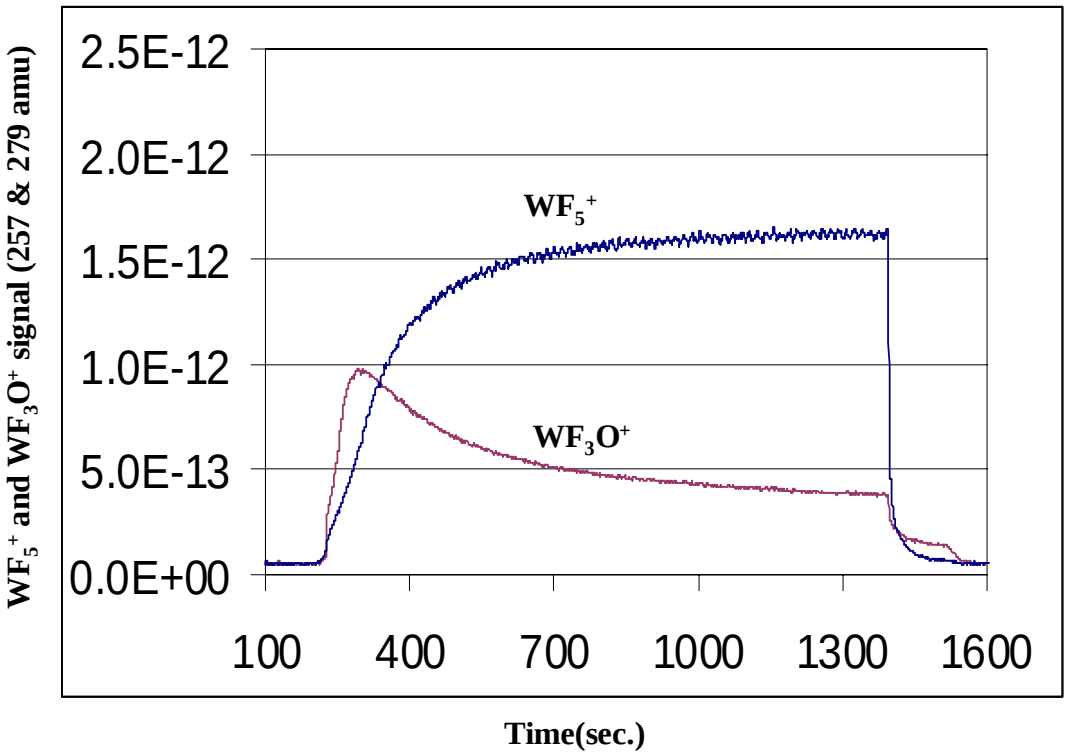


Figure 5.1: WF5+ and WF3O+ mass spectrometry signals during the conditioning cycle.

EID happens inside the ionizer of mass spectrometry. As we know that the inner surface of the ion source is covered with adsorbed gases. Electron bombardment of the surface can result in desorption of the gases in the form of ions and/or neutrals. These ions may leave the ionizer and enter the analyzer along with the ionized gas molecules, which produces errors in the partial pressure analysis. The neutrals may also be ionized by subsequent electron bombardment and make an unwanted contribution to the detected ion signal as well. Since different gas species show quite different EID behavior, it is not easy to determine what and how much effect EID will

have on a particular pressure analysis. To relieve the interference of EID with chemical sensing, degas capability is commonly in mass spec. design: a higher voltage is applied to the filament, causing increased electron bombardment of the chamber and therefore increased outgassing in order to remove the desorbed species.

Similar to EID, the ion molecule reactions between ions and molecules in the ionizer will affect the chemical sensing too, contributing to the signal that can not be easily related to the partial pressures of the gases in the system.

What is implied in the discussion above is that the chemical sensing is determined by not only the chemistry in the reactor but also the previous process history and the reactions inside the sensor.

### 5.1.2: Sensitivity drift

After screening out the possibility of process drift, the sensitivity drift can be considered and investigated for the observed signal change. Most likely reasons include but are not limited to:

1. Degrading of the electron multiplier (EM) (only if EM mode is applied in measurement)
2. Deposition of electrically conductive films on critical insulator surfaced.
3. Deposition of insulator films on critical surfaces that must remain conductive to perform properly.

EM is made of a special type of glass and it will degrade gradually after a long time exposure to high pressure especially corrosive fluorine containing chemical

species. The EM gain shall be checked frequently by measuring a given peak in both the Faraday cup and EM modes. The ratio of these two currents tells the EM gain. Reducing the working pressure and exposure time will help to slow down the degradation of the EM and prolong its lifetime.

The second problem is the deposition of conductive films on critical insulators due to the thermal reaction inside the ionizer. The best way to check it is to make resistance measurements on the sensors itself when the mass spectrometry is still under vacuum. The resistance between the anode pin and filament pins should exceed 10 MegOhems. A lower resistance will result in excessive leakage current between the anode and filament, which will mimic at least part of the electron emission current, resulting in decreased sensitivity. Insulating deposits formed on the inside surface of the anode as a result of the reaction between the reactive reactants and the impurities like $O_2$/$H_2O$ inside the ionizer can also cause sensitivity degradation. That is because the insulating surface will charge up with electrons, decreasing the potential at which the gases were ionized, such that they did not have sufficient kinetic energy to pass the quadrupole mass filter. Minimizing the oxygen or water vapor in the mass spectrometry will greatly reduce the insulating deposits.

Abrupt change in the signal like the one shown in Figure 5.2 has been observed in our research. It is considered that the misbehavior of the ion source is responsible for that. Most often it could be taken as the forewarning of final emission failure and a change of the ion source is necessary soon.

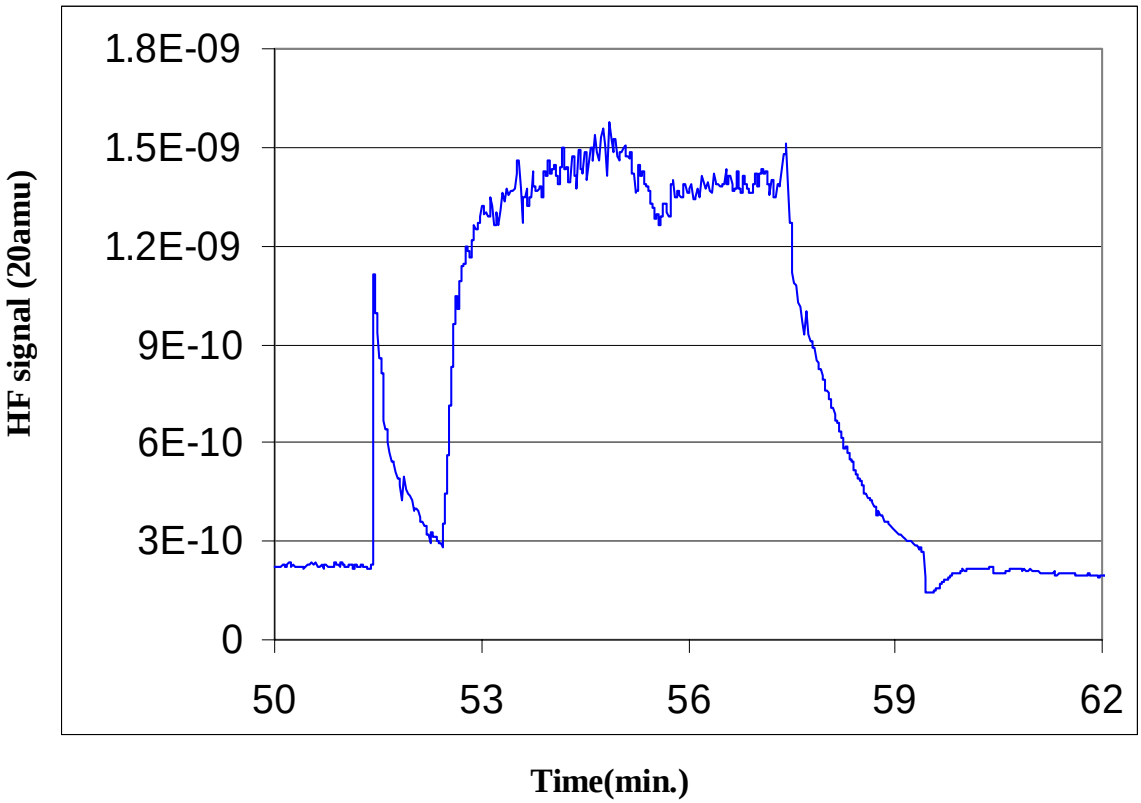


Figure 5.2: HF mass spectrometry signal showing the abrupt change due to sensor misbehavior.

Knowing the different sources of sensor drift and process drift, we will be able to distinguish these two types of drift. Usually a careful analysis of all the mass spectrometry signals will help to reveal the true reason for the signal drift. Generally speaking, the process drift will be observed in all the signals but may result in opposite behavior for generation and depletion signals, while sensor drift will cause the signal drift in the same direction.

### *5.2 Metrology signal choice*

In principle product generation signal provides a better measurement than reactant depletion because of the large background inherent to depletion signal especially when conversion rate is low. However this work shows that both the product generation and reactant depletion signals can be candidates for thickness metrology development. This research suggests that the choice of a signal on which to base thickness metrology is dependent on the specific process. For example, in the multi-component reaction system, the choice of reactant stoichiometry is determined by the chemical mechanism and the application. Typically an overabundance of one reactant is required, so that the transport of the other is at least in part rate-limiting. This implies that the most abundant species may not be suitable for measurement of reactant depletion for film thickness metrology, because it has the lowest conversion rate.

Another factor that shall also be taken into account when selecting the right signal is the chemistry of different candidates. Since the wall reaction between the reactive species and impurities in the system can contribute to the same reactant depletion and occasionally generate the same products as the process reaction on the wafer, some reactive species may not be a good choice for metrology either. In $H_2$ reduction W-CVD process, the attempts to achieve film thickness metrology from HF succeeded only after extensive investigations on the effects of the wall conditioning and the process conditions. A long conditioning cycle and baking of the system was implemented to minimize the condensation and reaction on the wall. $H_2$ has far less problematic wall chemistry, which makes $H_2$ depletion-based metrology quite

favorable as compared with $WF_6$ signal. However the extremely poor conversion rate of the process limits the accuracy of the metrology results from $H_2$ significantly.

# 6. Conclusions.

The accomplishments of this research, which are covered in the thesis and summarized below demonstrate the value of applying *in-situ* chemical sensing in complex manufacturing process systems for sensor-based metrology and advanced process control.

## 6.1: Real-time *in-situ* chemical sensing using mass spectrometry

A direct mass spectrometry sampling system has been successfully implemented for real-time *in-situ* chemical sensing in W-CVD process from mixtures of $H_2/WF_6$ and $SiH_4/WF_6$ on Ulvac-ERA 1000 cluster tool. A data acquisition system was built with the data acquisition board running on LabView¤ platform to facilitate sensor integration. Mass spectrometry signals of product generation and reactant depletion were captured synchronously and revealed important information regarding process chemistry and equipment dynamics. The time integration of mass spectrometry signals was shown to provide *in-situ* measurement of the W film thickness in accordance with the stoichiometry of the process reaction. The subtleties picked up by the mass spectrometry, such as the Si reduction reaction during the nucleation stage of the $H_2$ reduction process enabled us to develop fault-trapping strategies.

## 6.2: Sensor-based W film thickness metrology.

In $H_2$ reduction process, our attempts to develop mass spectrometry-based W film thickness metrology posed various challenges, among which are very poor

reactant conversion rate of about 3-4%, severe wall reactions and ion molecule reactions inside the ionizer, and occasional sensor drift. In spite of all these difficulties, metrology results from HF signal with an uncertainty of around 7% (16% from $H_2$ signal) were accomplished after extensive experimental refinements and major reconfiguration of the sensor sampling approach, particularly the development of a direct gas sampling method which sampled gases at the reactor rather than downstream near the process pumps. A conditioning cycle with mixture of $H_2/WF_6$ was incorporated before wafer processing and played a key role in equilibrating the wall surface and thus reducing the effect of wall reaction on chemical sensing.

Our experience suggests that the metrology accuracy in $H_2$ reduction process is primarily limited by the low conversion rate. Therefore we initiated the $SiH_4$ reduction process in attempts to enhance the utilization of the reactants. The benefit of high conversion rates for *in-situ* metrology is profound, allowing good signal/noise in the dynamic process monitoring. By increasing the reactant conversion rate by >5X to about 20% conversion, we have achieved thickness metrology using the $H_2$ reaction product signal with an error less than 2%. Furthermore, the much higher conversion rate present in the $SiH_4$ reduction process clearly enables the omission of the nonproductive unheated wafer cycle required in the $H_2$ reduction process for HF signal background measurement. This brings mass spectrometer-based metrology into a stage that is viable for application in manufacturing.

## 6.3: Sensor-based W film thickness process control.

It has been demonstrated that in our experiments that wafer state metrology based on *in-situ* mass spectrometry provides a basis for effective process control. Two different strategies were applied: run-to-run control in $H_2$ reduction process; real-time end point control in $SiH_4$ reduction process.

In $H_2$ reduction process, two static linear models derived from metrology results based on HF signal were employed to drive the robust IMC run-to-run control algorithm for W film thickness control. To demonstrate the implementation of this sensor-based run-to-run process controller, a temperature drift of $-5^0$C/wafer was deliberately introduced, which may cause W film thickness declining by 40% off the target value after a 10-wafer run in the open loop system. The run-to-run controller, capable of handling systematic process drift like the introduced temperature drift, was used to maintain the HF signal at target by adjusting the deposition time. The resulting film thickness was controlled within 10% of the target value, which is comparable to the accuracy of the metrology results.

In $SiH_4$ reduction process, mass spectrometry showed the capability of supporting real-time end point control. Here the $H_2$ product generation signal was monitored and the process was terminated when the time integration of $H_2$ signal reached the target. By controlling the integrated $H_2$ signal in real-time, the W film thickness was successfully controlled within 3% of the target in the presence of random disturbances, some of which were associated with varying initial various wafer surface conditions. The film weights showed a much smaller deviation of 0.0006g as compared to around 0.0015g obtained with no control. Such random

disturbance can not be controlled by run-to-run control strategies, but indeed they require real-time control.

## 6.4: Fault detection using mass spectrometry.

A fault-trapping algorithm using mass spectrometry has been constructed to detect the improperly cleaned wafer surface in $H_2$ reduction process. During the nucleation stage of $H_2$ reduction process, the seed W layer is deposited by Si reduction selectively on Si surface but not on insulator such as $SiO_2$. The surface cleanliness metric (SCM) based on the normalized integration of $SiF_4$ (gaseous product of Si reduction process during the nucleation stage) mass spectrometry signal indicates whether the Si surface was clean. For SCM $\geq$0.7 at 40 sec after process initiation, the surface is considered clean and the $SiF_4$ signal shows a sharp and narrow peak. For SCM$\leq$0.2 at this point, it is considered oxide-covered (not clean). The nucleation of W film by Si reduction will be retarded where the oxide remains so that the $SiF_4$ signal shows delayed peak or a twin-peak feature and a fault announcement is issued. For SCM values lying between 0.2 and 0.7, a warning is issued. This work shows that mass spectrometry have potential application in fault detection during the course of using mass spectrometry as *in-situ* film thickness metrology for process control in CVD process.

# 7. Future Work.

Significant achievements as stated above demonstrate the value of real-time chemical sensing using mass spectrometry, However to make this technique ready for real semiconductor manufacturing, several more issues should be addressed.

## *7.1: Blanket W-CVD.*

As we discussed before that much better metrology results would be available with higher reactants conversion rate. $H_2$ reduction Blanket W-CVD at 40-100 torr is today's industrial standard which gives a conversion rate of 40-50%. Such a high conversion rate should be very desirable for sensor-based thickness metrology.

Modification to the Ulvac-ERA1000 cluster tool is undergoing to accommodate blanket W-CVD at higher pressure. The modification includes replacing the lamp-heating with substrate heating and adding a separate pressure control system that is capable of maintaining the pressure in the reactor up to 100 torr. We expect $H_2$ reduction blanket W-CVD process at high pressure will lead to sensor-based thickness metrology as good as $SiH_4$ reduction process does.

## *7.2: Development of wafer state metrology on patterned wafer.*

It needs be pointed out that all the processes in this research were carried out on 4" Si or W-capped Si wafers with no patterns. However on the real wafers used in IC fabrication, the actual area of the contact windows is no more than 10-20% of the total wafer surface, the rest of which is covered by the insulator or barrier layer. As a result of the reduced reaction site, the intensity of the mass spectrometry signal will be

cut down significantly under the same processing conditions, which may affect the accuracy of the metrology result and process.

In high aspect ratio via filling, another equally important factor besides the film thickness is the film conformality. It would be important to seek ways to determine film conformality as a mass spectrometry-based metrology. However this requires a deep understanding of the relation between mass spectrometry signals and the film conformality, perhaps along with invention.

### *7.3: Development of in-situ Calibration System for Mass Spectrometry Sensitivity Calibration.*

Mass spectrometry must provide quantitative measurement of chemical species for wafer state metrology. Sensitivity calibration need be practiced regularly to ensure the validity of the mass spectrometry signals. The sensitivity calibration should be carried out *in-situ* without consuming the valuable process time.

To provide *in-situ* sensitivity calibration, an *in-situ* calibration system as shown in Figure 7.1 has been constructed. To start calibration the valve isolating the calibration system from mass spectrometer will admit calibration gas e.g. $H_2$ or Ar into the sampling system. The amount of gas delivered is determined by the pressure inside the calibration system where a Spinning Rotary Gauge is employed to measure the pressure. Knowing the pressure, the sensitivity of the sensor can be easily calculated out based on equation 2-22 and we will be able to compare data on different days even in the presence of sensitivity drift by normalizing the signal according to the sensitivity (see Figure 7.2). Here a large gas reservoir is selected in order to maintain

the pressure in the calibration system stable during the calibration procedure. Further work is needed to develop and qualify the sensor calibration methodology.

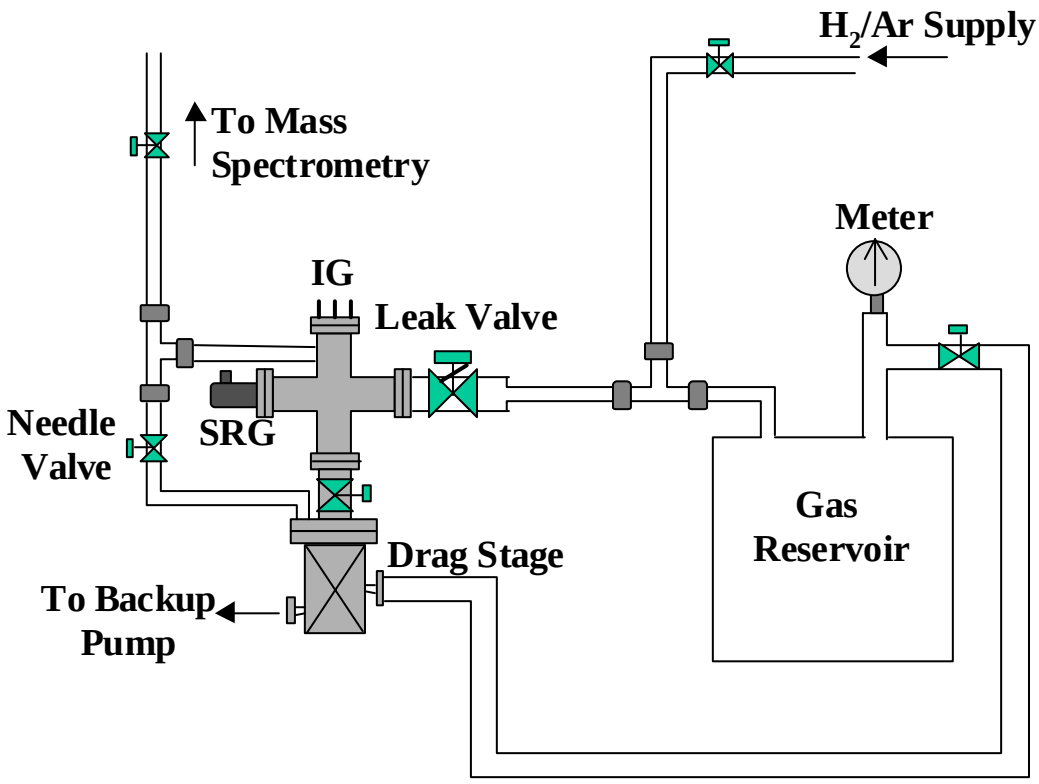


Figure 7.1: The schematic of *in-situ* mass spectrometer sensitivity calibration system.

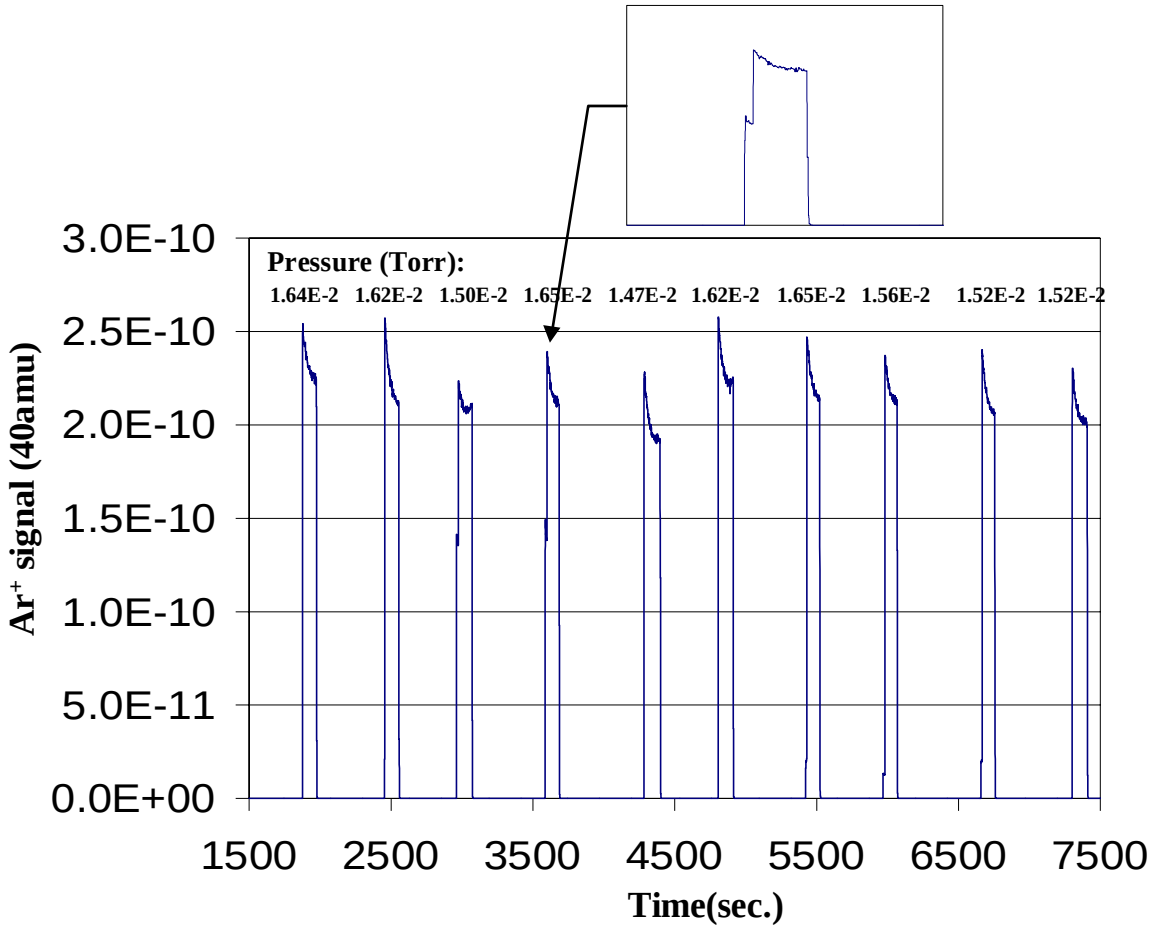


Figure 7.2: Mass spectrometry signal of $Ar^+$(40amu) and corresponding pressure inside calibration system.

### *7.4: Incorporation of Different Types of Sensors to Enable Better Understanding of Process and Sensor Study as Well.*

It is a common practice to implement multiple sensors on one tool. In our research, an acoustic sensor Composer™ was deployed along with mass spectrometer for chemical sensing as illustrated in Figure 7.3. Incorporation of multiple sensors proves beneficial by offering invaluable information to help us understand the chemical process and the sensor itself. Take the issue of sensor drift and process drift

as an example, process drift shall be observed in the signals of all the sensors, while sensor drift may only affect one particular sensor. Therefore that will give us some

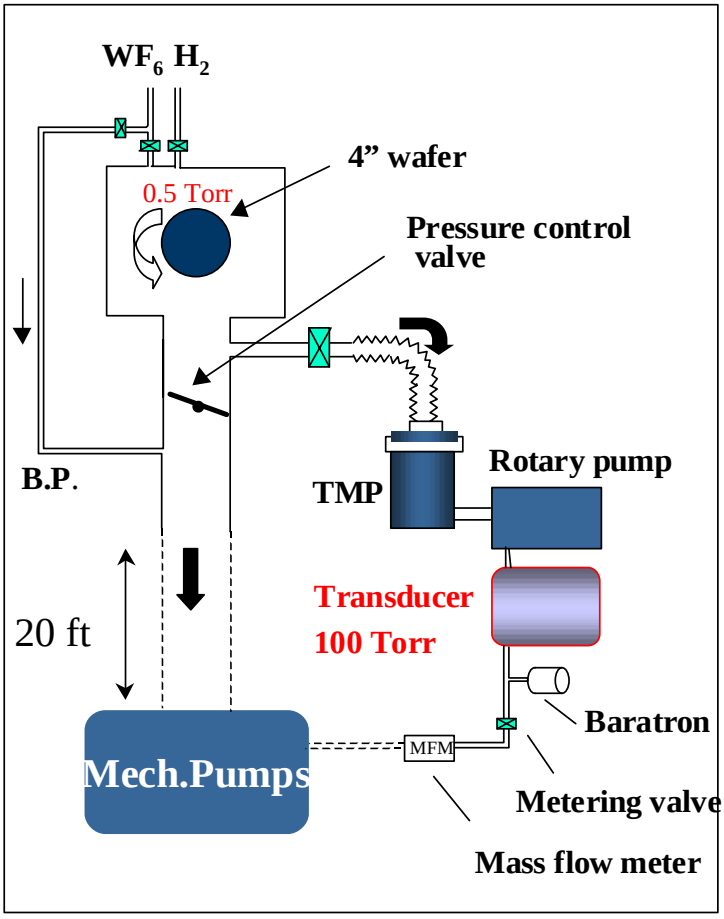


Figure 7.3: Configuration of Composer™ sampling system

clues to the true reason of an observed signal drift. However each of the different types of sensors implemented has its own characteristic, which makes the incorporation of various sensors on one tool not trivial at all. Some sensors work properly only under high vacuum, others may need a configuration as shown in Figure 7.3 to bring up the pressure in order for them to get reliable measurement. Some

sensors can be applied virtually to any process, while some can only work under a plasma environment.

A. APPENDIX CIS SAMPLING SYSTEM DESIGN

The process pressure inside the reactor is 0.5 Torr in $H_2$ reduction process. The close ion source sampling system is shown below with the conductance of the orifices and close ion source in Table A.1.

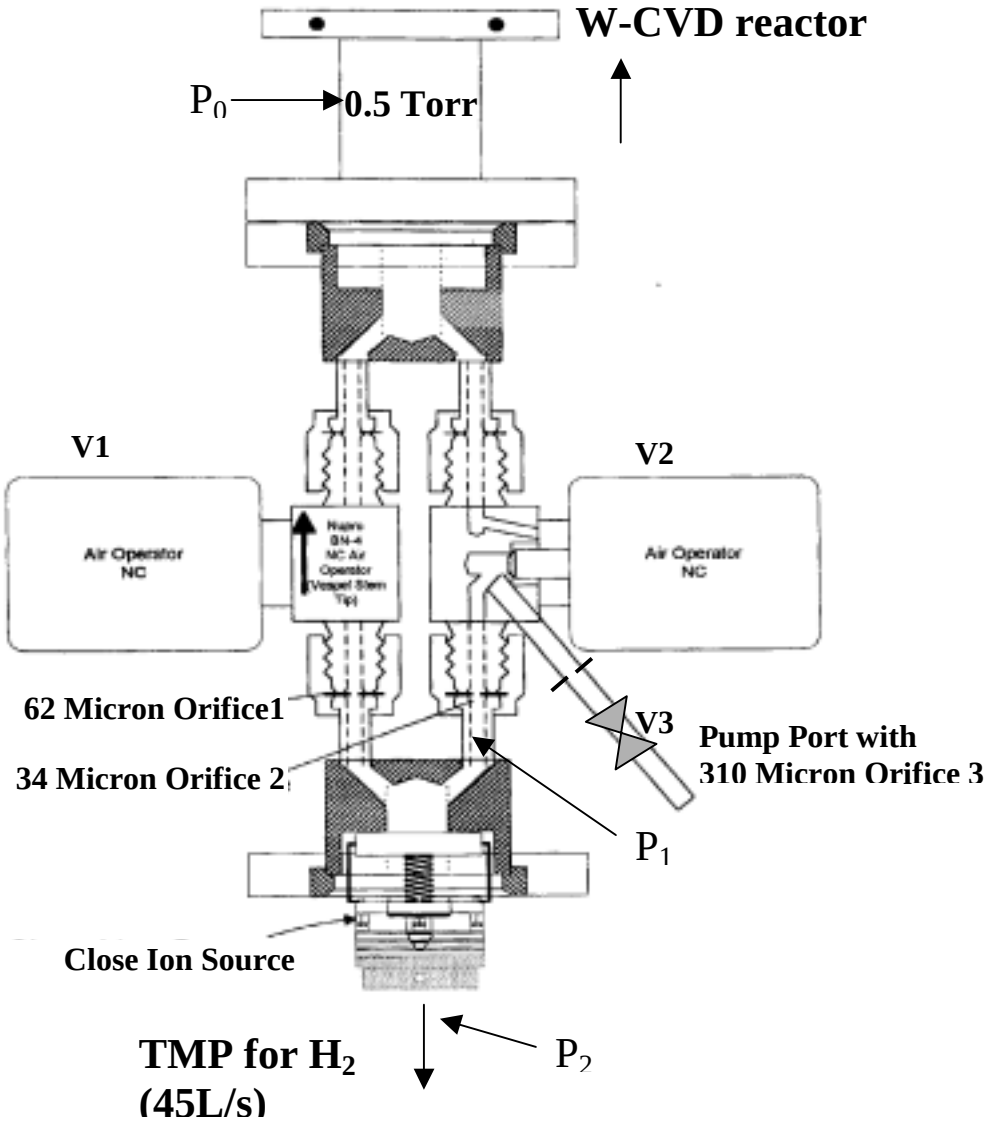

Figure A.1: CIS sampling system design.

Table A.1: Conductance of the orifices and pumping speed of the TMP.

| | Conductance or pump speed (L/s) |
|---|---|
| Orifice 1 | 5.68E-04 |
| Orifice 2 | 1.77E-02 |
| Orifice 3 | 1.31E-04 |
| CIS | 0.4 |
| TMP | 45 |

The pressure reduction of this sampling system can be calculated as follows:

$$P_1 = P_0 \times \frac{1.31E-4}{0.4} = 0.5 \times \frac{1.31E-4}{0.4} = 1.64E-4(Torr)$$

$$P_2 \times PS = P_1 \times 0.4 + P_f \times \frac{PS}{CR}$$

- $P_2 \times 45 = 1.64\,E-4 \times 0.4 + 5\,E-2 \times \frac{45}{3\,E\,5}$
- $P_2 = 1.63\,E-6\,(Torr)$

Where $P_0$ (=0.5 Torr) is the processing pressure in the reactor, $P_1$ denotes the pressure inside the close ion source, and $P_2$ represents the pressure in the mass spectrometry chamber. PS and CR are the pumping speed and compress ration of the TMP respectively. The foreline pressure is 5E-2 Torr. The results indicate that $P_2$=1.63E-6 Torr, which is close to our observation of 2E-6 Torr.

[i] E. J. Lerner. Can anything stop the transistor? The Industrial Physicist. Pages: 18-21, June,2000

[ii] H. P. Tseng and R. Jansen, Cleanroom Technology, ULSI Technology, edited by C. Y. Chang and S. M. Sze, 1996, McGraw-Hill.

[iii] Overall Roadmap Technology Characteristics & Glossary. International Technology Roadmap for Semiconductors 1999 Edition. Page: 17, SIA 1999.

[iv] L. L. Tedder, G. W. Rubloff, I. Shareef, M. Anderle, D. H. Kim, and G. N. Parsons. Real-time process and product diagnostics in rapid thermal chemical vapor deposition using *in-situ* mass spectrometric sampling. J. Vac. Sci. Technol. B 13(4), pages: 1924-1927, 1995.

[v] K. Huber, T. Desanti, and S. Felker. Increased process stability for CVD tungsten via *in-situ* particle monitoring and upstream process control. A. Iturralde and T. H. Lin,editors, Process, Equipment, and Materials Control in Integrated Circuit Manufacturing II, Proceedings of SPIE , volume 2876, pages 241-249, Austin 1996.

[vi] R. Iscoff. Semiconductor International. August, 69, 1994.

[vii] L. L. Tedder, G. W. Rubloff, B. F. Cohaghan, and G. N. Parsons. Dynamic rate and thickness metrology during poly-Si rapid thermal chemical vapor deposition from SiH4 using real-time *in-situ* mass soectrometry. J. Vac. Sci. Technol. A 14(2), Pages: 267-270, 1996.

[viii] X. Li, M. Schaepkens, G. S. Oehrlein, R. E. Ellefson, L. C. Frees, N. Mueller, and N. Korner. Mass spectrometric measurements on inductively coupled fluorocarbon plasmas: Positive ions, radicals and endpoint detection. J. Vac. Sci. Technol. A17(5), pages:2438-2446, 1999.

[ix] T. Gougousi, Y. Xu, and G. W. Rubloff, Process Diagnose and Mass Spectrometry-Based Metrology in W-CVD Process, J. Vac. Sci. Technol. B 18(3),2000.

[x] L. Peters Residual gas analysis: the use of 300 mm processing will determine whether residual gas analyzers become an essential process monitor or just another diagnostic tool. Semiconductor International, pages: 94-101, October, 1997.

[xi] Executive Summary. International Technology Roadmap for Semiconductors 1999 Edition. Page: 10, SIA, 1999.

[xii] R. J. Bunkofske. Using real-time process control to enhance performance and improve yield learning. Micro. Pages: 49-55, February, 2000.

[xiii] A. C. Diebold. Overview of metrology requirements based on the 1994 national technology roadmap for semiconductors. Proceedings of the Sixth Annual SEMNEEE Advanced Semiconductor Manufacturing Conference and Workshop, Pages: 50-60, Nov. 13-15, 1995. Cambridge, MA.

[xiv] Metrology. International Technology Roadmap for Semiconductors 1999 Edition. Page: 308, SIA, 1999.

[xv]. A. C. Adams. Dielectric and polysilicon film deposition. VLSI Technology, Editor S. M. Sze, McGraw-Hill , New York, 1983.

[xvi] H.C. Cheng. Dielectric and polysilicon film deposition. ULSI Technology, Editor C.Y. Chang and S.M. Sze. McGraw-Hill , New York, 1996.

[xvii] Interconnect. International Technology Roadmap for Semiconductors 1999 Edition. Page: 166, SIA 1999.

[xviii] R. Liu. Metallization. ULSI Technology, Editor C.Y. Chang and S.M. Sze. McGraw-Hill , New York, 1996.

[xix] P.J. Ireland. High aspect ratio contacts: A review of the current tungsten plug process. Thin Solid Films, 304, pages:1-12, 1997.

[xx] M.L. Yu, B.N. Eldridge, and R.V. Joshi. Tungsten and other Refractory Metals for VLSI Applications III, Editor V.A. Wells, pages: 75-81, Materials Research Society, Pittsburgh, PA, 1988

[xxi] G.J. Leusink, C.R. Kleihin, T.G.M. Oosterlaken, G.C.A.M. Janssen, and S. Radelaar. J. Appl. Phys. 72 , Pages:490, 1992

[xxii] P.A.C. Groenen, J.G.A. Holscher, and H.H. Brongersma. Appl. Surf. Sci. 53, page 30,1991.

[xxiii] P.A.C. Groenen, J.G.A. Holscher, H.H. Brongersma. Mechanism of the reaction of WF6 and Si. Appl. Surf. Sci. 78, pages: 123-132, 1994

[xxiv] E.K. Broadbent and C.L. Ramiller. J. Electrochem. Soc. 131, page: 1427, 1984.

[xxv] C.M. McConica and K. Krishnamani. J. Electrochem. Soc. 133, page:2542, 1986.

[xxvi] Y. Pauleau and Ph. Lami. J. Electrochem. Soc. 132, page:2779,1985.

[xxvii] R. Arora and R. Polland. J. Electrochem. Soc. 138, page: 1523, 1991.

[xxviii] A. Hasper, J. Holleman, J. Middlehoek, C.R. Kleijn, and C.J. Hoogendoorn. J. Electrochem. Soc. 138, page:1728, 1991.

[xxix] M. Furuyama and T. Moriya. Toshiba Patent Application No. 57182181 , October 19, 1982.

xxx M.L. Yu and B. J. Eldridge, J. Vac. Sci. Technol. A7, page:625, 1989.

[xxxi] N. Kobayashi, H. Goto, and M. Suzuki. J. Appl. Phys. 69, page: 1013, 1991

[xxxii] M.L. Yu, K.Y. Ahn, and R.V. Joshi. Surface reactions in the chemical vapor deposition of tungsten using WF6 and SiH4 on Al, PtSi, and TiN. J. ppl. Phys. 67(2), pages :1055-1061, January, 1990

[xxxiii] J. Ammerlaan. Kinetics and characterization of Tungsten CVD processes, Ph.D. Thesis, Delft University of Technology, 61-95, 1994.

[xxxiv] E.J. McInerney, T.W. Mountsier, B.L. Chin, and E.K. Broadbent. Advanced Metrallization for ULSI Applications, Eidtors: V.V.S. Rana, R.V. Joshi, and I. Ohdomari, pages: 69-74, Materials Research Society, Pittsburgh, 1992.

[xxxv] R.S. Rosler, J. Mendonca, and M.J. Rice, Jr. Tungsten chemical vapor deposition characteristics using $SiH_4$ in a single wafer system. J. Vac. Sci. Technol. B6 (6), pages: 1721-1727, 1988

[xxxvi] R.V. Joshi, V. Prasad, L. Krusin-Elbaum, M. Yu, and M. Norcott. J. Appl. Phys. 68, page: 5625, 1990.

[xxxvii] H.L. Park, S.S. Yoon, C.O. Park, and J.S. Chun. Thin Solid Films 181, page: 85, 1989.

[xxxviii] D.W. Greve, T.J. Knight, X. Cheng, B.H. Krogh, and M.A. Gibson. Process control based on quadrupole mass spectrometry. J. Vac. Sci. Technol. B 14(1), pages: 489-493, 1995.

[xxxix] K.R. Evans, R. Kaspi, C.R. Jones, R.E. Sherriff, V. Jogai, and D.C. Reynolds. J. Cryst. Growth, 127, page: 523, 1993.

[xl] Transpector¤ Gas Analysis System Manual, part Number 074-276, pages: 2(2)-2(3) , Leynold Inficon Inc.

[xli] M.J. Drinkwine and D. Lichtman Partial Pressure Analyzers and Analysis. AVS Monograph Series, Editor: N.R. Whetten and R. Long, Jr. pages : 24-25, AVS Press.

[xlii] R.J. Ferran and S. Boumsellek. J. Vac. Sci. Technol. A 14, page: 1258, 1996.

[xliii] J. Moyne, H. Etemad, and M. Elta. A run-to-run control framework for VLSI manufacturing. Microelectronic Processing Conference proceedings, September,1993.

[xliv] E. Sachs and A. Hu. Run by run process control: combining SPC and Feedback control. IEEE Trans. Semiconductor Manufacturing. Vol. 8 (1), pages: 26-43,1995

[xlv] S. Adivikolanu and E. Zafiriou. Internal model control approach to run-to-run control for semiconductor manufacturing. 1997 American Control Conference Proceedings, pages: 145-149, Albuquerque, NH, June 1997.

[xlvi] S. Adivikolanu and E. Zafiriou. Extensions and performance/robustness tradeoffs of the EWMA run-to-run controller by using the internal model control structure.

[xlvii] J. Stefani and S. Butler. Application of predictor corrector control to polysilicon gate etching . Proceedings of the American Control Conference, pages: 3003-3007, San Francisco, June 1993.

[xlviii] E. Zafiriou, H. W. Chiou, and R.A. Adomaitis. Nonlinear model based run-to-run control for rapid thermal processing with unmeasured variable estimation. Electrochemical Society Proceedings. Vol. 95(4), pages: 18-31, 1995

[xlix] E.D. Castillo and J. Y. Yeh. An adaptive run-to-run optimizing controller for linear and nonlinear semiconductor processes. IEEE Transactions on Semiconductor Manufacturing, Vol.11 (2), May 1998

[l] E. Zafiriou and M. Morari. Robust Process Control. Published by Prentice Hall, 1989.

[li] J.a. Stefani and P.K. Mozumder. Advanced process control of a CVD tungsten reactor. IEEE Transactions on Semiconductor Manufacturing. Vol. 9 (3), pages:366-383, 1996.

[lii] BTU-Ulvac Inc, North Billerica, MA. Ulvac-ERA 1000 Selective Tungsten Deposition System, 1996.

[liii] H.Y. Chang. Modeling and simulation of a tungsten chemical vapor deposition reactor, Ph.D Thesis, University of Maryland, 2000.

[liv] I. Hirase, T. Sumiya, M. Schach, S. Ukishima, D. Rufin, M. Shishikura, M. Matsuura, and A. Ito. Tungsten and Other Refractory Metals for VLSI Application III, Editor: Victor Wells, Materials Research Society, Pittsburgh, PA, 1988.

[lv] Computer Board Inc. DAS 08H Data Acquisition Board Manual.

[lvi] Computer Board Inc. EXP 32 Expansion Board Manual.

[lvii] P.F. Knewstubb. Mass Spectrometry and Ion Molecule Reactions, page: 1, Cambridge University Press, 1969.

[lviii] Based on the discussion with Dr. Louis Frees from Leybold Inficon.

[lix] T.E. Madey and J.T. Yates, Jr., J. Vac. Sci. Technol. 8, page:525, 1971,

[lx] P.A. Redhead, J. Vac. Sci. Technol. 7, page:182, 1970